Absolute Pressure

► Pressure

Absorption

► Photometer

AC Dielectrophoresis Lab-on-Chip Devices

STUART WILLIAMS
Mechanical Engineering, Purdue University,
West Lafayette, IN, USA
swilliams@purdue.edu

Synonyms

Dielectrophoretic force; DEP

Definition

Dielectrophoresis is the translational motion of a neutral particle by induced polarization in a nonuniform electric field. The magnitude and direction of the induced dielectrophoretic force are dependent on the characteristics of the applied electric field as well as the dielectric properties of the surrounding medium and of the particle itself.

Overview

Herbert Pohl was one of the first to study particle electrokinetics in the 1950s, particularly the manipulation of polarizable particles with nonuniform fields. He coined the term ►dielectrophoresis, and details of his investigations can be found in his classic text [1]. The advancement of microfabrication techniques and the demand of Lab-on-a-Chip technologies have led to the development of dielectrophoresis techniques for particulate, biological and pharmaceutical applications. Dielectrophoresis was initially used to manipulate particles and cells in the micrometer range (1 μm to 1 mm). Since the early 1990s, nanotechnology has incorporated dielectrophoresis for the manipulation of viruses, DNA, protein molecules and other nanoparticles (diameters of 1 nm to 1 μm). This article provides a brief background of dielectrophoresis followed by its basic manipulation of particles using translation, rotation (electrorotation), orientation (electro-orientation) and traveling wave dielectrophoresis. This article approaches design considerations and modeling techniques for the micrometer length scale; it does not specifically address all dielectrophoresis complexities at the nanometer scale. The majority of this article deals with popular applications of dielectrophoresis including novel techniques to induce these forces; by no means does it cover all of the existing applications. For a more extensive explanation of dielectrophoresis the reader is referred to texts by Jones [2], Morgan and Green [3], and Hughes [4], the latter of which addresses techniques for nanometer-sized particles.

For most dielectrophoresis cases, the applied electric field is an alternating current (AC) signal, created with a common frequency generator. In typical experimentation, frequencies are generally greater than 100 kHz with magnitudes below 20 V peak-to-peak. The shape of the signal is typically sinusoidal, but pulse signals have also been used in dielectrophoresis applications. This signal is applied to electrode geometries, the micrometer-sized features of which can be created using simple microfabrication techniques. Electrodes are typically fabricated on the surface of silicon wafers or glass substrates, including microscope slides. For most biological applications it is recommended that the species of interest be visually observed by optical means, which leaves glass or other transparent materials as favorable substrates. In the case where the electrodes themselves hinder visual observation they are patterned out of indium tin oxide (ITO), a transparent conducting material. Microfluidic channels and other fabricated features can easily be incorporated into the system. It is pos-

sible to manipulate, separate or group targeted cells with novel electrode geometry design and fabrication. Due to its simplicity in fabrication and its susceptibility to visual observation and analysis, dielectrophoresis is a favorable technique for biological experimentation.

Dielectrophoretic forces, though, can be induced by means other than an applied electric signal through electrodes. Optical tools can be implemented to modify an applied electric field, making these methods more susceptible for dynamic as opposed to static manipulation of electric fields with surface electrodes. Dielectrophoresis applications are not limited to particulate manipulation either. With properly configured surface-electrode geometry, it is possible to induce fluid motion and create nanoliter-sized droplets. Additionally, dielectrophoretic forces can be utilized to manipulate particles to build micro- and nanostructures such as wires.

Basic Methodology

Before we can incorporate dielectrophoresis into Lab-on-a-Chip systems it is important to have a grasp of the theory behind dielectrophoresis. Basic theory, common experimental parameters, typical dielectrophoretic manipulation techniques, particle modeling considerations and dielectrophoresis-induced effects are discussed below.

Dielectrophoresis

Dielectrophoresis is the translational motion of a particle by induced polarization in a nonuniform electric field. When conductive, uncharged particles are exposed to an electric field they will polarize, inducing a dipole on the particle. The magnitude and charge orientation of the induced dipole are dependent on the permittivities and conductivities of the medium and of the particle. If the electric field is uniform the induced charges on both sides of the particle are equal, creating no net force on the particle. However, if the electric field is nonuniform (Fig. 1) there will be a net force greater than zero. The general expression for the dielectrophoretic force of a homogeneous sphere is expressed as

$$F_{\mathrm{DEP}} = 2\pi\varepsilon_0\varepsilon_{\mathrm{m}} r^3 \mathrm{Re}\big[K(\omega)\big]\nabla E^2 \tag{1}$$

where ε_0 is the permittivity of free space, ε_{m} is the relative permittivity of the medium, r is the radius of the particle, $\mathrm{Re}\,[K(\omega)]$ is the real part of the Clausius–Mossotti factor and ∇E^2 is the gradient of the magnitude of the electric field squared. This equation assumes that the there is no applied phase gradients to the electric field. The Clausius–Mossotti factor is defined as

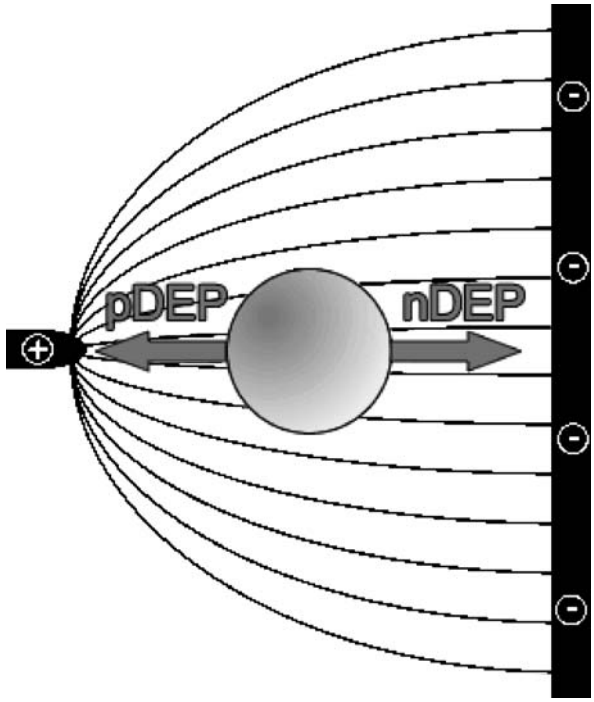

AC Dielectrophoresis Lab-on-Chip Devices, Figure 1 A polarizable particle in a nonuniform electric field

$$K(\omega) = \frac{\varepsilon_{\mathrm{p}}^* - \varepsilon_{\mathrm{m}}^*}{\varepsilon_{\mathrm{p}}^* + 2\varepsilon_{\mathrm{m}}^*} \tag{2}$$

where subscripts p and m are assigned to the particle and medium, respectively, and ε^* is called the complex permittivity. The complex permittivity is

$$\varepsilon^* = \varepsilon_0\varepsilon_{\mathrm{r}} - j\frac{\sigma}{\omega} \tag{3}$$

where j is $\sqrt{-1}$, ε_{r} is the material's relative permittivity, σ is the material's conductivity and $\omega = 2\pi f$ (where f is the applied frequency). The Clausius–Mossotti factor is a function of frequency and, depending on the dielectric properties of the medium and particle, this factor can be either positive or negative with a possible range of $+1.0$ to -0.5. If $\mathrm{Re}\,[K(\omega)]$ is negative, the particle experiences negative dielectrophoresis (nDEP) and is repelled from gradients in the nonuniform electric field (Fig. 1). For a positive value of $\mathrm{Re}\,[K(\omega)]$, the particle is attracted to high electric field gradients with positive dielectrophoresis (pDEP). With dielectrophoresis it is possible to manipulate particles using a variety of techniques and applications.

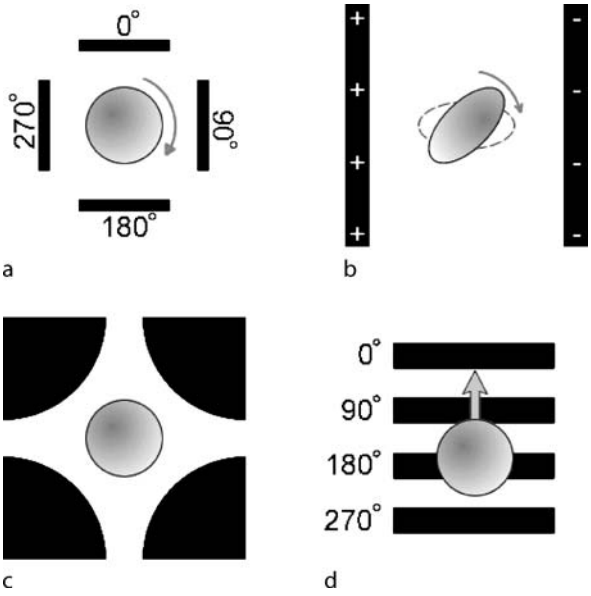

AC Dielectrophoresis Lab-on-Chip Devices, Figure 2 Dielectrophoretic manipulation techniques: (**a**) electrorotation, (**b**) electro-orientation, (**c**) particle trapping and (**d**) traveling wave dielectrophoresis

Particle Manipulation

The majority of dielectrophoretic manipulation of particles includes translating (dielectrophoresis), rotating (electrorotation), orienting (electro-orientation), trapping and using traveling wave dielectrophoresis. Figure 2 provides an illustrative representation of each technique. In electrorotation a torque is applied to a particle that is subjected to a rotating electric field (Fig. 2a). The induced dipole takes a finite amount of time to polarize in a neutral dielectric particle, which attempts to orient itself with the direction of the electric field. This dipole, though, lags behind the applied rotating electric field. The reorientation of the dipole with the electric field induces a torque on the particle, rotating it. Next, electro-orientation involves the alignment of a nonspherical particle in a uniform electric field (Fig. 2b). When an ellipsoidal particle polarizes, the dipole moment will align the particle with its longest nondispersed dipole parallel to the field lines. Its orientation is a function of the electric field frequency and the dielectric properties of the medium and particle.

Dielectrophoretic forces, though, can be used to not only rotate a particle, but trap it as well. There are two types of particle trapping, those that utilize pDEP or nDEP forces. For example, four electrodes can be positioned in a quadrupole arrangement and, when the appropriate electric field is applied, a particle or particles are trapped in the electric field null at its center (Fig. 2c). Particle trapping will be revisited later in this article. Traveling wave dielectrophoresis is the linear application of electrorotation (Fig. 2d). An AC electric wave is produced by applying an electric field that travels linearly along a series of electrodes. The particle will translate in the same or opposite direction as the traveling wave depending on the properties of the applied signal frequency and the dielectrics of the particle and medium.

Modeling and Dielectrophoretic Effects

When incorporating dielectrophoresis in Lab-on-a-Chip systems, additional modeling parameters and electrophysiological interactions need to be considered. Obviously, biological cells and some particulates are not all completely spherical nor are they homogeneous. Typically cells are modeled as multi-shelled particles with each shell having its own respective conductivity and permittivity. Additionally, nonspherical particles are modeled as ellipsoids. For each of these situations the Clausius–Mossotti factor is extended to include these geometrical and layered effects by applying polarization factors. These modifications are described in detail elsewhere [2–4]. The dielectric properties of some particles and cells are unknown; however, dielectric techniques can be applied to determine these characteristics. For example, when an induced particle changes from pDEP to nDEP, or vice versa, this is called its crossover frequency. Similarly, a particle in electrorotation that changes in rotational velocity or direction under different conditions will give insight into its dielectric properties. Many of the previously mentioned dielectrophoretic manipulation techniques can be applied to determine particle dielectric characteristics. By varying both the medium conductivity and the applied frequency, the changes in a particle's induced dielectrophoretic behavior can be visually observed.

The electric field can induce higher order poles, called multipoles, instead of the assumed dipole. This occurs when the electric field is highly nonuniform; for example, when the electrode geometry is on the same length scale as the particle or when a particle is in a field null. For most applications, though, the dipole assumption accurately depicts the behavior of the particle. However, multipoles can effect the particle's interaction with the electric field and will react differently from an induced dipole. The electric field can also induce some negative physiological effects to the cell by inducing cell heating and influencing transmembrane voltage. Transmembrane voltage can affect ion movement and damage voltage-sensitive proteins. The electric field itself can heat the surrounding medium in what is called *Joule heating*. Joule heating creates temperature gradients that can directly heat the cell or create localized convection currents. By working at the

micrometer length scale some of these negative effects are minimized; however, they may still influence the system and cannot be ignored.

Key Research Findings

This dielectrophoresis background only serves as a brief overview; these technologies need to be explored in more detail before incorporating them into a Lab-on-a-Chip system. Lab-on-a-Chip systems integrate techniques of small fluid and sample handling with detection or process capabilities. Dielectrophoresis can be incorporated into these systems to manipulate, separate or trap cells as well as control small amounts of fluid. This technology can be used to trap cells for additional analysis, separate cell types based on dielectric properties, dispense picoliter droplets or used for similar manipulative applications. However, dielectrophoresis itself cannot be used as a sensor, except to determine dielectric properties of cells or detect such changes in response to stimuli. The integration of sensory technologies with dielectrophoresis is not discussed. Instead, specific novel dielectrophoresis applications are addressed in detail.

Trapping Particles

One of the more popular dielectrophoretic manipulation techniques involves the trapping of individual or groups of cells. Dielectrophoresis can be thought of as *electrical tweezers* that will grab onto and position cells. Trapping can be accomplished by means of novel electrode geometries that utilize pDEP or nDEP forces to selectively capture a particle or cell. Some electrode geometries induce both types of forces simultaneously; an example of such an arrangement involves interdigitated electrodes (Fig. 3). Planar electrode fingers, whose width and gap separation are a few times larger than the diameter of the particles of interest, have alternating applied voltages (either 180° out of phase or alternating $+V$/ground). This geometry creates a strong pDEP force at the edges of the electrodes and a field null above the center of each electrode strip. This arrangement provides both trapping capabilities and the ability to determine unknown particle dielectric properties from visual observation. For example, at a particular frequency and medium conductivity a particle will experience a pDEP force. However, for a different applied frequency and/or a change in medium conductivity the same particle could undergo nDEP. The strength of the dielectrophoretic trapping force can be estimated with the hydrodynamic drag necessary to release the particle. Similarly, interdigitated electrodes can be used to separate two cells that experience opposite pDEP/nDEP forces due to their different dielectric characteristics. Interdigitated electrodes are one of the simpler electrode geometries, compared to other trapping arrangements.

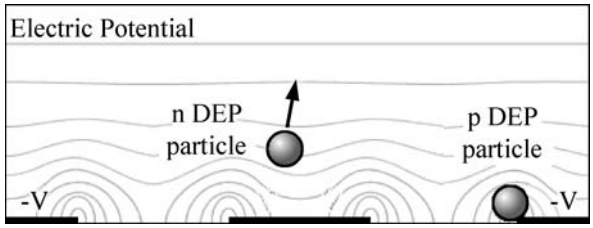

AC Dielectrophoresis Lab-on-Chip Devices, Figure 3 Dielectrophoresis of particles with interdigitated electrodes (side view). Particles experiencing pDEP are attracted to the edges of the electrode while nDEP forces repel the particle to the middle of the electrode

Other electrode geometries have been designed to capture individual cells using either pDEP or nDEP forces. A number of these geometries have been explored by Voldman and his research group [5] and will be discussed here. For pDEP, geometries are created that generate extreme electric field gradients in the trapping region. A geometry that creates such a field gradient is illustrated in Fig. 4a. An electrode smaller than the diameter of the particle has the signal applied through it to a larger, receiving electrode. The generated electric field would be similar to that illustrated in Fig. 1, with a high gradient in proximity to the smaller electrode. Electric field nulls have also been generated with electrode geometries for nDEP traps. Recall the quadrupole geometry in Fig. 2c. When an appropriate electric field is applied a field null is created in the center of the trap. The trapped particle is repelled from the surrounding regions of field gradients. Another nDEP trap is illustrated in Fig. 4b. The electric field is applied from the trapping electrode to the receiving electrode strip. A particle is trapped within the generated null inside the "boxed" electrode geometry. These previous geometries will trap a particle near the surface of the substrate. Electrodes, though, can be arranged three-dimensionally to create traps that capture particles and cells in suspension. One example is a nDEP trap using two stacked quadrupole geometries, resulting in an octopole trap (Fig. 4c). The electric field null is generated in the midplane between these two electrode substrates and thus a particle experiencing nDEP is captured in suspension. These are just a few examples of established trapping geometries, as others could be designed to suit a particular trapping application.

There are numerous trap geometries that exist for both pDEP and nDEP. These electrode arrangements and cell concentration can be varied to trap both single cells and groups of cells alike. However, there are dielectrophoretic interactions that cannot be ignored for trapping applications. Multipoles may need to be considered for single-

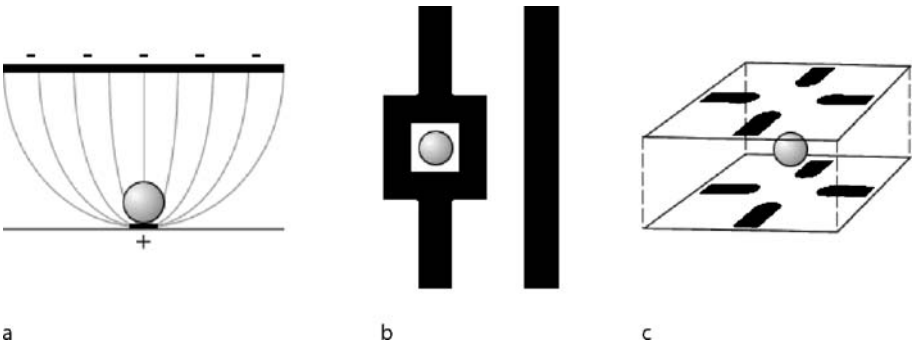

AC Dielectrophoresis Lab-on-Chip Devices, Figure 4 Various electrode geometries for dielectrophoretic traps: (**a**) pDEN trap (side view), (**b**) nDEP planar trap (top view), and (**c**) nDEP octopolar trap

particle traps since the generated field will have inhomogeneities on the scale of the particle itself. Also, particle–particle dielectrophoretic interactions will influence the capabilities of multi-particulate traps. Dielectrophoresis, therefore, needs to be accurately modeled and thoroughly investigated prior to use in a specific application.

Electrode-Based Systems

Microsystems have incorporated dielectrophoretic forces into microchannels to manipulate particles and cells with various electrode geometries. Electrodes can be used to align target cells or separate particulate cells from the rest of the sample, an example of which is illustrated in Fig. 5. These systems use a three-dimensional arrangement of electrodes, with mirrored electrode geometries aligned and separated by microfluidic structures. Thus the electrodes in Fig. 5 are on the top and bottom surfaces of the microchannel and do not significantly impede or manipulate the fluid flow. This system is optimized for a particular set of cells such that the applied signals generate the strongest dielectrophoretic forces; this system will operate with the maximum possible applied flow rate for more effective processing. The system, though, will be selective to a set of cells with the same or similar dielectric properties. This process is obviously advantageous for an application that selectively separates cells based on their dielectric properties. Additionally, this system can simultaneously separate and trap targeted cells for selective biological investigations. An example of a dielectrophoresis system and a description of its potential for biological analysis is explained in [6]. These dielectrophoresis techniques can be coupled with a variety of existing biological tools for innovative applications including fluorescence evaluation of cells in small populations, cell sorting, long-term investigations of single cells, cellular kinetics and other similar Lab-on-a-Chip analyses.

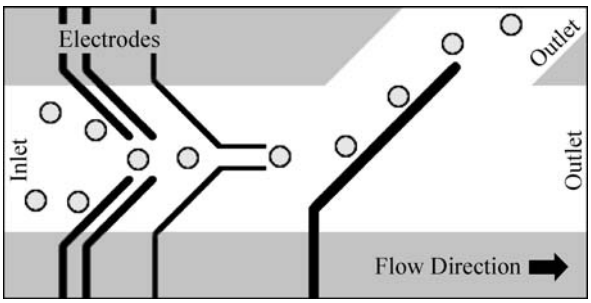

AC Dielectrophoresis Lab-on-Chip Devices, Figure 5 An illustration of a dielectrophoretic microsystem that can selectively sort particles (top view). Recall that the electrodes are on the top and bottom surfaces of the microchannel and to not mechanically manipulate the particles

Insulating Dielectrophoresis

Conventionally, the nonuniform electric fields for dielectrophoresis applications are produced directly with an arrangement of conductive electrodes. However, a nonuniform electric field can be generated in microchannels without direct interaction with electrodes. For example, Cummings generated nonuniform electric fields using remote electrodes placed at the inlet and outlet of the microchannel [7]. The electric field is applied across the channel and is deformed by the variations in the channel geometry or by insulating structures or posts within the microchannel. These mechanical structures within the channel will affect the generated electric field as well as dynamically change the flow field; these can be successfully coupled to produce an efficient particle concentrator within the channel. By using remote electrodes, electrochemical reactions and other unwanted dielectrophoretic effects will not occur within the section of particle collection or concentration. However, this technique relies on the application of higher voltages to produce the necessary electric field gradient, with magnitudes in the hundreds to thousands of volts

(outside the range of conventional waveform generators). The driving mechanism for fluid flow for these systems is electrokinetic in that it combines features of electroosmotic and electrophoretic flows. Insulating dielectrophoresis Lab-on-a-Chip systems use a coupled arrangement of electrokinetic and dielectrophoretic phenomena to separate or capture targeted particles. Consider such a dielectrophoresis system that has an array of insulating posts within a microchannel. At a low applied electric field there will be induced electrokinetic motion but minimal particle manipulation effects from dielectrophoresis. However, at higher magnitudes the influence of insulating posts becomes apparent, inducing dielectrophoretic forces on the particles. At a certain threshold in the applied electric field dielectrophoresis forces on the particles are greater than the electrokinetic forces, resulting in captured targeted particles at the insulating posts. Releasing these particles is just a simple decrease in signal magnitude. Structures other than posts have been successfully used to similarly manipulate and separate particles of different dielectric properties.

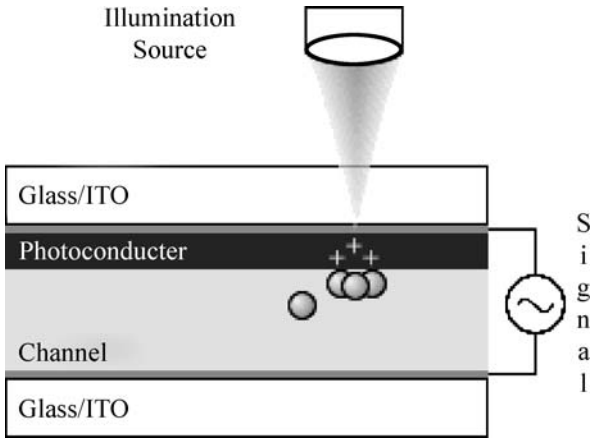

AC Dielectrophoresis Lab-on-Chip Devices, Figure 6 An example for a simple setup for optically induced dielectrophoresis. The optical source is illuminated through the ITO/glass substrate onto the photoconductive layer, creating an electric field gradient in which particles experiencing pDEP are attracted

Optical Dielectrophoresis

An electrode-less approach to induce localized dielectrophoretic forces can be created by light illumination in optically induced dielectrophoresis. This technique utilizes low-power optical beams to manipulate particles and cells. Consider an AC electric signal applied across two parallel electrodes with a film of photoconductive layer in between. This generates a uniform electric field across the film; however, the photoconductive layers have higher conductivities under illumination, thus distorting the otherwise uniform electric field. An illustration of a simplified optically induced dielectrophoresis system is shown in Fig. 6. The illumination of the photoconductive layer produces a virtual electrode and locally induced dielectrophoretic forces. These forces can be used in pDEP or nDEP applications and have the distinct advantage of being temporary, as opposed to permanent microfabricated electrode features. For example, trapped particles can be moved with the translation of the illumination pattern and released by simply turning off the light.

These optical methods, though, have been developed to include image projectors to manipulate cells using larger, patterned illumination areas. For example, virtual structures can be used to direct cells or can be alternatively used to pattern trapped cells. An investigation of optically induced dielectrophoresis for cellular manipulation is found in detail elsewhere [8]. This investigation characterizes the controllability of these optical techniques. This technique, though, should not be confused with optical tweezers (also called optical traps), which manipulate cells with forces generated by a highly focused laser beam. Optical tweezers use high optical intensity that may cause damage to the cell or induce localized heating. In contrast, optically induced dielectrophoretic techniques have about 1000 times less optical intensity.

Liquid Manipulation

Outside of particle manipulation, dielectrophoresis has also been used to control small volumes of liquid [9]. Liquids themselves also polarize and will, therefore, respond to nonuniform electric fields by being attracted to high-field-intensity regions. Liquid dielectrophoresis influences hydrostatic equilibrium and does not directly manipulate the fluid using dynamic mechanisms typically associated with electro-osmotic flow, electroconvection or other electrohydrodynamic methods. As with all dielectrophoresis techniques, liquid dielectrophoretic forces become stronger at smaller length scales, typically the micrometer length scale. Simple applications of this technique require a fluid running between two closely spaced planar electrodes (Fig. 7). A signal is applied between these two electrodes inducing the collection of individual molecules to the area of highest field intensity, along the edges of the electrodes. The liquid will translate and fill the area along these electrode "fingers" until equilibrium is achieved.

When the signal is removed the liquid will retract and return to its original hydrostatic equilibrium form. This retraction can be coupled together with surface structures to generate nanoliter droplets. However, typical voltage magnitudes are in the hundreds of volts, resulting in Joule

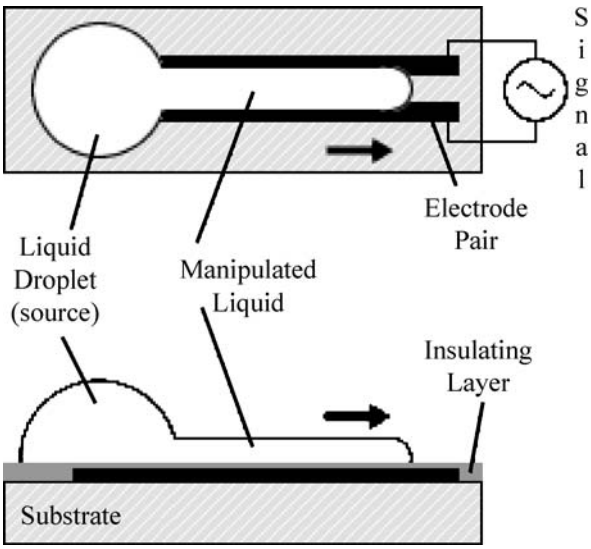

AC Dielectrophoresis Lab-on-Chip Devices, Figure 7 Liquid dielectrophoresis with a set of planar electrode fingers with an insulating layer (top view and side view). A signal is applied to manipulate the liquid to travel along the gap between the electrodes

heating and electrolysis. Electrolysis can be easily avoided by coating the electrode surface with an insulating layer. Heating is typically insignificant when liquids are nonconductive; however, water and other highly conductive liquids will undergo Joule heating. To cope with these issues in present liquid dielectrophoresis systems, very short applications of voltage (< 0.1 s) are applied to avoid heating. Liquid dielectrophoresis involves a complex relationship between electrohydrodynamics, fluid dynamics, surface effects, Joule heating and dielectrophoresis but this technique provides a rapid actuation of liquid that can be utilized in Lab-on-a-Chip systems.

Molecular Dielectrophoresis

Dielectrophoresis has also been used to manipulate macromolecules such as DNA, viruses, proteins and carbon nanotubes. The term *colloids* will be used here to generally describe a particle between 1 nm and 1000 nm. At this scale we need to take into consideration additional parameters that will affect the efficiency and application of dielectrophoresis. The first is Brownian motion, or the random chaotic movement of molecules, which will introduce another destabilizing variable if we were to trap colloids. Second, electrostatic effects at the surface of colloids, created by the electrical double layer, will influence particle–particle interactions. Factors such as hydrodynamic drag, buoyancy, electrothermal effects and a particle's double layer interactions need to be considered when applying dielectrophoresis to colloids.

The importance of mechanically controlling these structures in Lab-on-a-Chip systems with dielectrophoretic techniques will aid in the understanding of their biological interactions with other subcellular entities. For example, miniature quadrupole traps can be used to determine the crossover frequency of specific proteins and viruses. Capturing viruses at a particular set of experimental parameters will give insight into their identification as well as provide a means to concentrate or separate these particles. The crossover frequency of a protein is not only a function of medium conductivity, but it is dependent on the pH as well. Thus, dielectrophoresis can be coupled with chemistry-oriented techniques in order to approach the experimentation of single molecules. DNA has also been manipulated using dielectrophoresis. In one study [10], DNA was uncoiled from its natural bundled condition and stretched between two electrodes, aligning itself along the field lines. It was shown that it took about one-third of one second to uncoil a 48,500 base-pair DNA to a length of 17 μm. The applications of DNA manipulation include electrical measurements between electrodes and positioning of DNA for structural purposes or modification. Carbon nanotubes have also been manipulated similarly. These manipulative techniques have contributed to the assembly of nanometer-sized structures.

Dielectrophoretic Assembly

Dielectrophoresis can be utilized in assembly procedures to induce particle–particle interactions or to use attractive forces between electrodes to position a component and complete a circuit. When two polarized particles come into close proximity to each other they will undergo an attractive force due to their dipole interactions. This is referred to as dipole–dipole interaction, mutual dielectrophoresis or pearl chaining because this phenomenon creates strings of particles. Recall that a particle's induced dipole aligns itself to the electric field and that like particles will always have the same dipole orientation. These particles will have an attractive force since their opposite charges are aligned facing each other. Additionally, these particle chain formations can also be attributed to the distorted electric field caused by the particle's induced dipole. These field disturbances can cause a localized dielectrophoretic force, increasing the strength of these particle–particle interactions. Pearl chains are typically observed near electrode edges where the strength of the electric field is the greatest.

Pearl chains of nanoparticles can be arranged and fused together to create a nanowire or other similar struc-

tures. However, other dielectrophoresis techniques can be utilized to assemble a variety of geometries. Dielectrophoretic traps and optical dielectrophoresis can assemble groups of like particles. Electro-orientation techniques have been used to align and connect nanowires between electrodes. Functionalized particles can be implemented with dielectrophoresis Lab-on-a-Chip systems to create biological sensory or assembly systems. Dielectrophoresis, therefore, is a very versatile engineering tool.

Future Directions for Research

As a nonmechanical and minimally invasive process, dielectrophoresis presents as a tool to be used in Lab-on-a-Chip systems to manipulate particles and cells. These techniques will continue to evolve as the size of microfabricated features continue to decrease past the nanometer scale. This miniaturization will give rise into more comprehensive, subcellular microsystems which need novel methods to manipulate specific entities to suit a biological, chemical or sensory purpose. Dielectrophoresis phenomena at these decreasing length scales will continue to be characterized, leading to newly developed dielectrophoresis phenomena and subsequent innovative manipulation techniques. The future of dielectrophoresis is with the continued investigation and development of novel applications of dielectrophoresis techniques. With the integration of these technologies, a complete dielectrophoresis-driven Lab-on-a-Chip diagnostics system is possible.

Cross References

- ► AC Electro-Osmotic Flow
- ► Dielectrophoresis
- ► Dielectrophoretic Motion of Particles and Cells
- ► Electrokinetic Motion of Cells and Nonpolarizable Particles
- ► Electroosmotic Flow (DC)
- ► Electrophoresis
- ► Electrothermal Effects
- ► Joule Heating in Electrokinetic Flow: Theoretical Methods
- ► Lab-on-a-Chip (General Philosophy)
- ► Lab-on-Chip Devices for Particle and Cell Separation
- ► Techniques for Manipulating Cells

References

1. Pohl HA (1978) Dielectrophoresis. Cambridge University Press, Cambridge
2. Jones TB (1995) Electromechanics of Particles. Cambridge University Press, Cambridge
3. Morgan H, Green N (2003) AC Electrokinetics: Colloids and Nanoparticles. Research Studies Press, Baldock
4. Hughes MP (2003) Nanoelectromechanics in Engineering and Biology. CRC Press, Boca Raton, Florida
5. Rosenthal A, Taff BM, Voldman J (2006) Quantitative modeling of dielectrophoretic traps. Lab Chip 6:508–515
6. Muller T, Pfennig A, Klein P, Gradl G, Jager M, Schnelle T (2003) The potential of dielectrophoresis for single-cell experiments. IEEE Eng Med Biol Mag 22:51–61
7. Cummings EB (2003) Streaming dielectrophoresis for continuous-flow microfluidic devices. IEEE Eng Med and Biol Mag 22:75–84
8. Chiou PY, Ohta AT, Wu MC (2005) Massively parallel manipulation of single cells and microparticles using optical images. Nature 436:370–372
9. Jones TB (2001) Liquid dielectrophoresis on the microscale. J Electrostat 51–52:290–299
10. Washizu M and Kurosawa O (1990) Electrostatic manipulation of DNA in microfabricated structures. IEEE Trans Ind Appl 26:1165–1172

AC Electrokinetics

► Dielectrophoresis

AC Electro-Osmosis (ACEO)

► Nonlinear Electrokinetic Phenomena

AC Electro-Osmotic Flow

MARTIN Z. BAZANT[1,2]

[1] Department of Mathematics and Institute of Soldier Nanotechnologies, Massachusetts Institute of Technology, Cambridge, MA, USA

[2] Ecole Superieure de Physique et Chimie Industrielles, Paris, France

bazant@math.mit.edu

Synonyms

AC pumping of liquids; Traveling-wave electro-osmosis

Definition

AC electro-osmosis (ACEO) is a ►nonlinear electrokinetic phenomenon of induced-charge electro-osmotic flow around electrodes applying an alternating voltage.

Overview

Classical electrokinetic phenomena, such as ►electro-osmotic flow and ►electrophoresis, are linear in the applied voltage and thus cannot produce any net flow under alternating current (AC) conditions. A variety of

►nonlinear electrokinetic phenomena, which persist in AC fields, have been known for decades in colloid science, but the focus has been on electrophoretic mobility and particle interactions. The advent of microfluidics has stimulated interest in the use of electric fields to drive fluid flows, without any moving parts. In this context, nonlinear electrokinetics offers some unique advantages, such as the reduction of unwanted electrochemical reactions (using AC voltages) and the ability to drive fast, programmable flows at low voltages (using closely spaced micro-electrodes).

In the late 1990s, Ramos et al. discovered steady electro-osmotic flow over a pair of micro-electrodes applying an AC voltage and dubbed the effect *AC electro-osmosis* [1]. Around the same time, Ajdari predicted ACEO flow over periodic electrode arrays and showed how the effect could be used for long-range pumping [2]. As the performance of ACEO pumps has advanced [3, 4], ACEO has also been exploited, in conjunction with ►dielectrophoresis (DEP), in different geometries to manipulate particles and cells in microfluidic devices [5–7].

Basic Methodology

Local Flow Generation

ACEO is a phenomenon of ►induced-charge electro-osmosis (ICEO), where flow is generated by the action of an electric field on its own induced diffuse charge near a polarizable surface. The main difference with other examples of ICEO, such as flows around metal colloids, is that ACEO involves electrode surfaces, which supply both the electric field and the induced screening charge, in different regions at different times. For this reason, ACEO is inherently time-dependent (as the name implies) and tied to the dynamics of diffuse charge, as ions move to screen the electrodes.

Perhaps the easiest way to understand ACEO is to consider a pair of planar electrodes applying a sudden DC voltage (which is analogous to ICEO flow around a polarizable particle in an sudden electric field). As shown in Fig. 1, charge relaxation can initially be described by an equivalent RC circuit, where the diffuse layers act as capacitors, connected to "current-tube" resistors of varying length through the bulk solution. Since the resistance is smaller (and the field larger) near the gap, the inner portions of double layers on the electrodes charge more quickly than the outer portions. As shown in Fig. 2, this causes ICEO flow to occur, directed outward from the gap, only when the electrodes are partially screened, as the tangential field from the unscreened outer portions acts on induced charge on the inner portions. Note that the flow is independent of the sign of the applied voltage: If the polarity were reversed, then the field and induced charges would both change sign, resulting in the same ICEO flow.

Under AC forcing, the flow peaks when the oscillation period is comparable to the charging time (Fig. 2b). ACEO flow decays at higher frequencies, since there is not enough time for charge relaxation (Fig. 2a). It also decays at lower frequencies, since there is enough time to completely screen the bulk electric field (Fig. 2c).

Mathematical models of ACEO follow other examples of ICEO, as described in the article on ►nonlinear electrokinetic phenomena. A major simplification in the case of small voltages is to assume sinusoidal response to sinusoidal AC forcing and solve only for the complex amplitudes of the potential and velocity components at a single frequency ω (Fourier mode) [2]. In this regime, the basic scaling of time-averaged ACEO flow is

$$\langle u \rangle \propto \frac{\varepsilon V^2}{\eta(1+\delta)L\left[\frac{\omega}{\omega_c}+\frac{\omega_c}{\omega}\right]^2} \tag{1}$$

where V is the applied voltage, ε and η are the permittivity and viscosity of the liquid (both assumed constant), L is electrode spacing (roughly center to center), δ is the ratio of the diffuse-layer to compact-layer capacitances (both assumed constant). The peak frequency is at the scale of the RC charging time

$$\omega_c \propto \frac{D\,(1+\delta)}{\lambda L} \tag{2}$$

where λ is the Debye screening length and D is a characteristic ionic diffusivity.

The relevant case of a large applied voltage, $V \gg kT/e = 25\,\mathrm{mV}$, is not yet fully understood. A variety of new effects could become important, such as steric effects of finite molecular sizes, viscoelectric effects, discrete electrostatic correlations, dissociation and de-solvation kinetics, and/or Faradaic electrochemical reactions passing current through the surface. In particular, *Faradaic charging* (as opposed to *capacitive charging*, described above) has been proposed to explain experimentally observed flow reversal at high voltage [7], although this has not yet been borne out in a complete mathematical model of ACEO. Standard models of Faradaic reactions mainly predict suppression of the flow (by short-circuiting of the double layer charging process) and flow reversal only in certain cases, at lower frequencies than in the experiments [2, 8]. Although reactions surely play a role in ACEO, high-frequency flow reversal may be attributable to other effects, such as ion crowding in the diffuse layer [9].

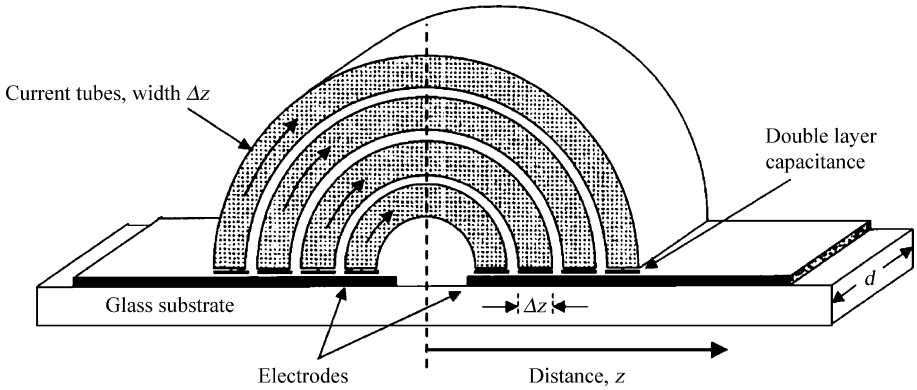

AC Electro-Osmotic Flow, Figure 1 Equivalent RC circuit model for double-layer charging over a pair of electrodes. The inner edges of the electrodes encounter less bulk resistance (due to shorter "current tubes") and thus charge more quickly than the outer edges (reproduced from [1]

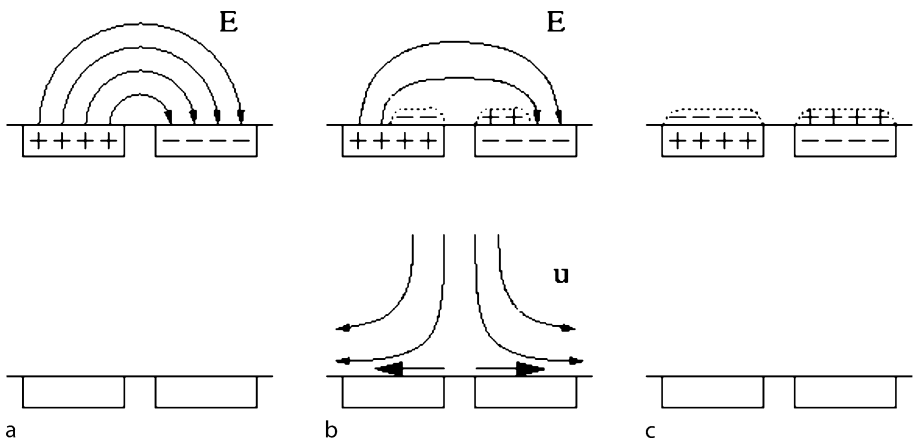

AC Electro-Osmotic Flow, Figure 2 The basic mechanism of AC electro-osmosis: Electrochemical relaxation (top) and induced -charge electro-osmotic flow (bottom) in response to a suddenly applied voltage across an electrode pair. (**a**) At first the electric field has no tangential component on the electrodes, since they are equipotential surfaces, and thus there is no electro-osmotic flow. (**b**) Capacitive double-layer charging begins near the gap where the initial normal current is strongest and causes the unscreened field lines dip down and provide tangential components over the induced charge; the result is ICEO flow directed away from the electrode gap. (**c**) After the charging time passes, the electrodes are fully screened, leaving no electric field and thus no flow. An AC voltage can drive a steady time-averaged flow, similar to (**b**), if its period is comparable to the charging time

Fluid Pumping

Regardless of the details of flow generation, there are some useful general principles to guide the development of microfluidic pumps. ACEO flow over a small set of electrodes can be used for local fluid mixing or particle trapping at stagnation points, but the flow decays quickly away from the electrode surfaces. A symmetric, periodic array of many inter-digitated electrodes (of alternating polarity at each moment in time) similarly produces an array of counter-rotating convection rolls, but no net pumping of the fluid in one direction. Instead, long-range pumping over an electrode array requires broken symmetry within each spatial period to rectify the AC forcing.

There are several ways to design ACEO pumps by breaking symmetry in a periodic electrode array. Ajdari originally suggested modulating either the electrode capacitance via a dielectric coating (Fig. 3a) or the surface height (Fig. 3b) with half the spatial period of the array, so that the one side of each electrode drives stronger ACEO flow compared to the other side and thus "wins" to produce net pumping over the array [2]. In the first implementation of an ACEO pump, Brown, Smith and Rennie opted instead to break symmetry by using planar electrodes of different widths and gaps [10], and, until recently, this design was the only one studied experimentally [3] or theoretically [8].

The performance of ACEO pumps can be greatly enhanced by designing appropriate non-planar electrode geometries.

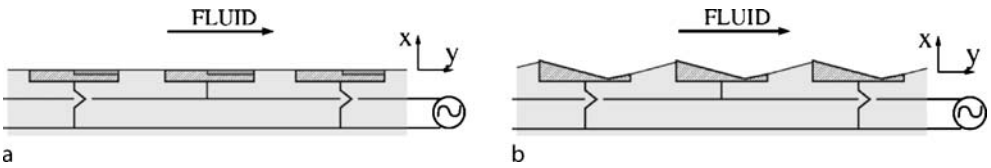

AC Electro-Osmotic Flow, Figure 3 Sketches of local broken symmetries in a periodic electrode array which lead to global time-averaged ACEO pumping: (**a**) non-uniform surface coatings; (**b**) non-uniform surface height (reproduced from [2])

As recently predicted by Bazant and Ben [11], various *3D ACEO* designs exhibit dramatically increased flow rate without flow reversal, due to a special geometry in which the non-uniform slip profile on the electrodes all contributes to flow in the same direction. The basic idea is to create a *fluid conveyor belt* with electrodes each having steps of two different heights: On each electrode, the region of desired forward flow is raised up, while the region of reverse flow is recessed below, so as to recirculate in a vortex aiding the forward flow (rather than fighting it, as in planar designs). This can be accomplished with electrodes having electroplated metal steps, as shown in Fig. 4, although other designs are possible, such as flat electrode steps deposited on a grooved surface (without the vertical metal surfaces). Simulations predict that 3D ACEO pumps are faster than planar pumps by more than an order of magnitude, at the same voltage and minimum feature size, and thus can achieve mm/s velocities with only a few volts. This suggests using 3D ACEO pumps to drive flows in battery-powered, portable or implantable microfluidic devices.

Fluid pumping over electrode arrays can also be achieved by applying a traveling wave of voltage. At low frequency, a similar induced-charge electro-osmotic mechanism, which peaks at the RC frequency (2), is responsible for the flow [12]. At high frequency (or with a thick dielectric coating on the electrodes), the classical Erlich–Melcher effect used to pump dielectric liquids, which peaks at the Debye frequency, $\sigma/\varepsilon = D/\lambda^2$, can also be observed [13]. Although traveling-wave ACEO seems to produce slower flow than standing-wave ACEO with planar electrodes, the possibility of designing suitable non-planar electrodes has not yet been considered.

Key Research Findings

The groups of Ramos [1] and Green [15] have pioneered the study of ACEO by developing theoretical models and measuring flows around pairs of micro-electrodes in dilute KCl. Their work has ruled out ►electrothermal effects (below 5 V in dilute electrolytes) and clarified the capacitive charging mechanism described above. The basic model successfully predicts the scaling of ACEO flow at low voltage and low salt concentration, although it tends to over-estimate velocities.

Following Ajdari [2], there has been extensive experimental [3, 4, 10, 12, 13] and theoretical [8, 9, 11] work on ACEO flows driven by periodic inter-digitated electrode arrays. Velocities exceeding 100 μm/s have been demonstrated in water [4, 10] and dilute KCl [3] by applying several volts at 1 – 100 kHz frequencies using asymmetric arrays of planar electrodes with unequal widths and gaps, at the scale of several microns. Somewhat slower flows have also been achieved by applying traveling-wave voltages with inter-digitated planar electrodes [12, 13], although the electrical connections are more complicated.

A puzzling feature of ACEO in many situations with planar electrodes is that the flow direction can reverse (compared to the theory) with increasing voltage, typically above 2 V. For example, high-voltage flow reversal has been observed in dilute KCl for AC forcing [3] and traveling-wave forcing [13] and in tap water for AC forcing with a DC offset [7]. As shown in Fig. 5a, the reverse flow is eventually faster than the forward flow and seems to grow more quickly with voltage than the expected scaling $u \propto V^2$.

Another puzzling feature of ACEO is the strong decay of the flow with increasing salt concentration. For this reason, all experiments in the literature have used either very dilute solutions (mostly KCl) or water (de-ionized or from the tap). A few groups have studied the concentration dependence of ACEO in aqueous KCl solutions [3, 15, 16]. These experiments and recent work on ►electrokinetic motion of heterogeneous particles suggest that flows due to ►induced-charge electro-osmosis exhibit a universal decay with concentration like $u \propto \log(c_{\max}/c)$ at large voltage [9]. As shown in Fig. 5b, the flow effectively vanishes above a bulk salt concentration of only $c_{\max} \approx 10$ mM, which is an order of magnitude smaller than most biological solutions.

Nevertheless, advances have been made in applying ACEO flows to pumping, mixing, and trapping particles in microfluidic devices. Experiments on 3D ACEO pumps with non-planar stepped electrode arrays have demonstrated an order of magnitude increase in flow rate versus the fastest planar design, due to the robust fluid-conveyor-

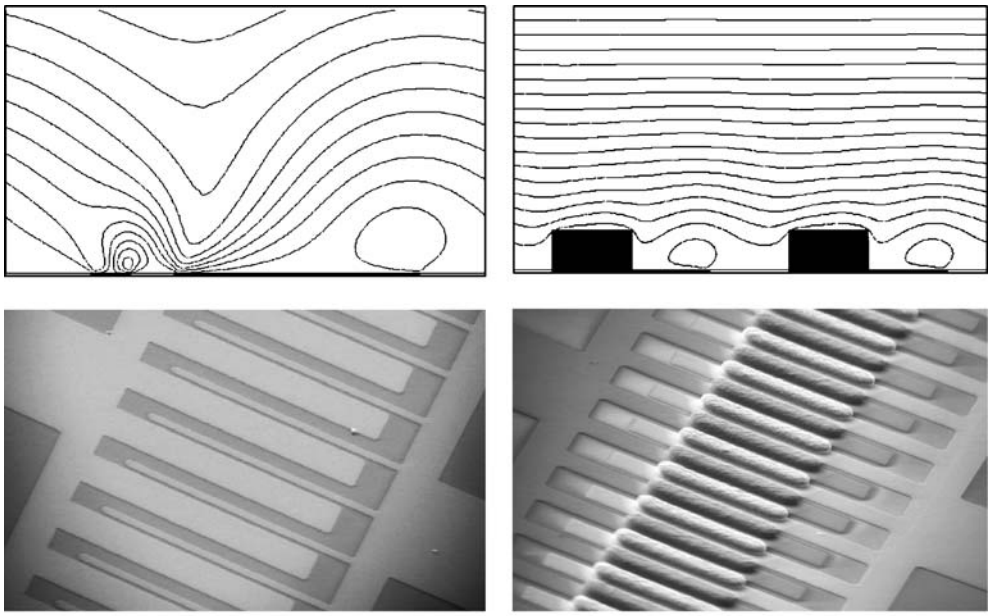

AC Electro-Osmotic Flow, Figure 4 Top: Simulations of ACEO microfluidic pumps, showing the time-averaged flow over a pair of micro-electrodes (dark regions) in one spatial period of an interdigitated-electrode array. (**a**) A nearly optimal planar design with different electrode sizes and gaps; the smaller electrode has the largest local slip velocity, but the larger electrode "wins" in overall pumping from left to right. (**b**) A much faster 3D ACEO design with stepped electrodes having a symmetric footprint and the same minimum feature size; the reverse slip now recirculates in a vortex to create a *fluid conveyor belt* for the raised pumping flow from left to right (reproduced from [11]). Bottom: Scanning electron microscopy images of each design fabricated in gold on glass with minimum feature size (gap) of 5 μm (unpublished, courtesy of J. P. Urbanski using the methods of [4, 14])

belt mechanism [4]. For a wide range of near-optimal step heights, there is also no observed flow reversal [14]. Therefore, it is now possible to drive fast, reliable mm/s flows in water or dilute electrolytes with less than 3 V, which can be provided by a small lithium battery.

Progress has also been made in exploiting ACEO flows to manipulate colloidal particles and biological cells in microfluidic devices [5–7]. The basic strategy is to use ACEO flow to draw particles to stagnation points on the electrodes, where they are trapped, presumably by DEP (although the classical theory does not seem to predict this effect). By increasing the voltage, the ACEO flow can be reversed, and particles are observed to move away from the stagnation lines, overcoming any remaining trapping force. In this way, it is possible to "write" and "erase" suspended particles, bacteria, or micro-algae on microelectrodes, as shown in Fig. 7a. This effect can be enhanced by added a DC bias voltage to the low-frequency AC voltage (50 – 100 Hz) between adjacent electrodes [7]. Particles are observed to collect only on the positively biased electrode, as shown in Fig. 7b. It has been suggested that opposing ACEO flows are produced by the competition between Faradaic charging on one electrode (positive bias) and capacitive charging on the other (negative bias), but a quantitative theory remains to be developed and confirmed systematically by experiments.

Future Directions for Research

ACEO is attractive to exploit in microfluidics since it offers precise local flow control without moving parts, using standard fabrication methods from the electronics industry. Device operation requires only the voltage (few Volts), power (mW), and current (mA) of a small battery, and Faradaic reactions are reduced or eliminated. These features make ACEO a promising route to portable or implantable microfluidic systems. In contrast, DC electroosmotic pumps, such as those exploiting electroosmotic flow in porous media, typically require several 100 V and produce bubbling at the electrodes due to electrolysis, which can require a catalytic gas management system. On the other hand, ACEO pumps have so far only produced very small pressures (< 10 Pa) far below those of porous-plug DC pumps (> 100 kPa), but new designs could close this gap. In any case, the ability to tune flows and particle motion by ACEO at the micron scale by modulating relatively small AC voltages could have many uses, e. g. for

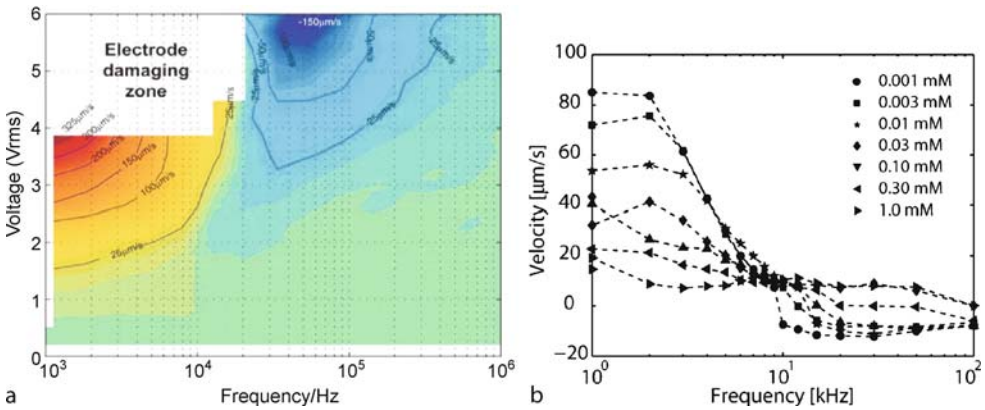

AC Electro-Osmotic Flow, Figure 5 Experimental data for ACEO pumping of KCl around a microfluidic loop, one-fifth covered by the asymmetric planar electrode array of Fig. 4a. (**a**) Contour plot of mean velocity versus AC frequency and RMS voltage at a bulk salt concentration of 0.1 mM (reproduced from [3]), where *electrode damaging* refers to bubble formation and inability to observe consistent flows. (**b**) Velocity versus AC frequency at 2 V peak-to-peak for different concentrations (reproduced from [16]). Both show high-voltage, high-frequency flow reversal, and the latter shows the strong decay with salt concentration

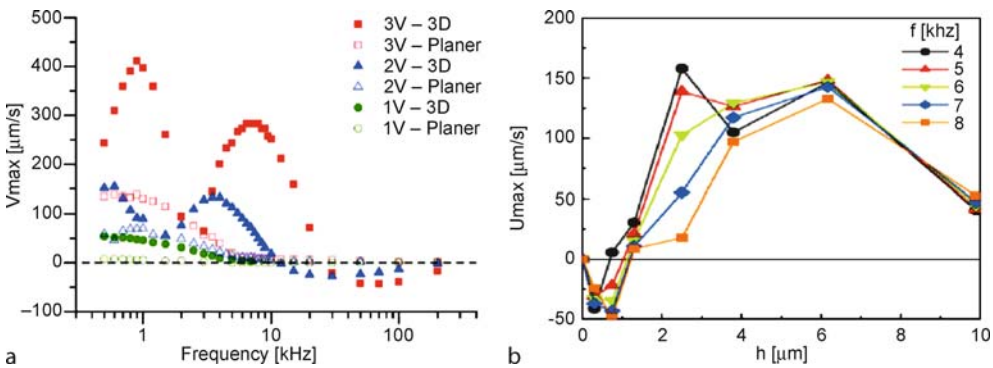

AC Electro-Osmotic Flow, Figure 6 (**a**) Comparison of ACEO pumping of water around a microfluidic loop by planar and (non-optimal) 3D electrode arrays with similar 5 μm minimum feature size (reproduced from [4]). (**b**) Experimental optimization of the step height for 3D ACEO pumping of dilute KCl (reproduced from [15])

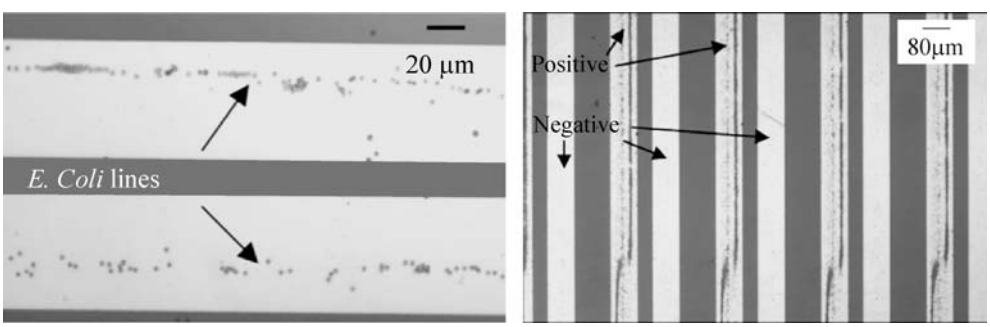

AC Electro-Osmotic Flow, Figure 7 (**a**) Collection of *E. Coli* bacteria in tap water along the stagnation lines of ACEO flow on Au microelectrodes at low frequency (100 Hz) and moderate voltage (1 V). (**b**) Preferential particle trapping by asymmetric polarization ACEO on electrodes with positive DC bias at higher voltage ($>$ 3 V) (reproduced from [7])

mixing, flow fragmentation, or manipulation of colloids and cells.

Understanding flow reversal in ACEO is an important open question, from both fundamental and practical points of view. As noted above, it has been attributed to Faradaic reactions, using theoretical arguments suggesting a scaling $u \propto e^V$ [7]. Simulations of ACEO pumps using standard Butler–Volmer reaction kinetics have failed to predict any flow reversal, except at low frequencies below 100 Hz [2, 8], although this may be consistent with experiments showing low-frequency flow reversal with a DC bias [7]. In contrast, high-voltage flow reversal with unbiased AC forcing in electrode-array pumps tends to occur at high frequency (> 10 kHz), as shown in Fig. 5. An alternative hypothesis, which predicts high-frequency, high-voltage flow reversal due to capacitive charging alone, is based on the reduction of double-layer capacitance due to ion crowding effects [9]. The question is far from settled, however, and more theoretical and experimental work is needed.

Another important open question concerns the dependence of ACEO flow on the solution chemistry (concentration, ionic species, solvent characteristics, etc.). The suppression of ACEO above 10 mM bulk salt concentration limits its use in biological applications and points to possible new physics of the double layer at large voltages, such as a dramatic increase in the diffuse-layer viscosity upon ion crowding [9]. Very few electrolytes have been studied experimentally, but current work suggests that varying the ionic species can also substantially alter the flow. An interesting direction for future research would be to develop surface coatings, electrode materials, and buffer solutions to mitigate or manipulate these complex interfacial phenomena.

Cross References

- ► Dielectrophoresis
- ► Dielectrophoretic Motion of Particles and Cells
- ► Electrical Double Layers
- ► Electrokinetic Motion of Polarizable Particles
- ► Electrokinetic Motion of Heterogeneous Particles
- ► Electroosmotic Flow (DC)
- ► Electrokinetic Flow in Porous Media
- ► Induced-Charge Electro-Osmosis
- ► Nonlinear Electrokinetic Phenomena

References

1. Ramos A, Morgan H, Green NG, Castellanos A (1999) AC electric-field-induced fluid flow in microelectrodes, J Colloid Interface Sci 217:420–422
2. Ajdari A (2000) Pumping liquids using asymmetric electrode arrays. Phys Rev E 61:R45–R48
3. Studer V, Pepin A, Chen Y, Ajdari A (2004) An integrated AC electrokinetic pump in a microfluidic loop for fast tunable flow control, Analyst 129:944–949
4. Urbanski JP, Thorsen T, Levitan JA, Bazant MZ (2006) Fast ac electo-osmotic pumps with non-planar electrodes, Appl Phys Lett 89:143508
5. Green NG, Ramos A, Morgan H (2000) AC electrokinetics: a survey of sub-micrometre particle dynamics, J Appl Phys D 33:632–641
6. Wong PK, Wang TH, Deval JH, Ho CM (2004) Electrokinetics in micro devices for biotechnology applications, IEEE/AMSE Transactions on Mechatronics 9:366–376
7. Wu J (2006) Biased AC electro-osmosis for on-chip bioparticle processing, IEEE Transactions on Nanotechnology 5:84–88
8. Olesen LH, Bruus H, Ajdari A (2006) AC electrokinetic micropumps: The effect of geometrical confinement, Faradaic current injection, and nonlinear surface capacitance, Phys Rev E 73:056313
9. Bazant MZ, Kilic MS, Storey B, Ajdari A (2007) Nonlinear electrokinetics at large applied voltages. Preprint. (http://www.arxiv.org/abs/cond-mat/0703035)
10. Brown ABD, Smith CG, Rennie AR (2000) Pumping of water with AC electric fields applied to asymmetric pairs of microelectrods. Phys Rev E 63:016305
11. Bazant MZ, Ben Y (2006) Theoretical prediction of fast 3D ACEO pumps, Lab Chip 6:1455–1461
12. Cahill BP, Heyderman LJ, Gobrecht J, Stemmer A (2004) Electro-osmotic streaming on application of traveling-wave electric fields. Phys Rev E 70:036305
13. Ramos A, Morgan H, Green NG, Gonzalez A, Castellanos A (2005) Pumping of liquids with traveling-wave electroosmosis. J Appl Phys 97:084906
14. Urbanski JP, Levitan JA, Burch DN, Thorsen T, Bazant MZ (2006) The effect of step height on the performance of AC electro-osmotic microfluidic pumps, J Colloid Interface Sci 309:332–341
15. Green NG, Ramos A, Gonzalez A, Morgan H, Castellanos A (2000) Fluid flow induced by nonuniform ac electric fields in electrolytes on microelectrodes. I. Experimental measurements. Phys Rev E 61:4011–018
16. Bazant MZ, Urbanski JP, Levitan JA, Subramanian K, Kilic MS, Jones A, Thorsen T (2007) Electrolyte dependence of AC electro-osmosis. In: Proceedings of 11th International Conference on Miniaturized Systems for Chemistry and Life Sciences (MicroTAS), 2007, pp 285–2878

Acoustic Droplet Ejection

► Transport of Droplets by Acoustics

Acoustic Levitation of Droplets

► Transport of Droplets by Acoustics

Acoustic Particle Concentration

► Transport of Droplets by Acoustics

Acoustics Based Biosensors

N. Gozde Durmus[1], Richard L. Lin[2], Mariel Kozberg[3], Deniz Dermici[4], Ali Khademhosseini[5,6], Utkan Demirci[5,6]
[1] Department of Molecular Biology and Genetics, Middle East Technical University, Ankara, Turkey
[2] Department of Materials Science and Engineering, Massachusetts Institute of Technology, Cambridge, MA, USA
[3] Department of Chemical Engineering, Massachusetts Institute of Technology, Cambridge, MA, USA
[4] Department of Economics, Bogazici University, Istanbul, Turkey
[5] Harvard-MIT Division of Health Sciences and Technology, Massachusetts Institute of Technology, Cambridge, MA, USA
[6] Center for Biomedical Engineering, Department of Medicine, Brigham and Women's Hospital and Harvard Medical School, Cambridge, MA, USA
udemirci@partners.org

Synonyms

Acoustic waves; Medical imaging; CMUTs

Definitions

A biosensor is defined as an analytical device that uses a biological recognition system to target molecules or macromolecules. Biosensors use a physio-chemical transducer to convert the signal from the bio-recognition system into a detectable signal [1]. Biosensors consist of three components: 1) the detector, which identifies the stimulus; 2) the transducer, which converts this stimulus to an output; and 3) the output system, which involves amplification and display of the output in an appropriate format [1].
Piezoelectricity is a phenomenon displayed in certain crystals, such as quartz and Rochelle salt, where mechanical stress induces voltage generation and vice versa.

Overview

There is an increasing demand for small, reliable, disposable, and inexpensive sensors in industrial, medical, and a variety of other science and engineering fields. Sensors are one of the fastest growing markets, with annual growth of about 18%. In particular, the market for biosensors is increasingly promising due to their application in progressing areas of healthcare, biotechnology, and medicine. For instance, the use of biosensors in personal glucose testing, HIV, and early cancer detection are areas with great medical relevance [1]. In addition, the ability to detect pathogenic and physiologically relevant molecules in the body with high sensitivity and selectivity offers a powerful tool in early diagnosis and treatment of diseases [1].
An acoustic wave biosensor utilizes acoustic or mechanical waves as a detection mechanism to obtain medical, biochemical, biophysical information about the analyte of interest [1, 2]. It detects changes in mass, elasticity, conductivity and dielectric properties from mechanical or electrical variations. These devices also employ the piezoelectric effect to excite acoustic waves electrically at an input transducer and to receive the waves at the output transducer [2].
The first scientific experiment of piezoelectricity was conducted in 1880 by Pierre and Paul Jacques Curie, who found that compression of various crystals leads to voltage production on their surface. They showed the converse effect the following year by demonstrating the elongation of certain crystals when injected with electric current. Although these observations intrigued the scientific community, piezoelectricity remained much of a laboratory technology until Paul Langevin used piezoelectric transducers to construct sonar for submarine detection in 1915 [3]. Acoustic biosensors can be made with piezoelectric crystals such as quartz, lithium niobiate or lithium tantalate since they are robust and environmentally stable. In addition, such sensors are versatile and can detect, in principle, various biomolecules [1]. Acoustic wave sensors can be categorized according to the waves they generate, such as bulk or surface acoustic waves (Fig. 1). Each of these wave mechanisms have various advantages and disadvantages depending on their specific applications [1].
The goal of this review is to categorize and describe the mainstream acoustic wave biosensors. We will begin by discussing biosensors that utilize bulk acoustic waves and subsequently analyze devices that employ surface acoustic waves. We will also examine sensors that employ capacitive micromachined ultrasound transducers, a novel technology that does not require piezoelectric substrates. For each type of these sensors, we will present an overview of their scientific mechanisms and fabrication techniques in the Basic Methodology section. We will then go on to discuss the advantages and applications in biology and medicine in the Key Research Findings and Future Direction for Research sections.

Basic Methodology

Bulk Acoustic Wave (BAW) Devices

Bulk acoustic wave (BAW) biosensors employ either longitudinal or shear waves, although the latter is often preferred to reduce acoustic radiation in the medium of

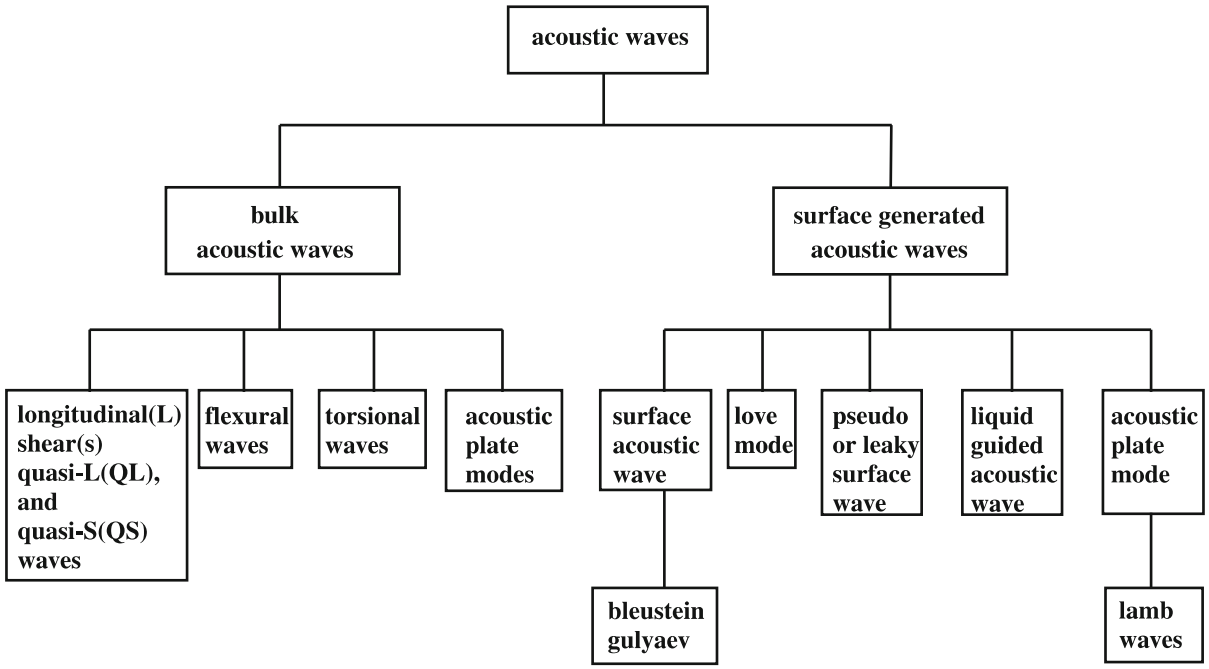

Acoustics Based Biosensors, Figure 1 Classification of acoustic waves [1]

interest. They are the oldest and the simplest acoustic wave devices. BAW devices consist of a parallel electrode placed on both sides of the thin piece of crystal. A BAW sensor can technically employ any piezoelectric element and typically quartz is used, as it is an inexpensive material readily available in nature and easily synthesizable in abundant quantities. In addition, thin disks of quartz are more stable at high temperatures than other piezoelectric elements. When an alternating electric field is applied, it results in a potential difference between the two electrodes and the shear deformation of the crystal. As a result, there is mechanical oscillation of a standing wave across the bulk of the quartz. The frequency of the vibrations is dependent on quartz properties such as density, size, and phase in contact with the crystal surface [4]. Currently, thickness shear mode (TSM) resonator and shear-horizontal acoustic plate mode (SH-APM) sensors remain the most widespread BAW sensors. The other two common BAW sensors that lie beyond the scope of this article are the thin rod acoustic wave sensors and the flexural plate wave devices [4].

BAW Device – Thickness Shear Mode (TSM) Resonator

TSM resonator, also known as quartz crystal microbalance (QCM), is the simplest and most widespread acoustic wave device today. TSM typically composes of a quartz plate sandwiched by electrodes on opposite faces. Electric field crosses through this plate when voltage is applied to the electrodes, resulting in a shear mechanical strain or displacement in the quartz. By oscillating the voltage frequency, a mechanical resonance can be generated, where the maximum displacement of crystal occurs at the surfaces. The resonant frequency, F_r, and the quality factor, Q, are the two resonance parameters. While F_r is the mechanical thickness shear resonance as mentioned before, it is also defined as the frequency of the maximum value of the electrical conductance, G_{el}. Q is approximated mathematically from the electrical conductance resonance spectrum as $Q = F_r/\Delta F_{BW}$, or the ratio of resonant frequency to the half bandwidth [5] (1).

Coupling of molecules in solid, liquid, or gas phase to the TSM resonator changes the resonance parameters. When mass attaches onto the crystal face, it raises the quartz's overall weight and reduces F_r. Saurbrey first derived the mathematical relationship between loading mass and F_r to be:

$$\Delta f = -\frac{2f_0^2 \Delta m}{A_{piezo}(u_q p_q)^{1/2}}$$

(1) The variables Δf, f_0, Δm, A_{piezo}, u_q, and p_q represent, respectively, the crystal's measured frequency shift, initial resonant frequency, mass change, surface area, shear mod-

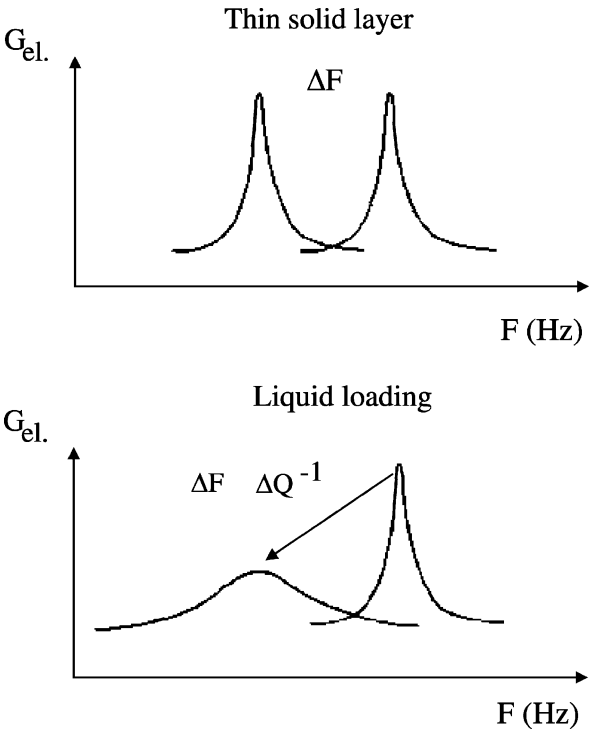

Acoustics Based Biosensors, Figure 2 Changes to the resonance peaks due to a thin solid layer (top) and liquid (bottom). Note the decrease in Q for TSM resonator in liquid [22]

ulus, and density [6]. TSM resonators immersed in liquid present a special case because acoustic energy dissipation through the fluid lowers Q as well. Additional formulas need to be applied to account for the liquid's viscosity and loading [6]. Figure 2 shows a comparison between shifts induced by solid and liquid loading on resonators.

TSM resonators possess lower mass sensitivity than most acoustic wave sensors that employ other mechanisms since they typically operate between only 5 and 30 MHz. Thinner devices can be used to increase frequencies that result in increased mass sensitivity, they are more fragile and harder to manufacture and handle [5]. Recent research on this topic has been on creating high-frequency TSM resonators with piezoelectric films and bulk silicon micromachining techniques.

TSM Fabrication

TSM resonator fabrication usually utilizes photolithography [2]. The resonance frequency of the quartz crystal depends on the shear modulus, density, and material thickness [1]. After polishing the quartz, photoresist is deposited and the device is exposed to UV light through a mask, which determines the active areas that have to be

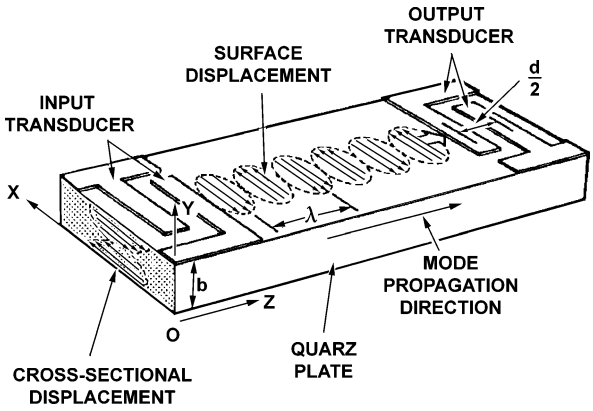

Acoustics Based Biosensors, Figure 3 SH-APM can sense on either side of the device because waves travel between the upper and lower surfaces of the plate [2]

metalized on the devices. On a TSM resonator, they represent the location of the electrode plates. A chemical interface is then added to the remaining crystal surface, where molecules in the liquid can bond to and be detected [2].

BAW Device – Shear-Horizontal Acoustic Plate Mode (SH-APM) Sensor

First introduced in the 1980s, SH-APM sensors use a thin piezoelectric substrate, or a plate, to guide the acoustic wave and to confine its energy within the plate's top and bottom surfaces. Most of the production and analysis principles employed in SH-APM sensors are used in a TSM resonator. Their most striking difference is that SH-APM sensors employ interdigital transducers (IDT) rather than electrode plates. IDTs are deposited on opposite ends of a surface, where one IDT generates displacement waves through application of an oscillating voltage and the other receives it (Fig. 3) [2]. The surface without IDT is immersed in the targeted liquid and acts as the sensor, so the device will not suffer from corrosion problems as electrode plates do in biological solutions [7].

Like TSM resonators, SH-APM sensors prevent the acoustic waves from gaining a shear vertical component and thus lessening energy radiation in the form of compression waves into the liquid. They achieve this by restraining particle displacement within the plate plane. However, given a SH-APM and a TSM device of similar plate thickness, the former usually attains higher mass sensitivity than the latter because IDT is much smaller and precise than the electrode plates on TSM. In general, SH-APM devices generate waves with a frequency ranging from 100 to 150 MHz, but they are also more complex and expensive than their TSM relatives [2].

SH-APM Fabrication

Although the crystals and substrates may be different, SH-APM sensors are fabricated in a similar fashion as TSM resonators. One difference that must be noted is the use of IDTs in SH-APM fabrication, which is not present in TSM resonators. Depending on the application, the optimization of sensor performance can be achieved through adjustments of the length, width, position, and thickness of the IDTs. These parameters can be altered by varying the design of the masks, amount of photoresist and other chemicals used in the fabrication process [2, 7].

Moreover, SH-APM devices require additional processing during their fabrication of the thin plates with respect to the IDT periodicity. Thin slices of piezoelectric materials such as quartz are often used. The whole procedure permits researchers to choose the correct crystallographic orientation for generating the desired shear waves. Despite this improvement, SH-APM devices remain less sensitive than SAW devices for two reasons. First, energy of the wave does not reach a maximum at the surface. Second, similar to TSM, SH-APM is restrained by a minimum thickness of piezoelectric plate [2, 7].

Surface Acoustic Wave Sensors (SAW)

Surface acoustic wave (SAW) sensors have been used for years in measuring temperature, pressure, viscosity, acceleration, concentration and chemical/biological entities [3]. They are also used to perform signal-processing operations and are sensitive to their environment [8]. This type of acoustic wave sensors consists of basic components such as piezoelectric substrate (crystals such as quartz, GaAs, or $LiNbO_3$), micrometallization patterns (electrodes), interdigital transducers (IDT) and active thin films. Unlike BAW, which only interacts with the environment at the opposite surface of the material by traversing through it, SAW travels along or near the surface of the piezoelectric material [3]. The piezoelectric device detects small mass changes at the surface of the sensor as a frequency response, as the electrodes on the surface of the piezoelectric substrate transmit and receive acoustic waves [8]. The acoustic wave is confined to the surface of the piezoelectric substrate and the excited wave is propagated along the crystal surface. The surface wave velocity changes due to the mass or the viscosity changes due to the binding reactions on the sensor surface. The range that SAW device operates depends on the acoustic velocity of the crystal substrate and IDT wavelength, and it usually lies between lower MHz range to the GHz range [8]. These devices are commonly used because of their ability to directly sense the changes in mechanical and mass properties and they have a broad range of applications such as pressure, temperature, viscosity, mass, chemical and biological sensing [8]. SAW sensors coated with organic and/or inorganic materials can be used to analyze absorption on the surface of a device [9]. For chemical sensing, the chemoselective material must be tailored to the analyte of interest. During its operation, SAW sensor responds to a gas or vapor exposure in air by a shift in resonant signal frequency, and then recovers to the original signal frequency, when the sensor is exposed to ambient air free of the responding analyte [8]. The SAW velocity changes according to the absorbed chemical substance and it results in the alternation of the mass load, the elastic stress and the conductivity of the polymer coating on the SAW device.

SAW devices are also considered as "electronic noses." An electronic nose is a device that is composed of a chemical-sensing system and a pattern-recognition system. Electronic noses mostly have the ability to detect very low vapor concentrations [8]. If there is vapor on the piezoelectric surface of the SAW device, the chemical substances in the vapor and in the acoustic wave interact and the properties of the wave changes. Sensitivity of the SAW detector is dependent on the temperature of the piezoelectric crystal and the vapor-pressure of the analyte. Chemical concentration of analyte of interest can be tested by monitoring the frequency. The SAW chemical sensor requires no special support gases and no consumables other than electrical power. Many of the SAW devices have been produced for military and defense applications. They are used for on-the-spot vapor detection of plastic explosives containing nitro groups such as trinitrotoluene (TNT) and cyclotrimethylenetrinitramine (RDX) [8]. As a result, SAW sensors are attractive for real-time detection and monitoring of toxic or hazardous gases, vapors and they are used in biology as a sensitive method for detection of biochemicals and biomolecular interactions [9].

SAW devices operate at high frequencies, which lead to smaller, more sensitive devices that have limits in the picogram range [8]. SAW devices can be miniaturized by using photolithographic techniques and complex circuits can be present on the substrate surface. Miniaturization makes them advantageous since the smaller dimensions increases the sensing surface area and binding properties [6]. Moreover, there is a dual-delay system with SAW sensors (Fig. 4). It is a layered structure and has three fundamental advantages. First, it compensates the influence of temperature on the differential frequency and the air pressure. Second, it reduces the measured frequency of the system from MHz range to kHz range [6]. Third, SAW devices have the ability to directly sense mass and mechanical changes in an environment, which makes them more sensitive than other electrical and thermal biosensors. Furthermore, they have numerous advantages in bio-

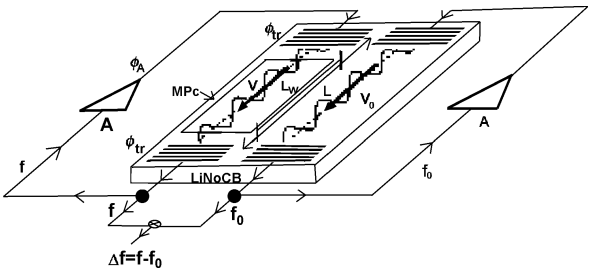

Acoustics Based Biosensors, Figure 4 SAW device dual delay line structure and its principal of operation [21]

logical applications [6]. These devices are also more cost-efficient than the optical biosensors and easier to handle. They are employed to study biomolecular interactions and allow easy and direct detection of analyte of interest [8]. In summary, SAW technology is a cost-effective method of label-free detection of biomolecular interactions and allows direct monitoring on the surface of a transducer in real time [10].

SAW Device Fabrication

Various lithographic techniques are used in the fabrication of interdigital transducers (IDT's) for surface acoustic wave sensors. The most widely used and least costly photolithographic technique to fabricate SAW devices is conventional contact printing. It uses rigid or conformable glass plates bearing the photographic image, which can be negative or positive depending on the fabrication steps of the IDT pattern [11]. Mass production of acoustic devices is done by optical lithography. Excitation of the SAW harmonics depends on the metallization ratio between the gaps and the electrodes of the SAW device. A lithography method especially suited for the fabrication of small gaps is the near-field phase shift technique. In this technique, a transparent mask with a pattern on its surface is brought into contact with the substrate. The phase of the exposing light is modulated at the edges of the patterned relief. High frequency, low-loss SAW devices can be fabricated by depositing thin piezoelectric films on substrates. These include ZnO, GaN, AlN, and $Al_xGa_{1-x}N$ thin films on sapphire, SiC and diamond substrates. The SiO_2/ZnO/diamond structure can provide a high acoustic velocity and a zero temperature coefficient of frequency. Extremely high velocity SAW modes with moderate coupling coefficient in AlN and GaN thin films are deposited on SiC, diamond, or sapphire substrates [12]. In addition, imprint lithography is a commercial method to fabricate SAW devices, especially for simple pattern, one-mask-level applications, where large areas can be patterned with nanometer-scale critical dimensions and high fidelity. Moreover, nanoimprint lithography is becoming a popular lithographic method. SAW filters and SAW correlators, present ideal structures to be fabricated using this method.

Capacitive Micromachined Ultrasonic Transducers (CMUTs)

Electrostatic transducers have been used for sound wave excitation and detection as an alternative to piezoelectric devices that are used widely for nondestructive evolution and medical-related applications. The vibration of a thin plate under electrostatic forces is the main acoustic actuation and sensing mechanism of these devices. These devices are based on the electrostatic attraction force between the backplate and the metallized membrane. The simplest forms of this device consists of a thin metal membrane that is stretched above a back electrode forming a small gap [13]. Upon exposure to sound waves, the gap height is modulated at the frequency of the incoming pressure field that induces a change in the device capacitance, which generates an output voltage proportional to the amplitude of the field. The capacitor is also used to generate sound waves. The advantage of the electrostatic devices compared to the other types of transducers is the impedance matching between the transducer and the surrounding medium. Advances in the silicon micromachining techniques enabled the fabrication of micro electro-mechanical systems (MEMS) based electrostatic transducers. These devices use the ultrasonic waves due to the miniaturization capacity of the silicon machining techniques and are called, capacitive micromachined ultrasonic transducers (CMUTs) [13].

CMUT are made of small and thin transducer membranes that are suspended over a conductive silicon substrate (Fig. 5). The two plates of the capacitor, substrate and the membrane are separated by a vacuum-sealed cavity. Two-dimensional (2D) arrays of miniaturized electrostatic cells are micro-scale cells that operate in parallel and driven in phase. Surface silicon micromachining is used for their microfabrication [13]. The operation principle of these devices is based on the capacitance modulation of a micro-condenser. Between the metalized membrane and the substrate, a direct current voltage is applied. The membrane is attracted toward the bulk by the electrostatic force, and induced stress within the membrane resists the attraction. If the membrane is exposed to ultrasound, a current output is generated as the capacitance changes under constant bias voltage. The amplitude of the current output is a function of the frequency of the incident wave, the bias voltage, and the capacitance of the device. CMUTs perform operation in the megahertz range. The lateral dimensions of each cell are in the order of tens of microns [13]. The gap

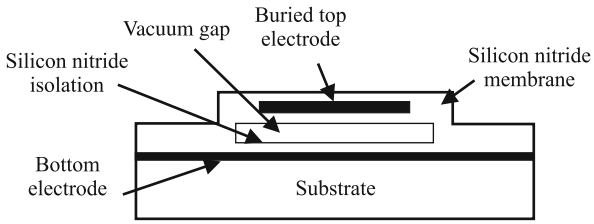

Acoustics Based Biosensors, Figure 5 Schematic cross section of a CMUT transducer membrane [23]

between the membrane and the substrate vacuum-sealed or unsealed can be as small as 500 Å. The membranes may be conductive or coated with a conductive electrode. This structure results in very efficient transducers that can compete with their piezoelectric counterparts in terms of efficiency and bandwidth. The small and thin membranes that constitute the CMUT transducer are micromachined onto a silicon substrate [13].

CMUT Fabrication

There are two conventional methods to fabricate CMUT; sacrificial release process and wafer-bonding method. The first CMUT was created by using a sacrificial release process and this method has become the standard CMUT fabrication for many years. In the sacrificial release process, a cavity underneath the membrane is created by depositing or growing a sacrificial layer on the carrier substrate. The sacrificial layer is removed with an etchant after the membrane deposition. However, there are some problems associated with this technology. The surface micromachining process causes limitation on the cavity and membrane size of a CMUT device. In addition, it is hard to batch produce surface micromachined CMUTs to tight quality specifications [14]. On the other hand, wafer-bonding method is a new fabrication technique that combines bulk and surface micromachining techniques. The transducer membrane and cavity are defined on a SOI wafer and on a prime wafer, respectively. Two wafers are then bonded by using silicon direct bonding in a vacuum environment, together forming the transducer (Fig. 6) [14]. This new method improves CMUT performance since it decreases the number of process steps, device turn-around time, and increases the overall uniformity, reliability, repeatability.

Key Research Findings

Advantages of BAW Devices over SAW Devices

Acoustic biosensors generally employ BAW rather than SAW because BAW devices generate waves that mainly propagate in the shear horizontal motion. Since shear horizontal wave does not radiate significant amount of energy into liquids, it minimizes damping in the liquid operation. Besides few exceptions, the SAW sensor induces considerable surface-normal displacement that radiates compression waves into the liquid and causes excessive damping. Since biosensors detect chemicals in liquid solutions, BAW is often preferred over SAW for many biosensing applications [2].

Biological Applications of SH-APM Sensors

SH-APM sensors have been utilized in various biological applications. For example, Liren et al. [15] presented a urease biosensor in which a 0.5 mm thick ZX-$LiNbO_3$ substrate was used and a resonant frequency approximately centered at 50 MHz. APM was generated and detected by IDTs, with a period of 88 um and a center distance of 10 mm, on the same PZ crystal. The group also fabricated two pairs of IDTs on the substrate so that one would conduct biochemical reactions while the other acted as a reference. Using this device, they successfully measured urea concentrations by detecting variations in the resonant frequency [15].

SH-APM sensors have also been applied in immunochemical reactions. In order to observe antigen-antibody reactions through mass loading on the crystal surface, Dahint et al. [7] constructed an immunosensor using a 150 MHz APM device on a ZX-$LiNbO_3$ plate with a thickness of 0.5 mm. These sensors, which could detect mass as small as to 200 pg/mm^2 of crystal surface, marked a shift in resonant frequency of around 1 kHz upon antigen adsorption [7].

Biological Applications of TSM Resonators

Many biosensors that employ TSM resonators are available on the market today. Depending on their design, they can detect biological entities such as nucleic acids, viruses, bacteria, and cells. An example of TSM-based biosensor was presented by Davis et al. [16]. They used a coating of human IgG and subsequently used a TSM resonator to detect the presence of sheep antihuman IgG as marked by the decrease in the resonant frequency, signifying an increase in the mass loading from the attachment of the antibodies [16].

TSM sensors can also be used as DNA-based sensors. Okahata et al. [28] studied the use of oscillatory driven 9 or 27 MHz quartz to quantify DNA–DNA and DNA–protein interactions. They used quartz with one side specifically coated and the other side rubber cased, which was dipped into a stirred and thermostated solution of the target. Binding amounts were evaluated quantitatively as mass per unit area. Effects of probe immobilization tech-

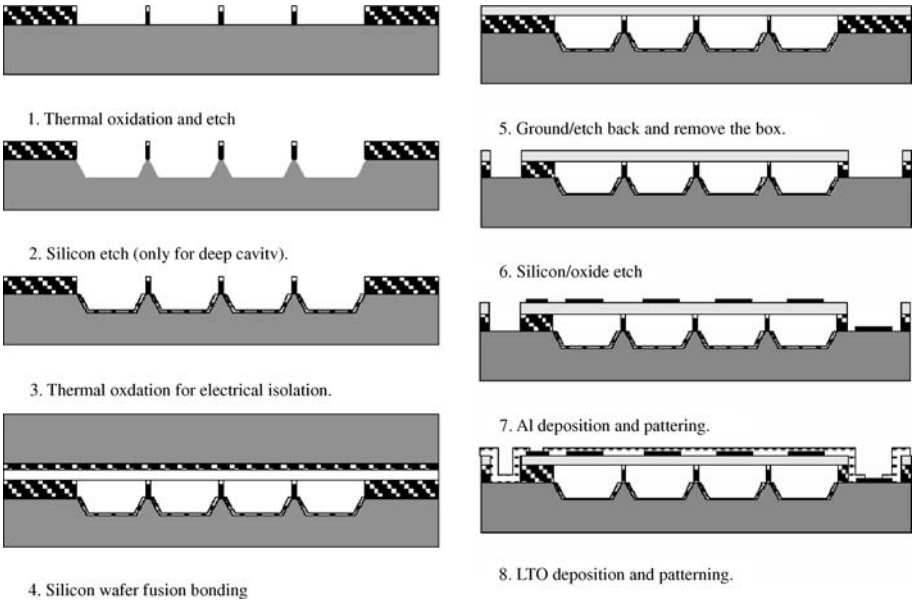

Acoustics Based Biosensors, Figure 6 Major steps of CMUT fabrication with wafer bonding method. (Reprinted with permission from Ergun et al.[24])

niques, chain lengths, ionic strengths, temperatures and mismatches on hybridization, regulatory protein binding, and electrostatic effects in DNA-binding properties of lysine containing oligopeptides were evaluated quantitatively. In addition, Tessier et al. [22] used a TSM sensor, or specifically an antibody functionalized quartz sensor, to detect human erythrocytes. Adsorption and desorption studies of antibody conjugated phages at antigen immobilized TSM resonator-surfaces in a high-throughput set-up were also performed [4].

Biological Applications of SAW

SAW devices are useful in industrial and commercial applications of chemical and biological sensing. In biological applications, these devices can be used to detect molecules by mass. A potential application of SAW devices in biology is in building immunosensors. In a study, immunosensor SAW devices were first coated with a parylene thin film to create a chemically homogeneous layer. Then, photoactive and functional groups containing dextran were immobilized and antibodies were bonded. This sensor consisted of lithium tantalate substrate with gold transducers and used to monitor urease binding [10]. This sensor was applied to monitor the amount of the urea in human urine to diagnose the onset of liver and kidney diseases [10]. In addition, another study immobilized polysaccharides to a silicon oxide surface intended for SAW. The pneumococcal polysaccharide (PPS) vaccine can immobilize via Protein A after pre-treatment of the surface with hydrochloric acid. The results show that the immobilization of PPS via Protein A increased the sensitivity of Streptococcus pneumoniae antibodies detection in human serum when compared with ELISA [17]. This study shows that SAW sensors can be used in detection of microbial contaminants in the environment.

Advantages of CMUT Devices

Piezoelectric ultrasonic transducers are used to generate and detect ultrasound over the last 30 years. This technology gives a bandwidth as high as 60–80% and a high sensitivity [18]. Nevertheless, the piezoelectric transducers have disadvantages in air or fluid-coupled applications due to the impedance mismatch between the medium and the piezoceramic material. Moreover, it is an expensive technique and shows some restrictions for the 2D arrays. On the other hand, CMUT devices became an attractive alternative to piezoelectric transducers as they have inherently low mechanical impedance associated with a thin vibrating membrane. Thin membranes that are fully supported with insulating posts on all sides and these devices have the advantage of the good mechanical properties of silicone and silicone nitride [19]. As the mechanical impedance of such thin membranes is much closer to those of fluids in a wide frequency range, CMUTs are better in immersion applications than piezoelectric devices. Moreover, CMUTs are fabricated using standard micromachining processes and provide ease of fabrication, batch production, very high level of integration and repeatability. Tak-

ing advantage of the microfabrication techniques, these devices can provide the broad bandwidth and coupling efficiency required for high performance. Furthermore, this kind of ultrasonic transducers have the ability to make complex array designs using standard photolithographic techniques that makes them usable for imaging applications [19]. A transducer with a wider band increases the resolution as well as enabling the design of the image processed. In addition, CMUTs are an alternative for intravascular imaging systems as they can be microfabricated as small 2D imaging arrays and maintain electroacoustic performance [19].

Biological Applications of CMUTS

Today's ultrasound technology has a wide range of applications in industrial and medical field, from distance measurement to medical diagnostic imaging. The fields such as dermatology, ophthalmology, and cardiovascular medicine require ultrasonic imaging systems. CMUTs enable in vivo medical imaging at high frequencies. They are also used in the microfluidics and acoustic sensing, which have applications in the biomedical engineering.

Intravascular ultrasound (IVUS) is a medical imaging technique that uses ultrasound equipment with long, thin catheters and enables visualization of blood vessels through the blood column and inner wall of blood vessels. This gives information about cardiovascular diseases. In addition, a pulse-echo phased array B-scan sector, 1D linear CMUT array was produced by Demirci et al. [19] to demonstrate the viability of CMUTs for ultrasound imaging for medical applications. 64- and 128-element 1D CMUT arrays with 100% yield and uniform element response were fabricated. For imaging experiments, resolution test phantom was used to mimic the attenuation properties of soft tissue. The image quality was found in order to show the practicality of using CMUT devices for ultrasound medical imaging due to its wide bandwidth and high sensitivity. Current l-dimensional (1D) side looking ultrasound imaging probes do not have the forward viewing capability. Demirci et al. [19] showed forward-viewing annular CMUT arrays can be used for medical imaging applications. 64-element, forward-viewing annular arrays were fabricated and designed for imaging applications in the 20 MHz range. The devices operate in the 5–26 MHz range with a fractional bandwidth of 135%. These forward-viewing annular CMUT arrays are promising tools for measuring blood flow and imaging upon being mounted on the front surface of a cylindrical catheter probe [19]. Forward-viewing IVUS enables new procedures in cardiac medicine such as viewing blood vessels, guiding stent placement, and monitoring operations in the heart [20]. In addition, researchers focused on developing a forward-looking 2D imaging arrays that can be microfabricated and integrated with electronics. CMUTs are alternative tools for 2D medical imaging arrays. In a study, ring annular CMUT was used for forward-looking IVUS imaging at 16 MHz. This 1 mm diamater arrayed CMUT device was used for volumetric imaging and they were found to have potential use in IVUS imaging catheters [20]. Another study by Knight et al. [29] modeled and designed the CMUT membranes for performance in forward looking IVUS. They used finite element analysis to calculate the electromechanical coupling coefficient, k^2 and showed that the CMUT geometry can be optimized for maximum coupling coefficient, allowing CMUT IVUS array elements to be designed with more than 60 dB/V dynamic range with 10 MHz bandwidth around 20 MHz by fabricating a 1.02 mm diameter 64-element array [20]. A recent improvent in CMUT technology produces a three dimensional ultrasound imaging system using a forward-looking ring array with a diameter of 2 mm and 64 elements each 100 μm × 100 μm in size. 3D images of several wire targets and Palmaz–Schatz stents indicate the potential of imaging with such a device. In addition, further improvements point to a promising future for forward-viewing CMUT ring arrays in intravascular imaging [21]. CMUT devices are used in the real time in vivo imaging applications with an improved performance over the existing medical ultrasound transducers. A wafer bonded CMUT probe showed a bandwidth of 130 % (3–13 MHz), which covers nearly the entire frequency range for medical ultrasound applications. Carotid artery and thyroid gland were imaged with surface and bulk-micromachined CMUT arrays and real time in vivo images were compared with a PZT array. The bandwidth and resolution performance of the surface micromachined arrays were slightly better than PZT. However, depth of penetration was not as good as in PZT. Bulk micromachined CMUT arrays showed the first real-time in-vivo images and had improved resolution and bandwidth but less depth of penetration. As a result, improved axial resolution and extremely broad bandwidth are achieved by CMUTs. Improved axial resolution will allow smaller targets to be resolved in tissue for such applications as imaging microcalcifications in the breast, small abnormalities in the thyroid, or better delineation of the intimal linings of blood vessels to search for plaque build-up [22].

Future Directions for Research

Advancements made over the past decades have culminated in the initiation and development of acoustic wave biosensors. The ability to detect biological molecules by

these sensors may contribute to treatment of many diseases such as HIV and cancer. In addition, these devices are promising in medical imaging given their ability to generate high-resolution pictures in real time. However, there are still limitations to some of these devices that can be surmounted through future research and though the potential of the application of these devices to biological situations has been recognized, more work is left to be done in order to employ them on a wider scale. Below are some limitations and potentials of the devices.

SAW Devices

There are a number of potential limitations with the SAW sensors as they are today. One limitation is that SAW sensors are sensitive to a variety of parameters [8]. In addition, the intensity of an acoustic wave can decrease in biological solution such that the sensing system may not work efficiently. Furthermore, many SAW devices that are used in the gas-sensing applications may not be used to detect molecules in the liquid phase. When a fluid contacts the SAW surface, the longitudinal wave component pumps a compression wave into the fluid [2]. In air, the energy losses are not too effective. However, in many liquids, all the energy is pumped out of the acoustic wave before it reaches the device's receiving transducer. SAW devices can perform well in liquids when they rely on surface waves with no longitudinal components like horizontally polarized shear waves, surface transverse waves, and the guided acoustic waves called "Love waves" [2]. Recent advances in liquid sensors and immunoassays improved the detection limits. In addition, surface technologies like functionalization with fluorescent probes, DNA, and enzymes increased the use of SAW devices in liquid samples [7]. There are also radar-type SAW sensors for high-voltage applications that detect at long distances. These sensors cannot be used scans of wider areas due to two main limitations. According to the radar equation, the radiofrequency signal changes with the fourth power of the distance between the radar unit and SAW sensor. As a result, high signal attenuation is governed by this equation. Second, only a few echo sounds can be distinguished because all sensors in the detection range respond immediately. Attaining this requires differentiated sensors that responds within different time slots, and multiple sensors can be used with a limited number of reflectors and limited identity-code capacity [25].

In addition, generation of acoustic waves in microstructures requires various processes and technologies, with compatibility as one of the main limitations in the development of smart sensors. Restrictions of manual handling and fabrication process limit minimum thickness of the devices to be about 100 microns. Adoption of silicon fabrication opens the possibility for the integration of the acoustic devices and electronic driving circuitry, leading to the development of smart sensors. This technique involves localization of specific fabrication steps to common areas to minimize the total number of process steps in the fabrication process as well as to maintain SAW and Lamb wave device integrity and quality [26].

Most of today's acoustic wave generation and focusing apparatus suffer from these further limitations: The piezoelectric arrays are expensive, and it is hard to get high-level, well-distributed intensities. In addition, shocks are generated at a rate of one or two shocks per second, whereas extracorporeal shockwave treatment (ESWT) typically requires thousands of shocks per treatment. Acoustic lenses are mostly fragile and non-effective for larger apertures. Moreover, electrohydraulic approach has disadvantages of non-uniform discharges, pain and high noise level.

BAW Devices – TSM Resonator

The limitations of TSM resonators are mostly related with the experimental setup, accuracy in modeling the sensor and physical behavior of a viscoelastic polymer. Researchers should be careful in model approximations, parameter estimations, and measurement errors. For acoustically thin polymers, the thickness can be calculated with a small error, but the shear moduli can hardly be extracted from measurements due to negligible influence on the sensor behavior. On the other hand, the coating thickness should be known because of the existence of multipleidentical solutions for acoustically thick polymers [27]. In addition, for detailed interpretation of sensor response in liquid requires more sophisticated experimental setup [4]. In addition, mechanical, optical, and electrochemical properties are helpful to characterize interactions at biological surfaces and interfaces. However, the needed equipment are expensive. While miniaturized quarts arrays seem to present a solution for low cost sensor setups, miniaturization has its limitations because small electrode areas can load enough molecules to achieve measurable frequency shifts. As a solution, combination of automatized pipetting systems, microfluidics, integrated sensor arrays and multicomponent data analysis may open the way towards high throughput screening with acoustic wave sensors [4].

Two major challenges are present in the application of TSM resonator as a biosensor. First, cross reactions such as unspecific protein adsorption affects the accuracy of the results. This limits the resonator's use to binding sites that specifically bond to the targeted biological molecules

and poses a significant disadvantage in environments containing various compounds. Second, since the resonator only responds to mass loadings, the analysis cannot differentiate this signal from other factors that can affect the resonant frequency such as viscoelasticity and acoustic coupling effect. This leads to a disagreement between the experimental and theoretical values of mass uptake, an error that needs to be accounted for by researchers [4]. Immunochemical analyzes or nucleic acid hybridization results of TSM resonators should always be coupled with a reference analysis method. In addition, dry- and wet-coated TSM resonators may not give the same results due to changes in viscoelasticity, so calibration should be done in the sensing medium during nucleic acid analyzes. Complexation of DNA may limit the flexibility of the molecule strands and ionic strength changes or interaction with the surface might vary extension and shape of the molecule. These may change viscoelastic behavior and produce erroneous results from TSM resonators [4].

CMUTs

CMUTs have the potential to make ultrasound a far more versatile and important imaging modality. This technology has made advances in acoustic matching and the microminiaturization of electronics. It enables higher frequency imaging, allows clinicians to view small features in the body, and is useful for ultrasound imaging especially in the area of volumetric in vivo imaging, intravascular, and intracardiac research.

Cross References

- ► Biosensors Using Atomic Force Microscopes
- ► Biosensors Using Lasers
- ► Biosensors Using Magnetics
- ► Biosensors Using Surface-Enhanced Raman Scattering
- ► Biosensor
- ► Piezoelectric

References

1. Lec RM, Lewin PA (1999) Acoustic wave biosensors, Engineering in Medicine and Biology Society, 1998. Proceedings of the 20th Annual International Conference of the IEEE. 6:2779–2784
2. Drafts B (2001) Acoustic wave technology sensors, Microwave Theory and Techniques, IEEE Transactions on 49(4):795–802
3. piezoelectricity Encyclopædia Britannica. (2006) EncyclopæDiaBritannica Online, 25 Aug. 2006, http://search.eb.com/eb/article-9059986
4. Kaspar M et al (2000) Thickness shear mode resonators ('mass-sensitive devices') in bioanalysis. Fresenius' J Anal Chem 366(6–7):602–10
5. Sauerbrey G (1959) Use of Quartz Crystal Vibrator for Weighting Thin Films on a Microbalance. Z Phys 155:206
6. Lin Z, Yip CM, Joseph IS, Ward MD (1993) Operation of an Ultrasensitive 30-MHz Quartz Crystal Microbalance in Liquids. Anal Chem 65:1546–1551
7. Dahint R et al (1994) Acoustic Plate Mode Sensor for Immunochemical Reactions. Anal Chem 66(18):2888–92
8. Milstein L, Das P (1977) Spread Spectrum Receiver Using Surface Acoustic Wave Technology. Communications, IEEE Trans 25(8):841–847
9. McGill RA, Chung R, Chrisey DB, Dorsey PC, Matthews P, Pique A, Mlsna TE, Stepnowski JL (1998) Performance optimization of surface acoustic wave chemical sensors. Ultrasonics, Ferroelectrics and Frequency Control, IEEE Trans 45(5):1370–1380
10. Lange K, Bender F, Voight A, Gao H, Rapp M (2003) A Surface Acoustic Wave Biosensor Concept with Low Flow Cell Volumes for Label-Free Detection. Anal Chem 75(20):5561–5566
11. Campbell CK (1984) Simplified Computer-Aided Fabrication of SAW Transducer Pattern Masks. Sonics and Ultrasonics, IEEE Trans 31(3):185–186
12. Chen Y, Emanetoglu NW, Saraf G, Wu P, Lu Y, Parekh A, Merai V, Udovich E, Lu D, Lee DS, Armour EA, Pophristic M (2005) Analysis of SAW properties in ZnO/Al/sub x/Ga/sub 1-x/N/c-Al/sub 2/O/sub 3/ structures. Ultrasonics, Ferroelectrics and Frequency Control, IEEE Trans 52(7):1161–1169
13. Ergun AS, Yaralioglu GG, Khuri-Yakub BT (2003) Capacitive micromachined ultrasonic transducers: theory and technology. J Aerosp Eng 16:76–84
14. Huang Y, Ergun AS, Hæggström E, Badi MH, and Khuri-Yakub BT (2003) Fabricating capacitive micromachined ultrasonic transducers with wafer-bonding technology. J Microelectromech Syst 12:128–37
15. Liren W, Xue W, Sixin W, Xuesong Y, Yuquan C (1996) A two-acoustic-waveguide-channel SH-APM urease biosensor. Engineering in Medicine and Biology Society. 1:85–86
16. Davis KA, Leary TR (1989) Continuous liquid-phase piezoelectric biosensor for kinetic immunoassays. Anal Chem 61(11):1227 – 1230
17. Dutra RF, Castro CMHB, Azevedo CR, Vinhas E, Malague E, Melo EHM, Lima Filho JL, Kennedy JF (2000) Immobilization of pneumococcal polysaccharide vaccine on silicon oxide wafer for an acoustical biosensor. Biosens Bioelectron 15(9–10):511–514
18. Caliano G, Carotenuto R, Cianci E, Foglietti V, Caronti A, Iula A, Pappalardo M (2005) Design, fabrication and characterization of a capacitive micromachined ultrasonic probe for medical imaging. IEEE Trans 52(12):2259–2269
19. Demirci U, Ergun AS, Oralkan O, Karaman M, Khuri-Yakub BT (2004), Forward-Viewing CMUT arrays for medical imaging. IEEE Trans Ultrason Ferroelect Freq Contr 55:887–895
20. Yeh DT, Oralkan O, Wygant IO, O'Donnell M, Khuri-Yakub BT (2006) 3-D ultrasound imaging using a forward-looking CMUT ring array for intravascular/intracardiac applications. IEEE Trans Ultrason Ferroelectr Freq Control 53(6):1202–11
21. Jakubik W, Urbanczyk M, Opilski A (2001) Sensor properties of lead phthalocyanine in a surface acoustic wave system. Ultrasonics 39(3):227–232
22. Tessier L et al (1997) Potential of the thickness shear mode acoustic immunosensors for biological analysis. Analytica Chimica Acta 347:207–17
23. Degertekin LF, Guldiken OR, Karaman M (2005) Micromachined capacitive transducer arrays for intravascular ultrasound. Proc SPIE Int Soc Opt Eng 5721:104

24. Huang Y, Ergun AS, Hæggström E, Badi MH, Khuri-Yakub BT (2003) Fabricating capacitive micromachined ultrasonic transducers with wafer-bonding technology. J Microelectromech Syst 12:128–37
25. Scholl G, Schmidt F, Wolff U (2001) Surface Acoustic Wave Devices for Sensor Applications. Phys Stat Sol (a) 185(1):47–58
26. Hoummady M, Campitelli A, Wlodarski W (1997) Acoustic wave sensors: design, sensing mechanisms and applications. Smart Mater Struct 6:647–657
27. Behling C, Lucklum R, Hauptmann P (1997) Possibilities and limitations in quantitative determination of polymer shear parameters by TSM resonators. Sens Actuators A 61:260–266
28. Okahata Y, Matsunobu Y, Ijiro K, Mukae M, Murakami, Makino K (1992) Hybridization of Nucleic Acids Immobilized on a Quartz Crystal Microbalance. J Am Chem Soc 114:8299–8300
29. Knight JG, Degertekin FL (2002) Capacitive micromachined ultrasonic transducers for forward looking intravascular imaging arrays. Ultrasonics Symposium, 2002, Proceedings. 2:1079–1082

Acoustic Separation

► Particle Manipulation Using Ultrasonic Fields

Acoustic Streaming

YONG KWEON SUH, SANGMO KANG
Dong-A University, Busan, Korea
yksuh@dau.ac.kr

Synonyms

Steady streaming; Eulerian streaming

Definition

Acoustic streaming is a secondary steady flow generated from the primary oscillatory flow. It includes not only the Eulerian streaming flow caused by the fluid dynamical interaction but also the Stokes drift flow which arises from a purely kinematic viewpoint.

Overview

Acoustic streaming originates from the acoustics. When the compressible fluid experiences a high-frequency oscillation driven by a certain source of sound, the nonlinear interaction causes a steady current in the field. This phenomenon is usually referred to as acoustic streaming. However, it was found that even an incompressible fluid can produce such steady streaming when the fluid oscillates adjacent to a certain obstacle or an interface. So, as pointed out by Riley [1], the term *acoustic streaming* is misleading. Instead of acoustic streaming he insisted on using *steady streaming* to encompass the case of incompressible fluid. *Acoustic streaming* in this article means both of these effects.

Another important issue that must be addressed is, whether or not the Stokes drift flow should be included in the streaming flow category. The Stokes drift flow is purely kinematic and so it is basically different from the Eulerian streaming flow, which is driven by the time average of the Reynolds stress term. However, the mass-transport effect given by the Stokes drift flow is not weaker than the Eulerian streaming. On the contrary, in the case of a progressive wave, the Stokes drift flow plays a dominant role (e. g., application of flexural plate waves to pumping and mixing in microfluidics [2]). Therefore, the Stokes drift flow must be understood as a kind of streaming flow.

Unfortunately, little is known about the historical background to the study of acoustic streaming. Therefore, instead of trying to give the historical background of the general concept, we will briefly survey the modeling and applications of acoustic streaming in microfluidics. A survey of steady streaming flow has been given by Riley [1].

In the early period, study mainly focused on the acoustic streaming of compressible fluids. The simplest and seminal phenomenon associated with acoustic streaming is the *quartz wind*. When the air experiences a high-frequency oscillation given by an ultrasound source, a progressive wave is established in the air. Due to the attenuation of the wave, a nonzero time averaged Reynolds stress is built in the region close to the sound source, and this stress pushes the air in the direction of wave propagation. The resultant wind is called a quartz wind. Lighthill [3] has provided a physical and simple analytical treatment of this steady streaming flow. Another important phenomenon is the so-called Kundt's dust pattern. When the air within a duct receives a standing wave, a nonzero time average of the Reynolds stress is built inside the duct. Due to the interaction between the air and the duct wall, a steady recirculating flow takes place within the duct. The net effect is that dust or particles accumulate at nodes.

On the other hand, researchers interested in mass transport in water waves have shown that a similar phenomenon occurs for incompressible flow (see [4] for an example). The salient feature is when an obstacle oscillates with high frequency in the quiescent viscous fluid. In this case the steady streaming emerges from both sides of the obstacle along the oscillating direction at small viscosity [5].

In this article, we will describe in some detail the fundamentals of three types of streaming flows associated with the microfluidic applications. First, the quartz wind which corresponds to the one-dimensional compressible flow will be introduced. Second, the Eulerian streaming flow

in two-dimensional space will be considered. Kundt's dust phenomenon will also be explained. Finally, we address the flexural plate wave and its net effect, i. e., the Stokes drift flow.

Basic Methodology

One-Dimensional Compressible Flow Model – Quartz Wind

In this and next subsections we closely follow the review by Riley [1] to describe the physical mechanism of acoustic streaming. We first consider the case when the sound is generated from a source and travels along a certain direction, say the x^*-direction, in a space. The governing equation for the motion of the compressible fluid is

$$\frac{\partial \rho^*}{\partial t^*} + \frac{\partial \rho^* u^*}{\partial x^*} = 0 \tag{1a}$$

$$\frac{\partial u^*}{\partial t^*} + u^* \frac{\partial u^*}{\partial x^*} = -\frac{1}{\rho^*}\frac{\partial p^*}{\partial x^*} + \frac{4}{3}\nu \frac{\partial^2 u^*}{\partial x^{*2}} \tag{1b}$$

where u^* is the flow velocity, p^* the pressure, t^* the time, ρ^* the density of the fluid and ν the kinematic viscosity of the fluid. The fluid particle is assumed to oscillate back and forth with amplitude A_0, frequency ω, and wavelength λ. We then take $1/\omega$, $\lambda/2\pi$, $A_0\omega$, and $\rho_0^* A_0 \omega^2 (\lambda/2\pi)$ as the reference quantities for the time, length, velocity, and pressure, respectively. Further, we expand the density as

$$\rho^* = \rho_0^* \left(1 + \varepsilon \rho_0 + \varepsilon^2 \rho_1 + \ldots\right) \tag{2}$$

where ρ_0^* corresponds to the undisturbed fluid density. We also expand the dimensionless velocity and pressure, respectively, as

$$u = u_0 + \varepsilon u_1 + \varepsilon^2 u_2 + \ldots \tag{3a}$$

$$p = p_0 + \varepsilon p_1 + \varepsilon^2 p_2 + \ldots \tag{3b}$$

Then the leading-order equations of Eqs. (1a) and (1b) for the small value of the parameter ε become

$$\frac{\partial \rho_0}{\partial t} + \frac{\partial u_0}{\partial x} = 0 \tag{4a}$$

$$\frac{\partial u_0}{\partial t} = -\frac{\partial p_0}{\partial x} + \frac{4}{3}\delta \frac{\partial^2 u_0}{\partial x^2} \tag{4b}$$

where the variables without an asterisk are dimensionless. Here, the two dimensionless parameters are

$$\varepsilon = \frac{A_0}{\lambda/2\pi}, \quad \delta = \frac{\nu}{\omega(\lambda/2\pi)^2} \tag{5}$$

which can be considered as the dimensionless amplitude of the flow motion and the inverse of the Reynolds number, respectively. As usual, these parameters are assumed to be small. To solve this system of equations we eliminate the perturbed density in Eq. (4a) and the pressure in Eq. (4b) by using the definition of sound

$$\frac{\partial p^*}{\partial \rho^*} = c^{*2} = \omega^2 (\lambda/2\pi)^2 \tag{6}$$

We then have

$$\frac{\partial^2 u_0}{\partial t^2} - \frac{\partial^2 u_0}{\partial x^2} - \frac{4}{3}\delta \frac{\partial^3 u_0}{\partial t \partial x^2} = 0 \tag{7}$$

The solution of this equation is

$$u_0 = \exp(-2\delta x/3)\cos(x - t) \tag{8}$$

Notice that the basic mode is progressive. We need the next higher-order equation of Eq. (1b), which is

$$\frac{\partial u_1}{\partial t} + \frac{\partial p_1}{\partial x} - \frac{4}{3}\delta \frac{\partial^2 u_1}{\partial x^2} = -u_0 \frac{\partial u_0}{\partial x} \tag{9}$$

The right-hand side term can be understood as a dimensionless force per unit mass. Substituting Eq. (8) into the right-hand side gives

$$-u_0 \frac{\partial u_0}{\partial x} = \exp(-4\delta x/3) \left[\frac{\delta}{3} + \frac{\delta}{3}\cos 2(x - t) + \frac{1}{2}\sin 2(x - t)\right]$$

Taking the time average over one period (the operation to be denoted as $\langle\rangle$) of this provides

$$-\left\langle u_0 \frac{\partial u_0}{\partial x} \right\rangle = \frac{\delta}{3}\exp(-4\delta x/3) \tag{10}$$

which plays a role as the driving force for the generation of the steady flow $\overline{u}_1$. Taking the time average of Eq. (9) results in

$$\frac{\partial \overline{p}_1}{\partial x} - \frac{4}{3}\delta \frac{\partial^2 \overline{u}_1}{\partial x^2} = -\left\langle u_0 \frac{\partial u_0}{\partial x} \right\rangle \tag{11}$$

It should be noted that the term (10) can be understood as a kind of body force. Lighthill [3] has presented solutions of this system of equations for the case in which the force (10) acts as a point source in an infinite space. It is seen that when the viscosity is low enough (at high streaming Reynolds numbers) the flow from the source is like a jet as shown in Fig. 1. This flow is sometimes called the *quartz wind*. The term *acoustic streaming* refers

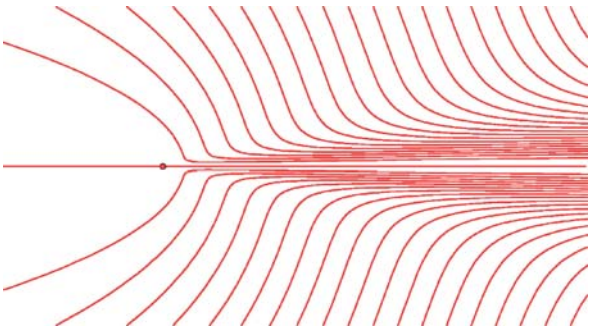

Acoustic Streaming, Figure 1 Acoustic streaming *quartz wind* generated from a point source of ultrasound

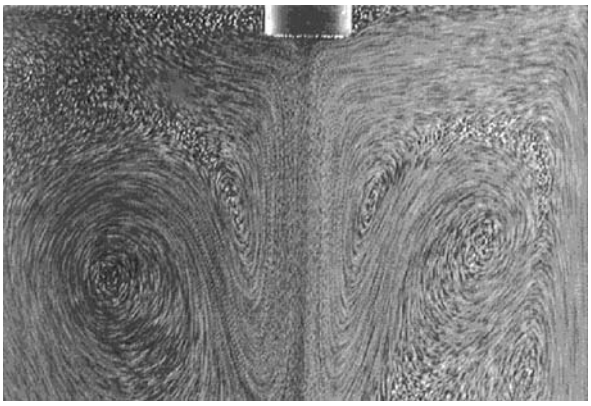

Acoustic Streaming, Figure 2 Acoustic streaming generated from an actual ultrasonic transducer

to this flow in the case of ultrasound. As can be seen from Eq. (10), the driving force for this current vanishes when there is no attenuation, i. e., when $\delta = 0$. Therefore we can say that the acoustic streaming in for the case of ultrasound in a compressible fluid is attributed to the attenuation of sound. The photograph in Fig. 2 clearly shows the streaming flow ejected by the transducer that creates the ultrasound.

On the other hand, we can also calculate the Stokes drift velocity from the solution of Eq. (8). We can follow a certain fluid particle's path $x(x_0, t)$, where x_0 is a reference point independent of the time. From the definition of the flow velocity we can write

$$\frac{dx}{dt} = \varepsilon u \tag{12}$$

We substitute Eq. (8) into the right-hand side of this and let $x = x_0 + \varepsilon x_1(t)$. We then have

$$x_1 = -\exp(-2\delta x_0/3)\sin(x_0 - t) \tag{13}$$

and

$$u_0 = -\exp(-2\delta x_0/3)\cos(x_0 - t) + \left(\frac{\partial u_0}{\partial x}\right)_{x=x_0} \varepsilon x_1 \tag{14}$$

Here again the last term contains the steady component and it becomes

$$\varepsilon u_\mathrm{d} = \frac{1}{2}\varepsilon \exp(-4\delta x_0/3) \tag{15}$$

which is known as the Stokes drift velocity. The steady streaming flow $\varepsilon\overline{u}_1$ given by the solution of Eq. (11) is called the Eulerian streaming flow. Compared with the Eulerian streaming flow, the Stokes drift flow is confined in a region close to the sound source, i. e., within the region $x = O(1/\delta)$. Actually this region corresponds to the one that the force (10) acts upon. That is, within this region the steady flow velocity is composed of the Eulerian streaming velocity and the Stokes drift velocity

$$u_\mathrm{L} = \varepsilon\overline{u}_1 + \varepsilon u_\mathrm{d} \tag{16}$$

which is known as the Lagrangian velocity. Beyond this region the Stokes drift flow vanishes and only the Eulerian streaming exists. In many cases the Stokes drift velocity is ignored, but when the location of interest is not far from the sound source it should be considered. In general, the Stokes flow is expected to occur only when the primary wave is progressive, not when it is standing.

Eulerian Streaming

Even the incompressible fluid can also give rise to Eulerian streaming flow when a solid obstacle is in contact with the oscillating fluid. Consider a two-dimensional incompressible flow around a solid body governed by the following dimensionless equations:

$$\nabla \cdot \mathbf{u} = 0 \tag{17a}$$

$$\frac{\partial \mathbf{u}}{\partial t} + \varepsilon \mathbf{u} \cdot \nabla \mathbf{u} = -\nabla p + \frac{1}{\mathrm{Re}}\nabla^2 \mathbf{u} \tag{17b}$$

where $\mathbf{u} = (u, v)$ and ∇ is the two-dimensional gradient operator. We use $1/\omega$, L, $A_0\omega$ and $\rho^* A_0\omega^2 L$ as the reference quantities for the time, length, velocity and pressure, respectively. Note that the reference length L used here represents a typical dimension of the obstacle. The Reynolds number Re defined as

$$\mathrm{Re} = \frac{\omega L^2}{\nu}$$

is assumed to be large. For the small value of ε, we expand

$$(\mathbf{u}, p) = (\mathbf{u}_0, p_0) + \varepsilon(\mathbf{u}_1, p_1) + \dots . \tag{18}$$

The leading-order equation of Eq. (17b) is then

$$\frac{\partial \mathbf{u}_0}{\partial t} = -\nabla p_0 \tag{19}$$

Therefore the leading-order solution is of potential flow. Moreover the solutions can take a separable form, e. g.

$$\mathbf{u}_0 = \mathbf{f}(x, y)\exp(\mathrm{i}t) \tag{20}$$

where the complex functions $\mathbf{f}$ must satisfy the continuity equation (17a) and $\mathrm{i} = \sqrt{-1}$ denotes the imaginary unit. Note that the inviscid region governed by these equations comprises most of the flow domain except the thin layer near the solid boundary.

Since the potential flow solution (Eq. (20)) does not satisfy the no-slip condition on the solid surface, we must consider a thin layer (called the Stokes layer) adjacent to the surface $n = 0$, where n refers to the local coordinate normal to the wall. In this thin layer, we use the strained coordinate Y defined as

$$n = \sqrt{2/\mathrm{Re}}\, Y$$

We also use the velocity components U and V along the local coordinates s and n, respectively (the coordinate s is along the surface). Then the boundary layer equation becomes

$$\frac{\partial U}{\partial t} - \frac{\partial u_\mathrm{e}}{\partial t} = \frac{1}{2}\frac{\partial^2 U}{\partial Y^2} - \varepsilon\left(U\frac{\partial U}{\partial s} + V\frac{\partial U}{\partial n}\right) \tag{21}$$

where $u_\mathrm{e}(s)$ denotes the tangential component of the potential flow velocity evaluated at the solid surface. We expand the velocity components as before.

$$(U, V) = \left(U_0, \sqrt{2/\mathrm{Re}}V_0\right) + \varepsilon\left(U_1, \sqrt{2/\mathrm{Re}}V_1\right) + \dots \tag{22}$$

The leading-order equation is

$$\frac{\partial U_0}{\partial t} - \frac{\partial u_{0\mathrm{e}}}{\partial t} = \frac{1}{2}\frac{\partial^2 U_0}{\partial Y^2}$$

whose solution takes the following form:

$$U_0 = u_{0\mathrm{e}}(s)\left[1 - \exp(-(1+\mathrm{i})Y)\right]\exp(\mathrm{i}t) \tag{23}$$

The normal component V_0 can also be obtained from the continuity equation. Note that this flow is still time periodic. The $O(\varepsilon)$ equation (21) then becomes

$$\frac{\partial U_1}{\partial t} - \frac{\partial u_{1\mathrm{e}}}{\partial t} = \frac{1}{2}\frac{\partial^2 U_1}{\partial Y^2} - \left(U_0\frac{\partial U_0}{\partial s} + V_0\frac{\partial U_0}{\partial Y}\right) \tag{24}$$

Here our interest is the time independent flow. Taking the time average of the above equation over one period of oscillation gives

$$\frac{1}{2}\frac{\partial^2 \overline{U}_1}{\partial Y^2} = \left\langle U_0\frac{\partial U_0}{\partial s} + V_0\frac{\partial U_0}{\partial Y}\right\rangle \tag{25}$$

The solution of this equation yields the streaming velocity at the edge of the boundary layer,

$$\overline{U}_{1\infty} = -\frac{3}{8}\left[(1-\mathrm{i})u_{0\mathrm{e}}^{\#}\frac{\mathrm{d}u_{0\mathrm{e}}}{\mathrm{d}s} + (1+\mathrm{i})u_{0\mathrm{e}}\frac{\mathrm{d}u_{0\mathrm{e}}^{\#}}{\mathrm{d}s}\right] \tag{26}$$

where the superscript # denotes the complex conjugate. This velocity then acts as a boundary condition for the exterior bulk region. The governing equation of the steady streaming flow takes the following form [1]:

$$(\overline{\mathbf{u}} + \overline{\mathbf{u}}_\mathrm{d})\cdot\nabla\overline{\mathbf{u}} = -\nabla\overline{p} + \frac{1}{\mathrm{Re}_\mathrm{s}}\nabla^2\overline{\mathbf{u}} \tag{27}$$

where Re_s is the streaming Reynolds number based on the streaming velocity at the edge of the Stokes layer; $\mathrm{Re}_\mathrm{s} = \varepsilon^2\mathrm{Re}$. This equation looks very similar to the Navier–Stokes equation, but here the convective velocity is replaced by the Lagrangian velocity $\overline{\mathbf{u}}_\mathrm{L} = \overline{\mathbf{u}} + \overline{\mathbf{u}}_d$.

The above formulation is effective and suitable when the streaming Reynolds number is large so that the Reynolds stress action is confined within the thin Stokes layer. In the microfluidic application, however, Re_s is usually small. So, the Reynolds stress term may be added to the streaming-flow equation (27) so that

$$(\overline{\mathbf{u}} + \overline{\mathbf{u}}_\mathrm{d})\cdot\nabla\overline{\mathbf{u}} = -\nabla\overline{p} + \frac{1}{\mathrm{Re}_\mathrm{s}}\nabla^2\overline{\mathbf{u}} - \mathbf{F} \tag{28a}$$

$$\mathbf{F} = \langle\,(\mathbf{U}_0\cdot\nabla)\mathbf{U}_0 + \mathbf{U}_0(\nabla\cdot\mathbf{U}_0)\,\rangle \tag{28b}$$

where the second term within $\langle\,\rangle$ on the right-hand side is nonzero for the compressible fluid case; for the compressible fluid case Eq. (28a) itself must be modified. This means that for the case with a low streaming Reynolds number, Eq. (28a) must be solved over the whole domain including the Stokes layer. Another important point for the incompressible flow is that the Reynolds stress vanishes when the primary oscillating flow is of the progressive-wave type. On the other hand, it should be noted that in

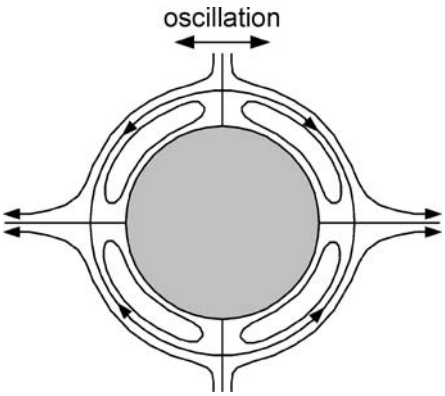

Acoustic Streaming, Figure 3 Sketch of the flow structure of the Eulerian streaming around a circular cylinder oscillating at a high frequency in a viscous fluid

the microfluidic area no literature has taken into account the Stokes drift flow in the convecting velocity (i. e., the velocity $(\overline{\mathbf{u}}+\overline{\mathbf{u}}_{\mathrm{d}})$ in Eq. (28a)) in the numerical simulation of the streaming flow.

We can experience a typical example of the Eulerian streaming flow around a circular cylinder [5]. Here, the fluid surrounding the cylinder oscillates with high frequency; or the cylinder may oscillate in the otherwise quiescent fluid without fundamental difference in the results. The steady flow within the Stokes layer at high streaming Reynolds numbers shows four-cell structure around the circular cylinder as shown in Fig. 3. There are two streams coming out of the cylinder from both sides in the direction of oscillation.

Kundt's dust pattern manifests another simple example of the Eulerian streaming flow given by the two-dimensional standing wave in a duct. When an acoustic standing wave is established in the duct with a compressible fluid, the steady streaming reveals four-cell structure over a half wavelength (or over the space between two neighboring nodes) as shown in Fig. 4. Near the duct wall, the steady streaming is toward the nodes, and near the duct center it is coming out of the nodes. Therefore dust within the duct should cluster near the nodal points of the standing wave. The detailed solution for this case has been given by Riley [1].

Stokes Drift Flow

Usually, by acoustic streaming we mean *Eulerian* streaming. However, the recent application of the flexural plate wave in microfluidics implies that the Stokes drift flow should also be considered as a type of steady streaming flow, because the net effect in the fluid transport is not discernable between the two. Here we derive the equations

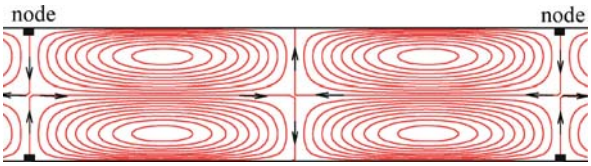

Acoustic Streaming, Figure 4 Eulerian streaming flow occurring between two parallel plates when a standing wave takes place inside the duct. Distance between the nodes corresponds to a half wavelength of the standing wave

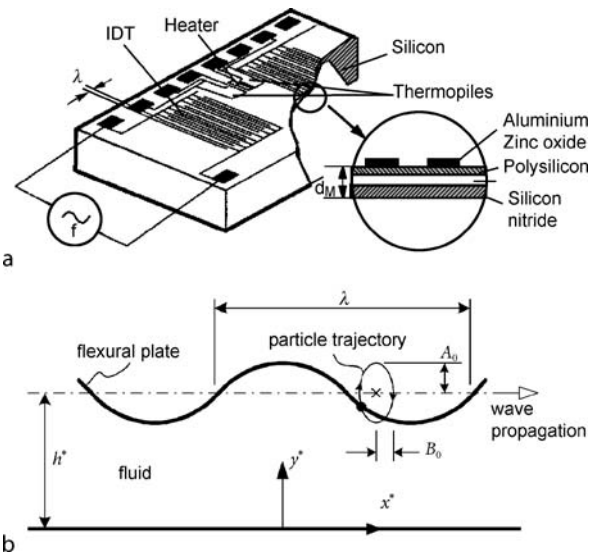

Acoustic Streaming, Figure 5 Microfluidic device utilizing the flexural plate wave. (**a**) Fabricated device; (**b**) shape of the flexural plate and the coordinates for analysis

as well as the solutions for the Stokes drift flow given by the flexural plate wave. The case of one-dimensional compressible flow has already been treated in this article.

Consider a viscous fluid confined between a flat wall at $y^* = 0$ and a flexural plate at $y^* = h^*$. The flexural plate oscillates showing a traveling wave with a high frequency ω by a well established piezoelectric vibration system. Fig. 5 illustrates the geometry of the flow model investigated in this article. The wavelength is λ and the wave propagation speed is $c^* = \omega\lambda/2\pi$. A particle attached on the flexural plate describes an ellipse with major A_0 and minor $B_0 = rA_0$ rotating clockwise when the wave travels toward the right-hand side as shown in Fig. 5 [2]. The ratio r is given from $r = \pi d/\lambda$, where d is the membrane thickness. A typical value of r is 0.1. The spatial coordinate x^* is along the wave propagation direction and y^* normal to it.

As before we use $1/\omega$ as the time scale, $\lambda/2\pi$ as the length scale, $A_0\omega$ as the velocity scale and $\rho A_0\omega^2\lambda/2\pi$ as

the pressure scale, then the dimensionless continuity and momentum equations take the form given in Eqs. (17a) and (17b). The equations for the particle motion on the flexural plate are

$$\delta x = -r\varepsilon \sin(x_0 - t) \tag{29a}$$

$$\delta y = \varepsilon \cos(x_0 - t) \tag{29b}$$

As a typical example, for $\lambda = 100\,\mu\text{m}$, $d = 3\,\mu\text{m}$, $A_0 = 6\,\text{nm}$, and the frequency $\omega/2\pi = 3\,\text{MHz}$, we have $A_0\omega = 113\,\text{mm/s}$, $\varepsilon = 3.8 \times 10^{-4}$, and $\text{Re} = 4760$. The boundary conditions are

$$u = 0 \qquad \text{at } y = 0 \tag{30a}$$

$$v = 0 \qquad \text{at } y = 0 \tag{30b}$$

$$u = r\cos(x - t) \qquad \text{at } y = h \tag{30c}$$

$$v = \sin(x - t) \qquad \text{at } y = h \tag{30d}$$

where h is the dimensionless depth of the fluid layer. The velocity conditions, Eqs. (30c) and (30d), are derived from Eqs. (29a) and (29b), respectively. In this derivation we simply replaced x_0 by x, which is valid for small r; later we will consider the higher-order effect.

As before, we neglect the nonlinear term in Eq. (17b). We also assume that Re is very large. Equation. (17b) then becomes

$$\frac{\partial \mathbf{u}}{\partial t} = -\nabla p \tag{31}$$

This indicates that the velocity field can be described by a potential function $\phi(x, y, t)$ in such a way that $\mathbf{u} = \nabla\phi$. As usual, this inviscid solution must satisfy the boundary condition for the normal component of the velocity at each of the walls but not the tangential component. This is the most important part of the analysis, because otherwise the leading-order solution is not of the progressive-wave type. Applying the conditions given in Eqs. (30b) and (30d) to the Laplace equation $\nabla^2\phi = 0$ and solving for ϕ, we obtain $\phi = (\cosh y/\sinh h)\sin(x - t)$ and

$$u = \frac{\cosh y}{\sinh h}\cos(x - t) \tag{32a}$$

$$v = \frac{\sinh y}{\sinh h}\sin(x - t) \tag{32b}$$

The bulk flow solution given by Eqs. (32a) and (32b) does not satisfy the condition for the tangential component of the velocity on the walls. So, we must expect boundary layers near each of the walls. First, near the top wall, $y = h$, we use the strained variable $Z = (h - y)\sqrt{\text{Re}/2}$. Then we obtain the appropriate x-momentum equation and solve for u to obtain

$$u = \coth h \cos(x - t) + (r - \coth h)\exp(-Z)\cos(x + Z - t) \tag{33}$$

A similar process leads to the following solution for u in the bottom boundary layer:

$$u = \frac{1}{\sinh h}\left[\cos(x - t) - \exp(-Y)\cos(x + Y - t)\right] \tag{34}$$

where $Y = y\sqrt{\text{Re}/2}$.

The analytical solutions obtained so far imply that the flow field driven by the oscillating flexural plate is progressive. This means that the Reynolds stress should vanish and so there should be no Eulerian streaming. On the other hand, it produces the nonzero Stokes drift flow. First we consider the bulk flow. Into the definition of the velocity components u and v, i. e., $\mathrm{d}x/\mathrm{d}t = \varepsilon u$ and $\mathrm{d}y/\mathrm{d}t = \varepsilon v$, we substitute Eqs. (32a) and (32b). Assuming the variables x and y on the right-hand side are constant, i. e. $x = x_0$ and $y = y_0$, we can integrate the equations to obtain

$$x = x_0 - \varepsilon\frac{\cosh y_0}{\sinh h}\sin(x_0 - t) \tag{35a}$$

$$y = y_0 + \varepsilon\frac{\sinh y_0}{\sinh h}\cos(x_0 - t) \tag{35b}$$

Now we substitute Eqs. (35a) and (35b) into Taylor expansions for u and v, i. e., Eqs. (32a) and (32b) about $(x, y) = (x_0, y_0)$ and take the time average over one period to obtain the steady velocity components $\overline{v} = 0$ and

$$\overline{u} = \frac{\varepsilon}{2\sinh^2 h}(\cosh^2 y + \sinh^2 y) \tag{36}$$

Next, we consider the top boundary layer. After some algebra we obtain $\overline{v} = 0$ and

$$\begin{aligned}\overline{u} = \frac{\varepsilon}{2}\Bigg\{&\left[\frac{\cosh y}{\sinh h}(1 - A) + rA\right]^2 \\ &+ \frac{\sinh y}{\sinh h}(1 - A)\left[\frac{\sinh y}{\sinh h}(1 - A) + A + r(y - h)A\right] \\ &+ B^2\left(r - \frac{\cosh y}{\sinh h}\right)^2 \\ &+ B^2\frac{\sinh y}{\sinh h}\left[\frac{\sinh y}{\sinh h} - r(y - h)\right]\Bigg\}\end{aligned} \tag{37}$$

where functions A and B are

$$(A, B) = \exp(-Z)(\cos Z, \sin Z)$$

Similar treatment can be done for the bottom boundary layer and we obtain $\overline{v} = 0$ and

$$\overline{u} = \frac{\varepsilon}{2\sinh^2 h}\left[1 - 2\exp(-Y)\cos Y + \exp(-2Y)\right] \quad (38)$$

Now, the complete formula for the streaming velocity applicable to all the regions including the two boundary layers is $\overline{v} = 0$ and

$$\begin{aligned}\overline{u} = \frac{\varepsilon}{2}\Bigg\{&\left[\frac{\cosh y}{\sinh h}(1-A) + rA\right]^2 \\ &+ \frac{\sinh y}{\sinh h}(1-A)\left[\frac{\sinh y}{\sinh h}(1-A) + A + r(y-h)A\right] \\ &+ B^2\left(r - \frac{\cosh y}{\sinh h}\right)^2 \\ &+ B^2\frac{\sinh y}{\sinh h}\left[\frac{\sinh y}{\sinh h} - r(y-h)\right] \\ &+ \frac{1}{\sinh^2 h}\left[\exp(-2Y) - 2\exp(-Y)\cos Y\right] - r^2\frac{y}{h}\Bigg\}\end{aligned} \quad (39)$$

As a typical example, for the case with $\lambda = 100\,\mu\text{m}$ and $h^* = 50\,\mu\text{m}$, we have $h = \pi$, and for $\varepsilon = 3.8 \times 10^{-4}$ and $\text{Re} = 4760$ we evaluate $\overline{u} = 3.8 \times 10^{-4}$ as the approximately maximum streaming velocity obtained from the bulk-flow solution (Eq. (36)) at $y = h$. When the velocity scale is $A_0\omega = 113\,\mu\text{m}$, this becomes $\overline{u}^* = 43\,\mu\text{m/s}$. This is not much different from the measured velocity (less than $100\,\mu\text{m/s}$) reported by Nguyen et al. [2], considering that the numerical result $1000\,\mu\text{m/s}$ obtained by them is more than 10 times the measured value for the same parameter set.

Figure 6 shows distributions of the streaming velocity for three depths of the fluid layer with the parameter set presented previously. The magnitude of streaming velocity increases on the whole as the depth decreases. Further decrease of h results in the overlap of the top and bottom boundary layers, and so the analytical solutions presented so far may not hold in that case.

The flow rate through the channel is given by

$$q = \int_0^h \overline{u}\,\text{d}y$$

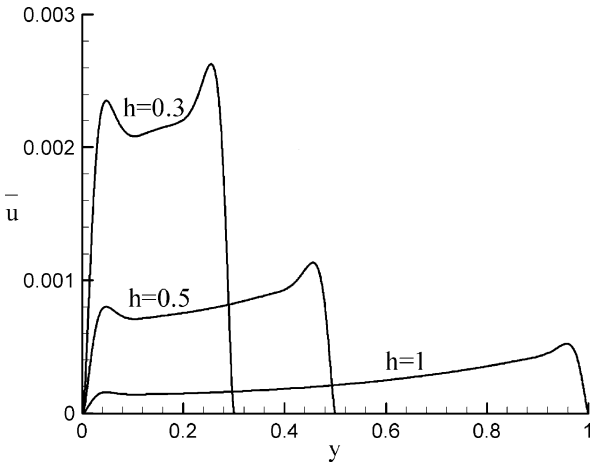

Acoustic Streaming, Figure 6 Distributions of the Stokes drift velocity across the fluid layer for three channel depths given by the flexural plate wave

Substituting the streaming velocity distribution (Eq. (39)) into this yields the following formula.

$$q = \frac{\varepsilon}{2\sinh^2 h}\left[\sinh h\cosh h - \sqrt{2/\text{Re}}\left(1 + \frac{7}{8}\sinh^2 h\right)\right] \quad (40)$$

At high Reynolds numbers, the second term within [ ] on the right-hand side of the above equation can be neglected and so the flow rate increases as the channel depth decreases, in line with the numerical result of Nguyen et al. [2]. On the other hand, when the second term is considered the flow rate shows a maximum value at a critical depth. Figure 7 shows the dependence of the flow rate on the depth at three Reynolds numbers and at the other parameter values the same as those presented previously. It indeed shows that at each of the critical depths, the flow rate has a maximum value. The critical depth increases as the Reynolds number decreases. It can be shown that the critical depth is given by the formula

$$h_c = \sinh^{-1}\left(\sqrt{\frac{8}{\text{Re} - 8}}\right) \quad (41)$$

For instance, at $\text{Re} = 4760$ we obtain $h_c = 0.041$ which corresponds to $h_c^* = 0.65\,\mu\text{m}$ at $\lambda = 100\,\mu\text{m}$. This is very small compared with the wavelength, but it is still far larger than the amplitude of the oscillation of the plate, $A_0 = 6\,\text{nm}$.

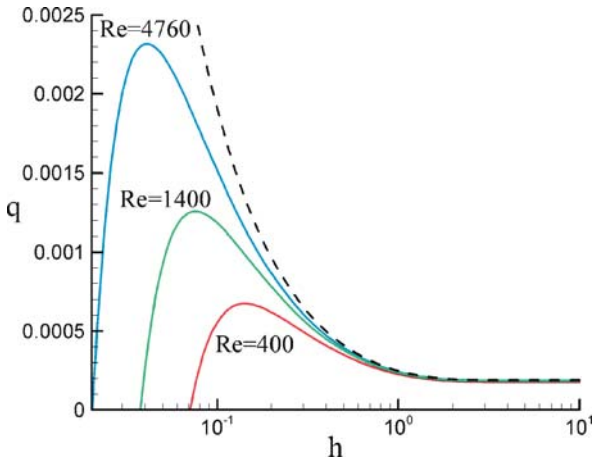

Acoustic Streaming, Figure 7 Effect of the channel depth on the flow rate at three Reynolds numbers for the flexural-plate-wave pumping. Dashed line corresponds to Re $= \infty$

Key Research Findings

Acoustic streaming has been applied to various microfluidic areas. White's group [2] have developed micropumps that utilize the flexural plate wave as the actuator. They have conducted a numerical simulation but the deviation was significant; their simulation results had to be corrected by a factor of 7 in order to fit the measurement data. To date, no report has been given of a satisfactory agreement between the experimental measurements and numerical or theoretical predictions. The numerical computation for acoustic streaming is not as simple as it looks. There are two key factors which may degrade the numerical results: one arises from the thin Stokes layer and the other from the extremely low levels of the streaming velocity compared with the primary flow. These can be overcome when we put very fine grids near the Stokes layer and simultaneously use high-precision numerical values.

In order to apply acoustic streaming to fluid mixing, Yaralioglu et al. [7] designed patterns of piezoelectric transducers on the bottom wall of a microchannel. They verified experimentally that the transducers, by generating acoustic streaming inside the channel normal to the main flow, enhanced the mixing. The mixing effect was, of course, affected by the configuration of the electrode patterning. They also asserted that the fundamental problem of the formation of bubbles and unintended heating of the fluid was not expected to occur in their system.

Acoustic streaming has also been applied to electrochemistry. Compton's group [8] has tested the use of ultrasound to study the effect of the various configurations of the acoustic streaming on the limiting current from an electrode. It was shown that there was a critical diffusion layer thickness below which the layer no longer became thinner. Recently they performed a numerical simulation on the acoustic streaming over an electrode within an axisymmetric space. The streaming flow was generated by the Reynolds stress terms formulated by other investigators. They successfully verified the previous experimental results that acoustic streaming was the principle mechanism of enhanced mass transport in sono-electrochemical cells.

Ultrasonics and its universal effect (acoustic streaming) have been used to manipulate particles in microfluidic devices, e. g., trapping, collection, separation, and deposition. For instance, Petersson et al. [9] employed a microchannel system with one center and two side channels at the inlet and outlet, respectively, of the channel. Through the side inlet channels they put a medium, say fluid *A*, containing particles, and through the center inlet channel the fluid *B* containing no particles. They then applied ultrasound normal to the channel in such a way that a standing wave was established in the main channel where the two media contacted each other. Due to the Reynolds stress and recirculating streaming flows, particles were collected near the channel center and this pattern persisted all the way through the main channel. At the outlet, the particles flow with the fluid *B*. They implied that such a medium-exchange effect could be applied to blood washing.

Marmottant and Hilgenfeldt [10] have considered bubble-driven microfluidic transport for bioengineering applications. In their experiment, bubbles were adsorbed on the bottom wall of the microchannel. When the standing ultrasound wave was introduced within the channel, steady streaming flow was generated. They stressed that the flow pattern in bubble streaming was quite different from that induced by an oscillating solid object. More interestingly, close contact of a foreign solid particle to the bubble showed a significant effect in the overall steady-flow field due to superposition of the bubble and particle streaming fields.

Future Directions for Research

To date no numerical simulation of the acoustic streaming flow associated with application to the microfluidics has been successfully performed. The simulation can be performed only with the streaming flow by using the governing equation given as Eq. (27), but we also need to solve the full unsteady Navier–Stokes equations including not only the primary oscillatory flow component but also the secondary steady flow component. In this case locally fine grids must be adopted to deal with the thin Stokes layer adjacent to the solid surface.

We also need to analyze the case for the flexural-plate-wave flow in more detail and to simultaneously perform numerical simulations of the resultant flows. The results of the full numerical simulation may be used to prove that the steady flow components are generated by the mechanism known as the Stokes drift flow.
We also need to study the dissipation effect caused by the oscillatory flow. At present, in Lab-on-a-Chip design, we are usually interested in the feasibility of the functions provided by the transducers, but sooner or later the energy consumption may be one of the most important factors.

Cross References

- ► Acoustic-Based Biosensors
- ► Piezoelectric Microdispenser
- ► Transport of Droplets by Acoustics
- ► Ultrasonic Pump

References

1. Riley N (2001) Steady streaming. Ann Rev Fluid Mech 33:43–65
2. Nguyen NT, Meng AH, Black J, White RM (2000) Integrated flow sensor for in situ measurement and control of acoustic streaming in flexural plate wave micropumps. Sens Actuators A 79:115–121
3. Lighthill J (1978) Waves in Fluids. Cambridge University Press, Cambridge
4. Iskandarani M, Liu PLF (1991) Mass transport in three-dimensional water waves. J Fluid Mech 231:417–437
5. Schlichting H, Gersten K (2003) Boundary Layer Theory. Springer, Berlin
6. Frampton KD, Martin SE, Minor K (2003) The scaling of acoustic streaming for application in micro-fluidic devices. Appl Acoust 64:681–692
7. Yaralioglu GG, Wygant IO, Marentis TC, Khuri-Yakub BT (2004) Ultrasonic mixing in microfluidic channels using integrated transducers. Anal Chem 76:3694–3698
8. Marken F, Akkermans RP, Compton RG (1996) Voltammetry in the presence of ultrasound: the limit of acoustic streaming induced diffusion layer thinning and the effect of solvent viscosity. J Electroanal Chem 415:55–63
9. Petersson F, Nilsson A, Jonsson H, Laurell T (2005) Carrier medium exchange through ultrasonic particles switching in microfluidic channels. Anal Chem 77:1216–1221
10. Marmottant P, Hilgenfeldt S (2004) A bubble-driven microfluidic transport element for bioengineering. Proc Nat Acad Sci 101(26):9523–9527

Acoustic Streaming Pumps

- ► Ultrasonic Pumps

Acoustic Waves

- ► Acoustics Based Biosensors

AC Pumping of Liquids

- ► AC Electro-Osmotic Flow

Active Mixer

CHIH-CHANG CHANG[1], LUNG-MING FU[2], RUEY-JEN YANG[1]
[1] Department of Engineering Science, National Cheng Kung University, Tainan, Taiwan
[2] Department of Materials Engineering, National Pingtun University of Science and Technology, Pingtun, Taiwan
rjyang@mail.ncku.edu.tw

Synonyms

Dynamic mixing; Active mixing

Definition

The term "active mixer" or "active micromixer" refers to a microfluidic device in which species mixing is enhanced by the application of some form of external energy disturbance. Typically, this disturbance is generated either by moving components within the micromixer itself, e. g. magnetically-actuated stirrers, or by the application of an external force field, e. g. pressure, ultrasound, acoustic, electrohydrodynamic, electrokinetic, dielectrophoretic, magneto-hydrodynamic, thermal, and so forth [1].

Overview

Mixing occurs in many natural phenomena, including geophysical, ocean and atmospheric flows, and is also an important step in industrial processes involving chemical reactions, fermentation reactions, combustion, and so forth. Traditionally, industrial mixing applications have always been performed using large-scale apparatus. However, in recent years, micro-scale devices (commonly referred to as microfluidic devices) have been proposed as a means of constructing micro-total analysis systems (μ-TAS) and Lab-on-a-Chip (LOC) devices. However, achieving a rapid and efficient mixing of different reactants when performing chemical and biological analyzes in such microfluidic devices is highly challenging. Therefore, the problem of developing enhanced micromixing schemes suitable for microfluidic applications has attracted significant interest within industrial and academic circles in recent years. As a result, the literature now

contains a large number of studies concerning micromixers implemented using a variety of mixing strategies [1].

The characteristic size of the microchannels in microfluidic devices is very small (typically of the order of several hundred micrometers), and hence the flow is dominated by viscous forces. As a result, the flow is restricted to the low Reynolds number regime, and thus turbulence does not occur. The Reynolds number of microfluidic flows in a conventional straight microchannel is typically less than unity, and the resulting Stokes flow is unidirectional. Even in curved or twisted microchannels, the transverse component of the flow (i. e. the secondary flow) is very small compared to the streamwise component since the inertial effects induced by the microchannel geometry are very weak. Therefore, when the microchannels contain two or more fluid streams, mixing of the different streams is dominated by molecular diffusion effects. In microscale channels, the diffusive mixing process is very slow compared with the rate at which the fluid is convected along the channel. Typically, microfluidic flows have a high Péclet number, i. e. $\mathrm{Pe} = Ul/D$, where U is the average flow velocity, l is the channel dimension and D is the molecular diffusivity. The diffusive mixing time is given by $t_\mathrm{D} \sim l^2/D$ and the mixing channel length required to achieve an adequate species mixing increases linearly with the Péclet number ($L_\mathrm{m} \sim \mathrm{Pe} \times l$). For example, for an average flow velocity of 500 μm/s, a channel dimension of 100 μm and a molecular diffusivity of 10 $\mu\mathrm{m}^2$/s, the mixing time and length required to achieve a complete species mixing are of the order of 1000 sec and 0.5 m, respectively. However, many practical biochemical applications, e. g. immunoassays and DNA hybridization, require the rapid mixing of macromolecules characterized by relatively low molecular diffusivity. Therefore, the mixing performance obtained in typical microchannels is unsuitable for biochemical analysis applications. Accordingly, a requirement exists for enhanced microfluidic mixing schemes to support the development of μ-TAS and LOC devices. Typically, such schemes involve reducing the diffusion length (i. e. l) and the diffusion time by increasing the interfacial contact area between the mixing species.

Although it is difficult to induce turbulence (so-called Eulerian chaos) in microchannels, the mixing performance obtained in low Reynolds number flow regimes can be enhanced via the chaotic advection mechanism (or so-called Lagrangian chaos). Chaotic advection occurs in regular, "smooth" (from a Eulerian viewpoint) flows [2] and provides an effective increase in both the interfacial contact area and the concentration gradient by inducing a reduction in the striation thickness, and hence in the diffusion length. As a result, both the mixing time and the mixing length are considerably reduced. In the case of a linear reduction in the striation thickness within the flow path, the mixing time and mixing length exhibit a sub-linear dependence on Pe. The two parameters can be reduced to as much as $t_\mathrm{m} \sim \ln(\mathrm{Pe})$ and $L_\mathrm{m} \sim \ln(\mathrm{Pe})$, respectively, for chaotic flows in the limit of large Pe [2, 3]. Importantly, chaotic advection cannot occur in steady, two-dimensional flows, but is restricted to time-dependent two-dimensional and three-dimensional flows. Accordingly, a small cylindrical rotor spinning about its centre with a uniform angular frequency (i. e. Couette flow) fails to provide an efficient micromixing performance, whereas two such rotors turned on and off alternatively create a blinking vortex phenomenon which yields a powerful mixing effect [2]. In Couette flow, the fluid streams are only stretched. Hence, chaotic advection cannot be induced, and thus the mixing effect is very poor. However, in the two-rotor arrangement, the fluid streams are repeatedly stretched around one rotor and then folded around the other. As a result, chaotic advection is induced and a good mixing performance is obtained. In general, achieving an effective mixing of two or more fluid streams always requires a repeated stretching and folding of the fluid elements. In recent years, various active mixing approaches have been proposed using chaotic advection to enhance the mixing effect. The chaotic flows induced by such active approaches are time-dependent and are easily controlled using external mechanisms. As such, active mixers are eminently suitable components for reconfigurable microfluidic systems.

Basic Methodology

Flow Field

Applying the continuum assumption, microfluidic flows can be modeled by the continuity equation and by a momentum equation modified to include the body force term, i. e.

$$\nabla \cdot \boldsymbol{u} = 0 \tag{1}$$

and

$$\rho_f \left(\frac{\partial \boldsymbol{u}}{\partial t} + \boldsymbol{u} \cdot \nabla \boldsymbol{u} \right) = -\nabla p + \mu \nabla^2 \boldsymbol{u} + \boldsymbol{F} \quad , \tag{2}$$

where t, $\boldsymbol{u}$, p, ρ_f and μ denote the time, the fluid velocity, the pressure, the fluid density and the fluid viscosity, respectively. In Eq. (2), $\boldsymbol{F}$ represents the external driving force (i. e. the external energy source) associated with the specific active micromixer. For example, in an electrohydrodynamic/electrokinetic-based active mixer, $\boldsymbol{F}$ represents the Coulombic force produced by the presence of a free space charge, $\rho_e E$, where ρ_e is the net free charge

density in the bulk liquid or at the solid-liquid interface (i. e. the electrical double layer) and $\boldsymbol{E}$ is the intensity of the externally applied DC or AC electrical field. Meanwhile, for a magneto-hydrodynamic mixer, $\boldsymbol{F}$ is the Lorentz force induced by the coupling between the magnetic field $\boldsymbol{B}$ and the electrical field $\boldsymbol{E}$, ($\boldsymbol{J}\times\boldsymbol{B}$, where $\boldsymbol{J}$ is the current density). In the literature, Eqs. (1) and (2) are generally solved using well-known numerical methods such as the finite difference method (FDM), the finite volume method (FVM), the finite element method (FEM), and so forth.

In typical microfluidic applications, the Reynolds number is much lower than unity (i. e. $\mathrm{Re} = \rho_f Ul/\mu \ll 1$), and hence the flow can be approximated as a creeping flow (i. e. Stokes flow). Therefore, the convection term in Eq. (2) can be neglected, and the time-dependent flows in active micromixers are then governed by Eq. (1) and Eq. (3), i. e.

$$\rho_{\mathrm{f}}\frac{\partial \boldsymbol{u}}{\partial t} = -\nabla p + \mu\nabla^2\boldsymbol{u} + \boldsymbol{F}. \tag{3}$$

Additionally, provided that the time required to reach the viscous diffusion time scale is much less than the oscillation time scale (ω^{-1}), i. e. $\rho_{\mathrm{f}}\omega l^2/\mu \ll 1$, the time derivative term in Eq.(3) can be neglected, and therefore the unsteady flow fields in active micromixers can be regarded as quasi-steady Stokes flow described by Eqs. (1) and (4), i. e.

$$0 = -\nabla p + \mu\nabla^2\boldsymbol{u} + \boldsymbol{F} \quad . \tag{4}$$

Visualization of Mixing Process

Numerical studies relating to active micromixers generally visualize the mixing process and evaluate the mixing performance by solving the following convection-diffusion equation:

$$\frac{\partial C}{\partial t} + \boldsymbol{u}\cdot\nabla C = D\nabla^2 C \tag{5}$$

in which C and D represent the sample concentration and the diffusion coefficient, respectively. However, there are several drawbacks to this approach. For example, if the deformation of the species interface is complex and the mixing channel is very long, the equation solution may fail to identify the interface precisely due to numerical diffusion and natural species diffusion. Furthermore, in large Péclet number flows, convective transport dominates the diffusive mechanism and the sample dispersion in the flow field can be greatly enhanced by promoting the convective transport. In such diffusion-limited cases, the diffusion effects can be neglected, and the sample simply convects with the fluid along the local instantaneous streamlines. Under these conditions, the Lagrangian particle tracing technique, which introduces mass-less, non-interacting passive particles into the flow fields, provides a satisfactory means of observing the advection phenomenon within the fluid streams without solving Eq. (5). The motion of a tracer particle can be tracked by the following kinematic equation (dynamic system):

$$\frac{\mathrm{d}\boldsymbol{r}}{\mathrm{d}t} = \boldsymbol{u}\,(\boldsymbol{r}, t)\,, \tag{6}$$

where $\boldsymbol{r}$ is the location of the tracer particle and $\boldsymbol{u}\,(\boldsymbol{r}, t)$ is the Eulerian velocity field. The tracer particle position in the unsteady flow field at different times can be obtained simply by integrating Eq. (6). Many suitable integration methods are presented in the literature, ranging from the simple first-order Euler method to the fourth-order Runge–Kutta method, or even higher-order methods. Besides simulating the dispersion of a blob of samples, the particle tracing method also enables the stretching and folding of fluid elements in an unsteady flow field to be clearly observed.

Characterization of Chaotic Mixing

In order to optimize the fluid deformation phenomena in active micromixers during the mixing process, it is first necessary to understand the fluid stretching and folding mechanisms which take place, and to evaluate them in a quantitative manner. Over the past few decades, dynamic system analysis techniques such as Poincaré maps and Lyapunov exponents have revealed that the repeated stretching and folding of fluid elements results in a chaotic mixing effect. (Interested readers are referred to the text edited by Ottino [2] for details regarding the application of Poincaré maps and Lyapunov exponents to the exploration of mixing kinematics). The information provided by Poincaré maps and Lyapunov exponent analysis enables a thorough understanding of the characteristics of micro-active mixing systems. Specifically, Poincaré maps can be used to explain the transitions of the mixing system behavior from periodic or quasi-periodic to chaotic motion, while the Lyapunov exponents provide an indication of the strength of the chaotic behavior and can be used to quantify the effects of the amplitude and frequency of the perturbations on the chaotic response. Collectively, the data provided by Poincaré maps and Lyapunov exponents provide sufficient information to optimize the design and operation of micro-active mixing devices.

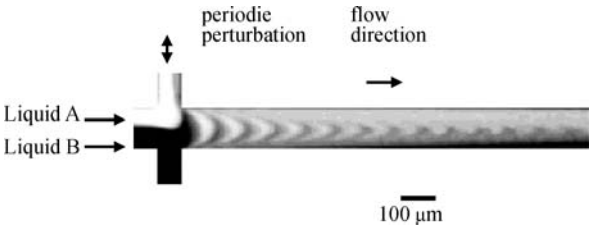

Active Mixer, Figure 1 Pressure perturbations induce lobe-like distortions of the interface and facilitate rapid mixing in the device with one pair of side channel

Key Research Findings

Many active mixing approaches have been proposed in recent years. Broadly speaking these approaches can be classified in terms of whether or not they use moving parts to generate a mixing effect. In those micromixers which do use moving parts, mixing is commonly achieved using micro stirrer bars, piezoelectric membranes, gas bubbles, and so forth. However, since the integration of these moving parts within the overall microfluidic system is challenging, and therefore expensive, researchers have paid increasing attention to active micromixers containing no moving elements. Numerous proposals for active mixing approaches have been presented in recent years, and space constraints prevent their detailed discussion here. Hence, the following provides no more than a high-level review of some of the more fundamental techniques. For a comprehensive discussion of active mixing schemes, interested readers are directed to the review presented by Nguyen and Wu in [1].

Pressure Perturbation Mixer

In pressure perturbation mixers, the species are perturbed by pulsing their velocities in some way. For example, Niu and Lee [4] presented an active mixer comprising a main channel and multiple side channels, in which the mixing species were stirred by pulsing the velocities of the fluids introduced through the side channels, as shown in Fig. 1. The resulting stretching and folding of the fluid elements in the main and side channels induced a chaotic advection mixing effect. A detailed particle simulation study was performed to examine the respective effects of the amplitude and frequency of the flow perturbations on the species mixing performance. Poincaré maps, constructed using the simulation data, showed that for a given parameter set, the fluid flow exhibited both chaotic and quasi-periodic responses. Additionally, Lyapunov exponent data were applied as mixing indices to evaluate the intensity of the chaotic mixing effect. The optimal operating parameters were then determined by plotting the Lyapunov exponent data against the amplitude and frequency of the perturbation.

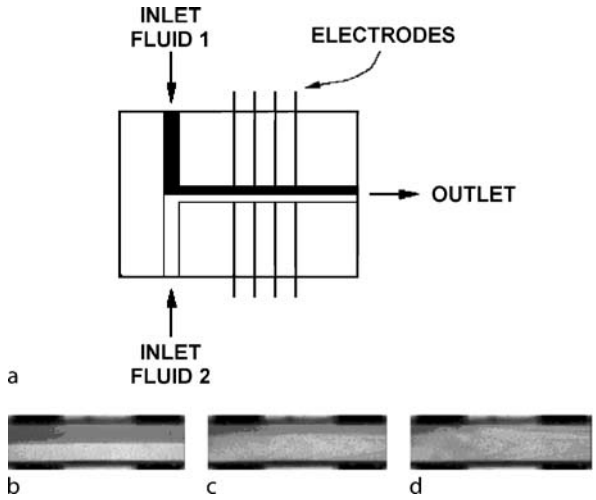

Active Mixer, Figure 2 (**a**) Configuration of electrohydrodynamic mixer. Experimental images of mixing (**b**) initial condition, (**c**) after the application of a DC electric field of intensity $E = 4 \times 10^5\ V/m$ and (**d**) $E = 6 \times 10^5$ V/m

Electrohydrodynamic (EHD) Mixer

In electrohydrodynamic (EDH) mixers, a mixing effect is created by applying an external electrical field to a bulk flow containing both an electrical conductivity gradient and a permittivity gradient. In the micromixer proposed by Moctar et al. [5], two fluids with identical viscosity and density but different electrical properties were injected into the mixing channel by syringe pumps, and the electrodes were arranged in such a way that the electrical field was perpendicular to the species interface, as shown in Fig. 2(a), creating a transversal secondary flow. The mixing effects induced by both DC and AC electrical fields were explored in a series of experimental investigations. From Fig. 2(b), (c) and (d), it can be seen that the mixing becomes more chaotic as the intensity of DC electric field increases. The results revealed that the application of an appropriate voltage and frequency to the electrodes, yielded a satisfactory mixing performance within less than 0.1 sec over a short mixing distance, even at Reynolds numbers as low as 0.02.

Electrokinetic-Based Mixer

Oddy et al. [6] presented a micromixer in which AC electrical fields were used to induce the electrokinetic instability (EKI) phenomenon in microscale channels at very low Reynolds numbers, as shown in Fig. 3. EKI is similar

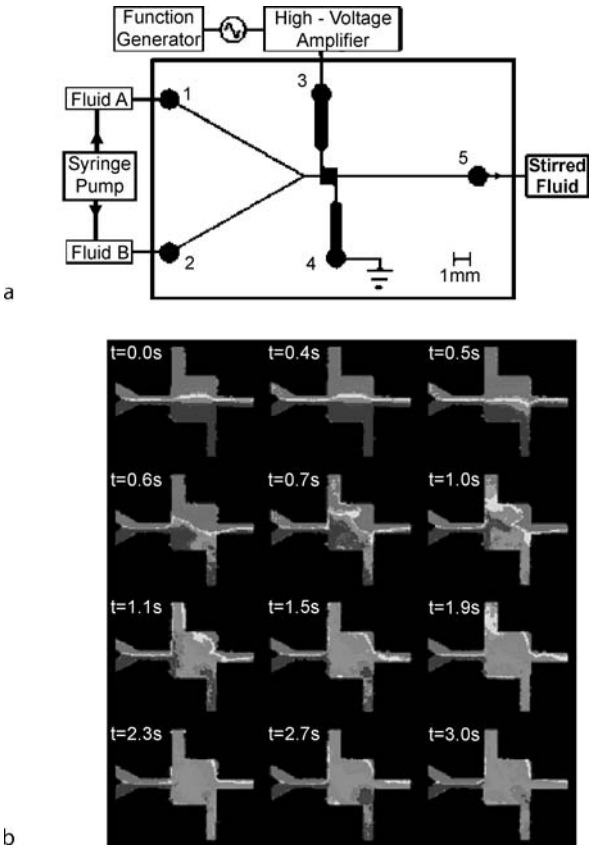

Active Mixer, Figure 3 (**a**) Configuration of electrokinetic instability mixer and (**b**) time-stamped experimental images of mixing process

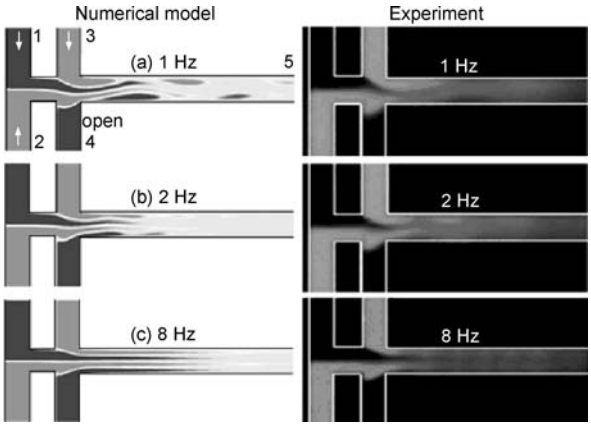

Active Mixer, Figure 4 Numerical and experimental images of mixing for different switching frequencies for a constant driving electric field of 100 V/cm

to electrohydrodynamic instability, which can be induced by either AC or DC electrical fields when an electrical conductivity gradient exists in the bulk flow. The results showed that for a flow rate of 0.5 μl/min, the EKI flow field resulted in a rapid stretching and folding of the fluid and achieved an effective mixing performance within 3 seconds, corresponding to less than 1% of the time required to achieve mixing via diffusion effects in a conventional straight microchannel.

Fu et al. [7] periodically switched an external electrical field to carry out species mixing in a T-form electrokinetic microfluidic mixer by generating electrokinetic perturbation forces. The authors showed that the mixing performance of the microfluidic mixer was enhanced by increasing the contact area and contact time of the mixing fluids, and by creating irregular flow fields in the mixing channel. However, the results also indicated that an adequate switching frequency was required to achieve a satisfactory mixing performance, as shown in Fig. 4.

Qian and Bau [8] applied time-wise periodic alterations of the zeta potential along the microchannel walls to induce an electroosmotic chaotic advection effect. It was shown that both a spatial and a temporal control of the zeta potential could be achieved by applying a field effect (i. e. a capacitive effect). The effect of periodically switching between several different flow fields at various periods was analyzed by performing particle tracking simulations (i. e. Poincaré maps). The results indicated that a more chaotic mixing effect was achieved at lower values of the switching frequency.

Magneto-Hydrodynamic (MHD) Mixer

Various researchers have employed the magneto-hydrodynamic (MHD) effect to implement micromixers. For example, Bau et al. [9] developed an active micromixer which used either DC or AC electrical and magnetic fields to generate Lorentz forces with which to stretch and fold the species fluids in a mixing chamber. The results indicated that an adequate mixing result was achieved within several seconds. A more sophisticated MHD mixer was developed by Yi et al. [10] based upon the two blinking-vortex arrangement used to induce chaotic advection. The proposed micromixer comprised a small cylindrical mixing chamber with an electrode deposited on its side wall and two copper-wire electrodes positioned eccentrically on the lower surface of the chamber. The chamber was orientated such that its axis was parallel to the direction of an applied magnetic field, and a mixing effect was generated by applying a potential difference of period T alternately between one of the wire electrodes and the circular side-wall electrode and between the second wire electrode and the side-wall electrode, as shown in Fig. 5. The particle tracing results revealed that the intensity of the chaotic mixing effect increased with increasing

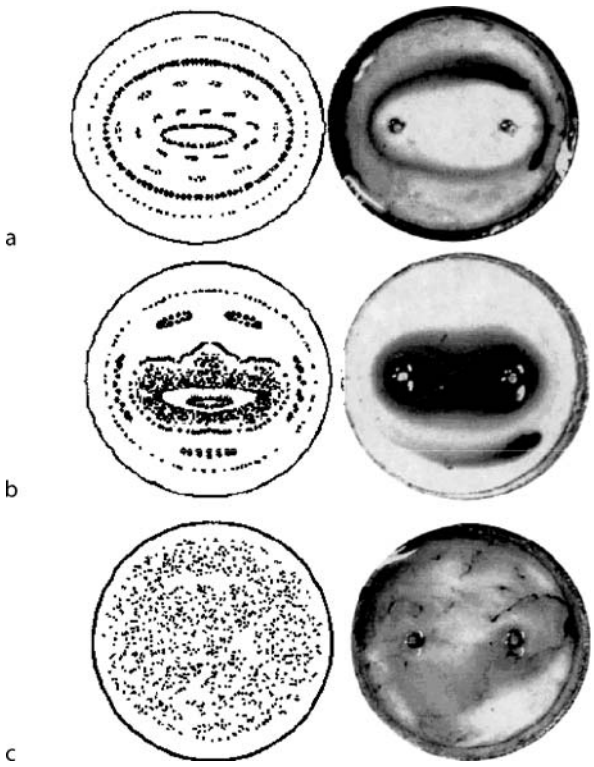

Active Mixer, Figure 5 Poincare maps (left column) and flow visualization photographs (co-rotating). For different periods of (**a**) $T = 4$, (**b**) $T = 10$ and (**c**) $T = 40$

T, resulting in a satisfactory mixing result within 40 periods.

Future Directions for Research

It seems likely that future micromixer designs will continue the current trend for implementing species mixing without the use of moving mechanical parts. Furthermore, it seems reasonable to speculate that the use of electrokinetic forces to induce a mixing effect will become increasingly common since this technique greatly simplifies the microfabrication process and reduces the cost and complexity involved in embedding active mixers within microfluidic systems. Electrokinetic forces have been widely employed in active mixing schemes in recent years, a case in point being the EKI mixer presented by Oddy et al. in [6]. However, current EKI-based mixers suffer the drawback of a high electrical voltage requirement. Accordingly, low-voltage, AC electrokinetic techniques are expected to receive increasing attention in coming years. Finally, it is known that the high flow rates required to achieve species mixing can be produced through various nonlinear electrokinetic phenomena. Therefore, the application of nonlinear electrokinetic techniques to realize active mixers is likely to emerge as a major research topic in the microfluidics community in the near future.

Cross References

- ► AC Electro-Osmotic Flow
- ► Chaotic Flow
- ► Electroosmotic Flow (DC)
- ► Electrokinetic/Hydrodynamic Flow Instability
- ► Microfluidic Mixing

References

1. Nguyen NT and Wu Z (2005) Micromixers – a review. J Micromech Microeng 15:R1–16
2. Ottino JM (1989) The Kinematics of Mixing: Stretching, Chaos, and Transport. Cambridge University Press, Cambridge
3. Stroock AD, Dertinger SKW, Ajdari A, Mezic I, Stone HA, Whitesides GM (2002) Chaotic mixer for microchannels. Science 295:647–651
4. Niu X, Lee YK (2003) Efficient spatial-temporal chaotic mixing in microchannels. J Micromech Microeng 13:454–62
5. El Moctar AO, Aubry N, Batton J (2003) Electro-hydrodynamic micro-fluidic mixer. Lab Chip 3:273–280
6. Oddy MH, Santiago JG, Mikkelsen JC (2001) Electrokinetic instability micromixing Anal Chem 73:5822–5832
7. Fu LM, Yang RJ, Lin CH, Chien YS (2005) A novel microfluidic mixer utilizing electrokinetic driving forces under low switching frequency. Electrophoresis 26:1814–1824
8. Qian S and Bau HH (2002) A chaotic electroosmotic stirrer Anal Chem 74:3616–3625
9. Bau HH, Zhong J, Yi M (2001) A minute magneto hydro dynamic (MHD) mixer. Sens Actuators B 79:207–215
10. Yi M, Qian S, Bau HH (2002) A minute magneto hydro dynamic (MHD) chaotic stirrer. J Fluid Mech 468:153–177

Active Mixing

- ► Active Mixer

Active Particle Flows

- ► Simulating Migration of Polymer Chains, Methods

Advanced Silicon Etching (ASE)

- ► ICP Etching
- ► Plasma Etching

AFM

Definition

The *atomic force microscope* (AFM) is a very high-resolution type of scanning probe microscope, with demonstrated resolution of fractions of an Angstrom, more than a 1000 times better than the optical diffraction limit. The AFM is one of the foremost tools for imaging, measuring and manipulating matter at the nanoscale. The AFM consists of a microscale cantilever with a sharp tip (probe) at its end that is used to scan the specimen surface. When the tip is brought into proximity of a sample surface, forces between the tip and the sample lead to a deflection of the cantilever according to Hooke's law. Depending on the situation, forces that are measured in AFM include mechanical contact force, Van der Waals forces, capillary forces, chemical bonding, electrostatic forces, magnetic forces, etc. Typically, the deflection is measured using a laser spot reflected from the top of the cantilever into an array of photodiodes. Other methods that are used include optical interferometry, capacitive sensing or piezoresistive AFM probes.

Cross References

- ► Atomic Force Microscope (AFM)
- ► Biosensor
- ► Biosensors Using Atomic Force Microscopes
- ► Scanning Probe Microscope

AFM Biosensors

- ► Biosensors Using Atomic Force Microscopes

Aggregation of Nanoparticles

- ► Nano-Particle Controllable Assembly

Aging

Definition

Aging is known in material science as material fatigue. It is a permanent structural damage that occurs when a material is subjected to cyclic or fluctuating strains at nominal stresses that have maximum values less than (often much less than) the static yield strength of the material. These damages can although be effected by thermal stresses due to continuous heating and cooling.

AlN

- ► Piezoelectric Materials for Microfluidics

Amperometric Detection

- ► Amperometric Techniques
- ► Electrochemical Techniques

Amperometric Techniques

THOMAS J. ROUSSEL[1,3], DOUGLAS J. JACKSON[2], RICHARD P. BALDWIN[3], ROBERT S. KEYNTON[1]
[1] Department of Bioengineering, University of Louisville, Louisville, KY, USA
[2] Department of Electrical and Computer Engineering, University of Louisville, Louisville, KY, USA
[3] Department of Chemistry, University of Louisville, Louisville, KY, USA
thomas.roussel@louisville.edu, doug.jackson@louisville.edu, rick.baldwin@louisville.edu, rob.keynton@louisville.edu

Synonyms

Amperometric detection; Controlled-potential instrumentation; Electrochemical detection; Oxidation/reduction

Definition

Amperometry is one of a family of electrochemical methods in which the potential applied to a sensing electrode is controlled instrumentally and the current occurring as a consequence of oxidation/reduction at the electrode surface is recorded as the analytical signal. In its simplest form, the applied potential is stepped to and then held at a constant value; and resulting current is measured as a function of time. When *amperometric detection* is used in conjunction with separation techniques such as capillary electrophoresis or liquid chromatography, the sensing (or "working") electrode is placed at the end of the separation stream so as to permit detection of sample components as they emerge and pass over the electrode surface. The applied potential must be sufficient to cause facile oxidation or reduction of the target analytes; and, in general, the magnitude of the measured current is directly proportional to the analyte concentration.

Overview

Amperometric electrochemical (EC) detection was initially developed in the 1970s for conventional sized high performance liquid chromatography (HPLC) instrumentation [1]. However, as the principal micro/nanofluidic applications of the approach are most directly related to capillary electrophoresis (CE), it is the development of these latter systems that is of greatest relevance here. Amperometric detection was first introduced in conventional bench-scale CE in 1987 by Wallingford and Ewing [2] for the determination of catecholamine-based neurotransmitters. The detection was carried out by carefully placing a small carbon fiber electrode at the outlet of the separation capillary and recording the current transient caused by oxidation of each catecholamine as it emerged from the capillary outlet and passed over the fiber. Subsequently, dozens of papers have appeared both on novel instrument designs in CE/EC and on a wide range of CE/EC applications [3]. During the course of this work, amperometric CE/EC has been carried out on a variety of carbon and metallic electrodes and has been shown to offer both the high sensitivity (μM–nM) required by CE and a unique selectivity determined by the potential applied and the specific electrode used. In general, this detection approach is applicable to several important families of organics. In addition to catechols, these include carbohydrates, amino acids, thiols, phenols, and aromatic amines, as well as a variety of specific compounds of biological or pharmaceutical interest.

In amperometry, quantification of species concentration is possible because the magnitude of the current generated in any given experiment is determined by the number of molecules, of that species, oxidized or reduced at the surface of the sensing electrode and therefore is directly proportional to the concentration of the molecule detected as defined by Faraday's law (Eq. (1)).

$$i_t = \frac{\mathrm{d}Q}{\mathrm{d}t} = \eta F \frac{\mathrm{dN}}{\mathrm{d}t} \tag{1}$$

Where i_t is the current generated at the surface of the sensing electrode at time $= t$, Q is the charge at the surface of the sensing electrode, η is the number of moles of electrons transferred per mole of analyte, N is the number of moles of analyte oxidized or reduced, and F is the Faraday constant ($96{,}487\ \mathrm{C\,mol^{-1}}$). Detection limits have been reported at the attomole and femtomole levels [4, 5], roughly corresponding to micromolar concentrations in the carrier fluid. Because this form of detection is coupled to the liberation or consumption of electrons, the application of this detection technique is limited to those species that are electroactive, i. e., those that can be oxidized or reduced at an electrode surface. While amperometry has been used for decades in benchtop scale analytical systems, the greatest attractiveness of this particular detection approach lies with the ability to miniaturize the necessary electrodes (working, reference, and auxiliary or counter) and incorporate them into miniaturized *Lab-on-a-Chip* devices. The simplicity of the supporting electronics for amperometry provides advantages as well compared to other detection systems (e. g., UV-visible absorbance, laser-induced fluorescence, mass spectrometry, etc.) that require a considerably larger ensemble of supporting equipment.

The specific fluidic system involved, while not the main topic of this chapter, is closely linked to the detection system and warrants a brief explanation. Separation techniques such as CE and HPLC utilize channels or columns that pass a fluidic medium carrying the analytes of interest. Bulk flow is actuated using either gravity or pressure, in the case of LC, or electroosmotic forces, in the case of CE. Separation of analytes occurs due to physical or chemical interactions with what is incorporated into the column (a packing material that completely fills the column or is coated onto the inner walls) for HPLC or differential electrical migration of the charged analytes toward the electrokinetic "drive" electrodes for CE. Many of these separation techniques are being downsized using microfabrication methods, referred to collectively as *microfluidics*.

Basic Methodology

In a redox reaction (Eq. (2)), electrons are removed from a solution species (oxidation) at one electrode and transferred to a solute (reduction) at the other:

$$\begin{aligned} \alpha A &\rightarrow \chi C + ne^- && \text{(anode)} \\ \beta B + ne^- &\rightarrow \delta D && \text{(cathode)} \end{aligned} \tag{2}$$

where A, B, C, and D are the reactants and products of the reaction α, β, χ, and δ are their stoichiometric coefficients, and n is the number of electrons. To carry out and monitor such a reaction, an electrochemical *cell* is used. These *cells* typically consist of three electrodes – the working, auxiliary, and reference electrodes – placed in electrolyte solution. Amperometric sensing is controlled by application of the desired potential or voltage solely to the working electrode. This is the electrode at which the redox reaction (either oxidation or reduction) of the analyte of interest occurs, and therefore it is the current flowing at this electrode that constitutes the analytical signal (Fig. 1). The function of the reference electrode is to provide a contact

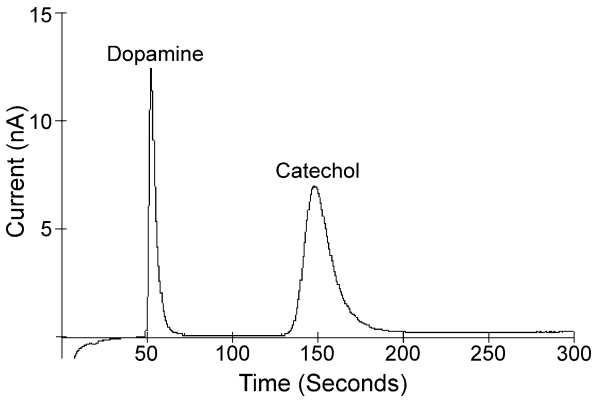

Amperometric Techniques, Figure 1 Typical electropherogram for catechol and dopamine using amperometric detection on a microchip platform

whose potential remains constant during the amperometry experiment, and its chemical composition (saturated calomel, Ag/AgCl, etc.) is purposely selected to facilitate this. The role of the counter electrode is to provide a current path that completes the electrical circuit. Thus, the redox reaction occurring here is equal in size but opposite in direction (i. e., reduction or oxidation). Normally, this electrode consists of a simple metallic contact, most commonly platinum.

The chemical composition/structure of the working electrode can vary considerably, and a proper selection is often critical to achieving success in a given application. The minimum requirements are reasonable degrees of chemical inertness and electrical conductivity. Commonly encountered electrodes include metals, such as Pt, Au, or Hg, and carbon. In addition, the surface of these electrode materials can also be modified chemically by a number of different approaches in order to optimize performance for a specific electrochemical process [6]. For example, the charge, polarity, porosity, and specific chemical and biochemical reactivity can be adjusted by the addition of appropriate functional groups, self-assembled mono- and bi-layers, and polymer coatings.

The function of the external electronic circuitry – or the "potentiostat" – in amperometric experiments is to supply the desired voltage difference between the working and reference electrodes and measure the resulting redox current instantaneously. The magnitude of the working electrode potential necessary to initiate the oxidation or reduction is ideally determined by the Nernst equation (shown in Eq. (3)) but can also be affected by factors such as the conductivity of the carrier fluid, the electron-transfer kinetics of the specific redox reaction, the composition of the detection electrode, and the relative distance between the working and reference electrodes.

$$E = E^0 - \frac{0.059}{|n|} \log\left(\frac{a_C^{\chi} a_D^{\delta}}{a_A^{\alpha} a_B^{\beta}}\right) \tag{3}$$

where E is the potential of the working electrode, E^0 is the standard potential for the redox reaction of interest, n is the number of electrons involved, and the a's represent the activities of the reactants and products. It follows from the Nernst equation that making the working electrode potential more negative favors the reduction process and is therefore said to be more "reducing" or "cathodic" while application of a more positive potential would be "oxidizing" or "anodic". Thus, in practice, amperometric detection involving analyte reduction is generally carried out by application of negative potentials, while analyte oxidation requires use of relatively positive applied potentials. Successful bench-scale CE/EC in the amperometric mode requires the accurate maintenance of EC potentials on the order of roughly ± 1 V at working electrodes placed in CE fields on the order of 5 – 30 kV and the measurement of EC currents typically pA in magnitude in the presence of μA-level background CE currents.

A representative three-electrode amperometric detection configuration and a simplified potentiostat circuit are shown in Fig. 1. The working and reference electrodes are placed in the amplifier feedback loops so that the voltage difference between them must match an adjustable external voltage source. Because the composition of the reference electrode is designed to maintain its potential at a constant value, the working electrode potential is just the selected external voltage compared to or "vs." the specific reference electrode used. The reference electrode is connected to a high input impedance buffer amplifier, which serves to limit the current flow through it to a negligible level, which in turn serves to keep its composition unchanged and its potential at its starting value. The working electrode is connected to an ammeter circuit, typically a sensitive transimpedance amplifier (current-to-voltage converter). The oxidation or reduction reaction occurring when an electroactive analyte passes the working electrode produces current flow in the ammeter that is then converted to a proportional voltage for display.

A simple electrical model of the solution as seen by the electrodes is shown in Fig. 3. Resistances are primarily determined by the ionic content of the electrolyte solution, which is typically in the 0.01 – 0.10 M range. When the electrodes are placed in an electrolyte solution, a charge separation or "double layer" forms spontaneously at the electrode-solution interface. This produces a capacitance, commonly referred to as the double-layer

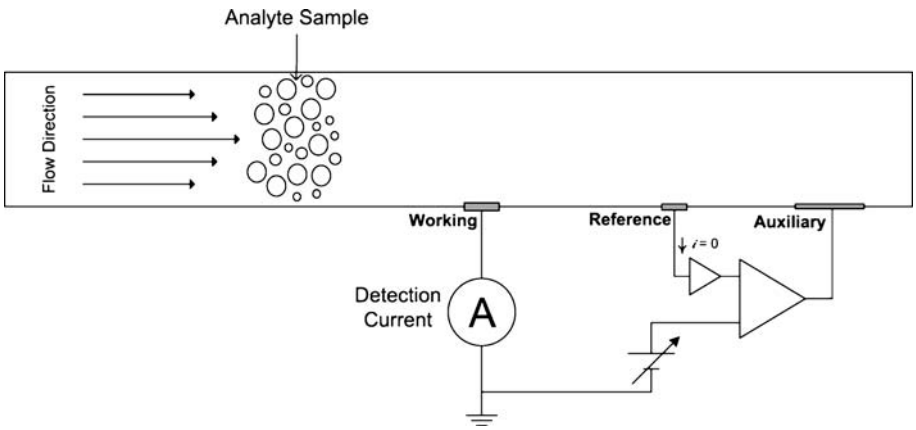

Amperometric Techniques, Figure 2 Schematic of amperometric detection cell (general representation for Lab-on-a-Chip (LOC) applications

capacitance, C_{DL}. The size of this capacitance is a function of electrode area, electrode-to-solution potential, electrode material, and the ion concentration in solution. The potentiostat compensates only for capacitance, impedance, and resistance (C_{DLA}, R_c, Z_{FA}) within its control loop and allows these to be largely ignored experimentally. Therefore, the uncompensated resistor, R_u, which is outside the loop, causes an error in the working electrode potential, iR_u, as a result. However, given the very small amplitude currents usually involved in microfluidic systems and the relatively low resistivities of the aqueous electrolyte solutions normally employed, this error is seldom of any practical concern for amperometric measurements. Of course, the product $R_u C_{DL}$ represents the cell time-constant and largely determines the speed of response of the cell to any change in the applied potential. For typical amperometric detection applications where the applied potential is kept constant throughout the entire experiment, this also is of no concern; but, for the relatively few cases in which the potential is systematically scanned during the CE separation, limitations in accurate control of the working electrode potential due to charging of C_{DLW} must be considered.

Application of amperometric detection to HPLC instrumentation is usually straightforward, involving the placement of conventional size electrodes downstream from the column exit. Care must be given to keep the dead-volume entailed by the detection cell and connecting tubing small enough to avoid compromising the separation efficiency. For CE/EC systems, however, there are two specific issues that must be addressed experimentally: 1) physical alignment of the electrodes with the capillary or channel outlet; and, 2) electrical decoupling of the EC detection from the high-voltage CE field. The need to optimize capillary/electrode alignment arises from the very small dimensions involved – with the widths of both CE channels and EC electrodes typically in the 10 – 100 μ range. Thus, optimum sensitivity dictates that the working electrode is placed very near the channel outlet while acceptable reproducibility requires that this positioning, once established, be maintained throughout extended sets of experiments. With bench-top CE instrumentation, this usually requires the use of microscopes and 3D micro-positioners to align the fiber or wire with respect to the capillary. Alternative arrangements to ease this problem have been suggested such as the use of planar "wall-jet" electrodes that can be somewhat larger in size or the incorporation of the EC electrode onto the capillary by deposition of an appropriate metallic film onto its outside tip. Of course, one of the attractive features of Lab-on-a-Chip CE/EC systems is that the specific location, size, and shape of the EC electrodes can be absolutely controlled during the microfabrication process.

In amperometric detection, the placement of the working electrode in CE/EC detection systems can be divided into three different categories, *off-channel (or column)*, end-*channel (or column)* and in-*channel detection.* The purpose of this distinction is to indicate the location of the EC electrodes with respect to the CE electrodes and field (Fig. 4). This is an important consideration because of the possible interactions that might occur, as mentioned above, between the EC and much larger CE electric fields. "Off-channel" EC detection refers to the situation in which an electrically conducting "fracture" or thin crack, opening, or hole is created in the capillary or channel wall a short distance before the exit. This fracture allows the CE voltage and current to be dropped before the actual physical end of the system and permits the EC electrodes to be placed near or even inside the capillary exit for efficient analyte detection but nevertheless to remain

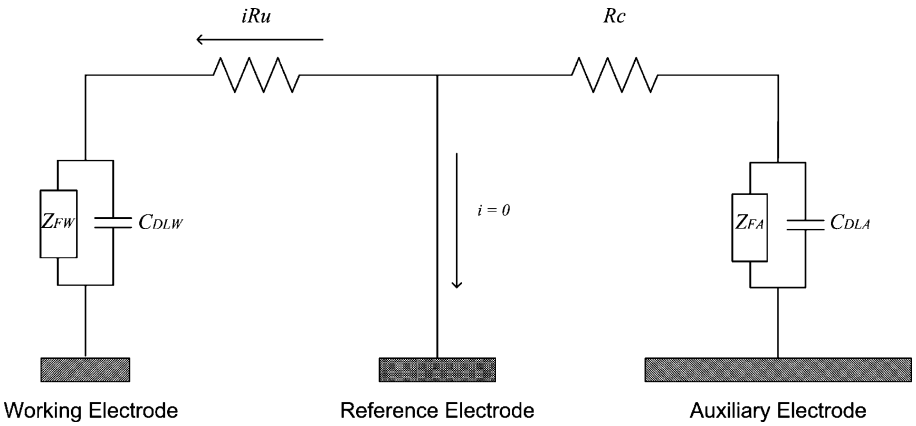

Amperometric Techniques, Figure 3 Electrical model of three-electrode cell (Z_{FW} is the faradaic impedance at the working electrode; C_{DLW} is the double-layer capacitance at the working electrode; Z_{FA} is the faradaic impedance at the auxilary electrode; C_{DLA} is the double-layer capacitance at the auxilary electrode; R_C is the resistance of the electrochemical cell; R_u is the uncompensated resistance; and, i is the current)

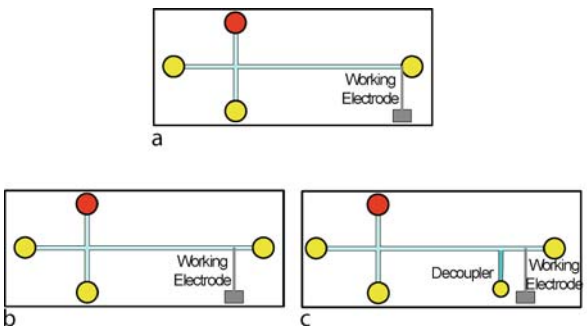

Amperometric Techniques, Figure 4 Schematic of EC electrode placement for the different detection electrode configurations: (**a**) end-channel detection; (**b**) in-channel detection; and, (**c**) off-channel detection

"off" or outside the influence of the CE field, commonly referred to as "decoupling" [7, 8]. The off-channel approach, which often may pose significant technical difficulties to implement, offers the possibility of very efficient detection of the analyte while it is still contained within the confines of the narrow separation channel and remains in the form of a relatively concentrated plug. "End-channel" detection refers to the more convenient placement of the EC detection electrode just beyond the end of the separation channel in the CE buffer reservoir. Thus, the EC cell is located within the high-voltage CE field, and electrical interactions between the two are still possible. However, as long as the CE capillary or channel width is sufficiently small, its ohmic resistance is high enough that the CE current is negligibly small and only a very small portion of the CE voltage extends beyond the exit and into the much larger volume detection compartment. Of course, an inherent problem with this technique is that the well-defined analyte plugs maintained within the capillary immediately begin to spread radially upon exiting and moving into the much larger volume detection reservoir. Therefore, care must be taken that the detection electrode, in this case, is located close to the exit of the channel, typically 25 – 100 μm, but not so close as to interact unduly with the residual CE voltage that does extend slightly beyond the separation channel. A detailed study of the residual post-capillary CE field, and the effect of end-channel electrode placement, has been reported by Klett et al. [9]. The in-*channel* approach has been employed by researchers, however, this approach is limited due to bubble generation in the channel, which can significantly decrease the signal-to-noise (S/N) ratio of the electrochemical signal, as well as the high electric field can significantly effect the resting background current generated at the surface of the working electrode.

In regards to electrode geometry, the EC detector response is proportional to electron generation (or consumption) during the desired redox reaction. Therefore, increasing the area of the detection electrode will increase the detection signal. The tradeoff is that the background noise increases linearly as well. Due to the confined geometry of the microchannel, in-channel electrodes are limited to simple rectangular shapes determined by the channel width and exposed electrode area. This configuration is sufficient to maximize the contact of the analyte with the electrode surface. For an end-channel electrode configuration, however, a simple rectangular planar electrode is not the only option. The conventional planar geometry can be altered to match the shape of the radially migrating analyte so as to maximize the delivery of the sample to the detection electrode surface.

Key Research Findings

The first microfluidic *Lab-on-a-Chip* (LOC) devices were reported by Harrison and Manz in the early 1990s. These devices consisted of simple channels, several cm in length and 10 – 100 μm in width and depth, etched into glass microscope slides or silica plates via conventional micromachining techniques [10]. In this work, samples were injected onto the chip and moved as required through the channel network by electroosmotic flow; separations were carried out by electrophoretic mechanisms common to bench-scale CE instrumentation; and target analytes were detected and quantitated via fluorescence detection. Subsequent studies by these and other groups demonstrated unique advantages for the Lab-on-a-Chip approach: high separation efficiencies, short analysis times, minute sample and reagent consumption, high sample throughput, and easy automation.

In 1996, the first use of amperometric detection in microchip CE devices was reported by Wooley, Lao, Glazer and Mathies [11] who used off-chip CE driving electrodes together with a photolithographically patterned Pt electrode placed just outside the CE channel for on-chip detection of catechol neurotransmitters by direct oxidation and DNA fragments and PCR products indirectly by EC monitoring of an electroactive intercalating agent. In another end-channel approach, Baldwin and colleagues [12] were the first to demonstrate a Lab-on-a-Chip device that incorporated both CE high-voltage electrodes and all amperometric EC detection electrodes directly onto an integrated, microchip platform. Key features of their device were the formation of a "shelf or ledge" at the end of the separation channel to restrict the height of the detection reservoir near the working electrode and the radial pattern of the working electrodes. These features enabled optimization of EC detection by decreasing the electrical resistance and CE voltage drop in the detection region and increasing the residence/contact time of the analytes with the working electrode, respectively. Another novel CE microchip end-column approach has been reported by Ertl et al. [13], which integrates sheath-flow into the CEEC system to increase analyte velocity in the detection reservoir as it exits the CE separation channel. Their study further elucidated the importance of the spacing between the working and reference electrodes, with optimum detector performance achieved for a spacing of ∼ 20 μm. Using an electrically isolated potentiostat with a floating working electrode, Martin and coworkers [14] successfully detected catechol with minimum band-broadening effects by placing the working electrode just inside the separation channel but without any decoupling. Off-channel EC detection approaches have been also explored in microchip platforms. For example, the Lunte groups demonstrated two different methods for decoupling the CE field from the EC detection system. In the first, decoupling was achieved by laser-cutting a series of 20, 30 μm holes in the roof of the CE channel into the upper glass coverplate and then filling them with cellulose acetate [8]. In the second, a 500 μm wide Pd decoupler strip was fabricated via photolithography and sputter-coated onto the glass substrate that formed the bottom of the CE channels [15]. When placed directly in the CE channel and used as the CE cathode, the Pd was able to absorb the H_2 gas that is generated during normal CE operation and leads to the formation of bubbles in the channel. The key advantages of these approaches (and others like them) are that they allow microchips to operate at higher field strengths (up to 1700 V/cm) with superior limits of detection (∼ 25 nM for dopamine with a carbon fiber electrode) and allow the EC working electrode to be placed in-channel where higher efficiency separations can be realized. Similarly, Lai et al. [16] integrated a Pd-film decoupler with a series-dual electrode to significantly enhance the oxidation current when switching between the single electrode mode and dual-series mode. In other work, Wu et al. [17] electrodeposited Pt nanoparticles on a Au ground electrode to construct the decoupler and achieved a limit of detection of 0.125 μM at a $S/N = 4$ for dopamine with a Au working electrode.

Compared to alternative detection approaches, amperometric methods are ideally suited to microfabrication processes since the electrodes themselves have the ideal dimensions (1 to 10 μm) for incorporation onto a microchip. Most importantly, patterning and construction of EC microelectrodes is extremely compatible with mainstream microfabrication technologies such as photolithography and sputter-coating. As a result, electrodes (and electrochemical cells) of different shape, size, location, and composition can be patterned directly onto glass, silica, and other substrates with a high degree of accuracy using the same photolithographic techniques employed to fabricate the microchip's CE channels, thereby allowing the detection operation to be fully integrated onto the chip (Fig. 5). In addition, multiple electrodes in different CE channels or multiple electrodes with different response characteristics can be created to allow the device to fit the intended application optimally (Fig. 5b). This level of integration does not exist with other detection approaches and has several performance and applications advantages. For example, with LIF, multi-channel detection requires either the use of multiple fluorescence systems or a means of scanning a single fluorometer across multiple spots on the chip.

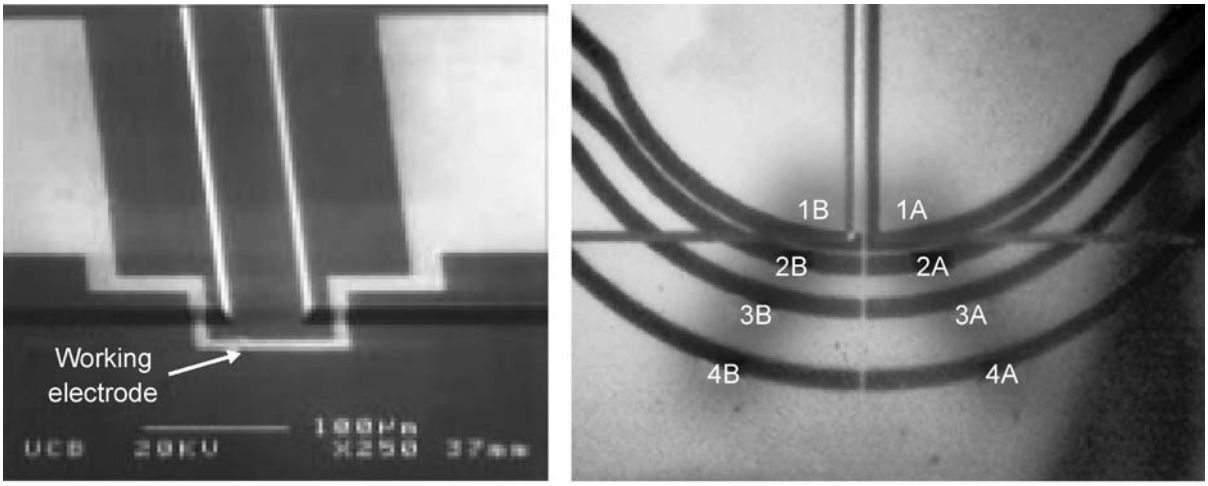

a b

Amperometric Techniques, Figure 5 Examples of different electrode geometries that can be fabricated via photolithographic techniques: (**a**) rectangular working electrodes (Reprinted with permission from [11]); and, (**b**) multiple radial working electrodes (Reprinted with permission from [18])

Chip-based amperometric EC detection techniques have been utilized in several noteworthy analysis situations – most commonly in clinical (e. g., immunoassays and protein analysis) and environmental sensing. A recent review by Vandaveer et al. [19] provides an excellent overview of these applications.

Future Directions for Research

Considering the relative ease with which prototypes can be developed on the micro-scale, custom EC electrode configurations mated perfectly to the CE separation platform are possible. For example, devices with multiple separation channels may be outfitted with multiple EC cells, each identical to the other to establish redundancy for fail-safe detection. Each channel could run simultaneously and statistical calculations (running averages, standard deviations, etc.) could be used to enhance both the reliability of detection and the robustness of the detection system. The development of such advanced LOC instruments is expected to be central to their practical utilization in applications involving remote and unattended sensing.

Another possibility would be for each channel of a multiple channel CE/EC system to be configured with an EC cell specifically designed to detect a different analyte or analyte group. This could be accomplished, for instance, by maintaining each EC electrode at a different potential, fabricating each detection electrode out of a different substrate, or modifying each electrode chemically or biochemically. In this case, there would be no redundancy; however, a single experiment could yield results for a range of analyte components. Furthermore, alternative microfabrication techniques can be developed to create electrodes with alternative geometries, such as flow through or three-dimensional, large surface area detection electrodes. Increased surface area electrodes allow for a more complete interaction between the analyte and the detector which should be expected to enhance the signal-to-noise ratio and sensitivity.

A relatively new area which is likely to grow in importance is the construction/functionalization of the EC electrodes with alternative materials to enhance the reactivity toward the analyte or to allow detection of analytes that do not oxidize or reduce ideally at simple electrodes. For example, Marwan et al. [20] reported the functionalization of glassy carbon electrodes with metal-based species in order to elicit the electrochemical reduction of nitrates and oxidation of hydrogen peroxide. Similarly, Sarapuu et al. [21] have shown the modification of boron-doped diamond and highly oriented pyrolytic graphite electrodes with quinones to greatly enhance the rate of oxygen reduction, thereby allowing a highly sensitive determination of hydrogen peroxide. Biological molecules (DNA, antigens, etc.) which are often not inherently electroactive can be detected electrochemically by approaches such as Kavanagh's [22] in which a redox polymer and a single-stranded DNA probe were attached to a gold electrode; hybridization and formation of the double-stranded probe DNA altered the electrochemistry of the polymer and thereby permitted detection of the complementary DNA species. Continuing research into further functionalization of traditional and modified electrode materials will further enhance sensitivity and promote selectivity between ana-

lytes, especially in the areas of clinical and biochemical analysis.

An alternative approach gaining widespread attention is the addition of an electrochemically active tag or label to an electro-inactive biomolecule such as DNA, SNPs, etc. Similarly to fluorescence detection, in which a sample is treated with a natively fluorescent chemical marker in order to render it optically detectable, this technique tags the sample at a specific site with a molecule that undergoes oxidation/reduction at a well-characterized electrode system. Wooley, et al. [11] first proposed this promising approach in 1998. Since then, others have demonstrated the ability to carry out this technique on a microchip platform. Hebert and colleagues [23, 24] have detected a specific SNP (Single Nucleotide Polymorphism) site using an electrochemically active taggant in conjunction with sinusoidal voltammetry, while Wang and coworkers [25] labeled amino acids with electrochemically active 1-cyanobenz(f)isoindole derivatives to permit the detection of arginine, lysine, phenylalanine, glycine and cysteine. Given the inherent sensitivity of EC and the flexibility of microfabrication, this line of research is expected to have a major impact on the detection of many important biomolecules.

Cross References

- ► Capillary Electrophoresis
- ► Electroosmotic Flow (DC)
- ► Electrophoresis
- ► Surface Conductivity Measurement
- ► Potentiometry

References

1. Kissinger PT, Ridgway TH (1996) Small-Amplitude Controlled-Potential Techniques. In: Kissinger PT, Heineman WR (eds) Laboratory Techniques in Electroanalytical Chemistry, 2nd edn. Dekker, New York
2. Wallingford RA, Ewing AG, (1987) Capillary zone electrophoresis with electrochemical detection. Anal Chem 59:1762–1766
3. Haber C (1996) In: Landers JP (ed) Electrochemical detection in capillary electrophoresis. Handbook of Capillary Electrophoresis, 2nd edn. CRC, Boca Raton
4. Sloss S, Ewing AG (1993) Improved method for end-column amperometric detection for capillary electrophoresis. Anal Chem 65:577–581
5. Wang J (2000) Analytical Electrochemistry, 2nd edn. Wiley-VCH, New York
6. Bard AJ, and Faulkner LR (2001) Electrochemical Methods: Fundamentals and Applications, Chapter 13, 2nd edn. Wiley, Hoboken, p 580
7. Osbourn DM, Lunte CE (2001) Cellulose acetate decoupler for on-column electrochemical detection in capillary electrophoresis. Anal Chem 73:5961–5964
8. Osbourn DM, Lunte CE (2003) On-column electrochemical detection for microchip capillary electrophoresis. Anal Chem 75:2710–2714
9. Klett O, Björefors F, Nyholm L (2001) Elimination of high-voltage field effects in end-column electrochemical detection in capillary electrophoresis by use of on-chip microband electrodes. Anal Chem 73:1909–1915
10. Harrison DJ, Manz A, Fan Z, Ludi H, Widmer HM (1992) Capillary electrophoresis and sample injection systems integrated on a planar glass chip. Anal Chem 64:1926–1932
11. Woolley AT, Lao K, Glazer AN, Mathies RA (1998) Capillary electrophoresis chips with integrated electrochemical detection. Anal Chem 70:684–688
12. Baldwin RP, Roussel Jr. TJ, Crain MM, Bathlagunda V, Jackson DJ, Gullapalli J, Conklin JA, Pai R, Naber JN, Walsh KM, Keynton RS (2002) Fully-integrated on-chip electrochemical detection for capillary electrophoresis in a microfabricated device. Anal Chem 74:3690–3697
13. Ertl P, Emrich CA, Singhai P, Mathies RA, (2004) Capillary electrophoresis chips with a sheath-flow supported electrochemical detection system. Anal Chem 76:3749–3755
14. Martin RS, Ratzlaff KL, Huynh BH, Lunte SM (2002) In-channel electrochemical detection for microchip capillary electrophoresis using an electrically isolated potentiostat. Anal Chem 74:1136–1143
15. Lacher NA, Lunte SM, Martin RS (2004) Development of a microfabricated palladium decoupler/electrochemical detector for microchip capillary electrophoresis using a hybrid glass/poly(dimethylsiloxane) device. Anal Chem 76:2482–2491
16. Lai CCJ, Chen CH, Ko FH (2004) In-channel dual-electrode amperometric detection in electrophoretic chips with a palladium film decoupler. J Chromatogr A 1023:143–150
17. Wu CC, Wu RG, Huang JG, Lin YC, Chang HC (2003) Three-electrode electrochemical detector and platinum film decoupler integrated with a capillary electrophoresis microchip for amperometric detection. Anal Chem 75:947–952
18. Keynton RS, Roussel TJ, Crain MM, Jackson DJ, Franco DB, Naber JF, Walsh KM, and Baldwin RP (2004) Design and development of microfabricated capillary electrophoresis devices with electrochemical detection. Anal Chim Acta 507:95–105
19. Vandaveer IV WR, Pasas-Farmer SA, Fischer DJ, Frankenfeld CN, Lunte SM (2004) Recent developments in electrochemical detection for microchip capillary electrophoresis. Electrophoresis 25:3528–3549
20. Marwan J, Addou T, Belanger D (2005) Functionalization of glassy carbon electrodes with metal-based species. Chem Mater 17:2395–2403
21. Sarapuu A, Helstein K, Schiffrin DJ, Tammeveski K (2005) Kinetics of oxygen reduction on quinone-modified HOPG and BDD electrodes in alkaline solution. Electrochem Sol State Lett 8:E30–E33
22. Kavanagh P, Leech D (2006) Redox polymer and probe DNA tethered to gold electrodes for enzyme-amplified amperometric detection of DNA hybridization. Anal Chem 78:2710–2716
23. Hebert NE, Snyder B, McCreery RL, Kuhr WG, Brazill SA (2003) Performance of pyrolyzed photoresist carbon films in a microchip capillary electrophoresis device with sinusoidal voltammetric detection. Anal Chem 75:4265–4271
24. Hebert NE, Kuhr WG, Brazill SA (2003) A microchip electrophoresis device with integrated electrochemical detection: A direct comparison of constant potential amperometry and sinusoidal voltammetry. Anal Chem 75:3301–3307

25. Wang J, Chen G, Pumera M (2003) Microchip separation and electrochemical detection of amino acids and peptides following precolumn derivatization with naphthalene-2,3-dicarboxyaldehyde. Electroanalysis 15:862–865

Amphoteric Ion Exchange Membrane

Definition

An ion exchange membrane which includes both a weak anioin exchange and a weak cation exchange functionality in to the same membrane. This type of membrane has the ion exchange functionalities distributed randomly throughout the membrane.

Cross References

► Ion Exchange Membranes

Analysis/Design

► Control of Micro-Fluidics

Analysis of Individual Cell Contents

► Single Cell Analysis in Microfluidic Devices

Analyte

Definition

An *analyte* is the substance or chemical constituent that is undergoing analysis. It is the substance being measured in an analytical procedure. For instance, in an immunoassay, the analyte may be the ligand or the binder.

Cross References

► Biosensor
► Chemical Analysis
► Bio-Analysis

Analytical Method

► Analytical Modeling

Analytical Modeling

Synonyms

Analytical method

Definition

Analytical modeling is to seek for mathematical functions and equations that are obtained from the closed-form (exact or approximate) solution to the original physics-governing equations. The outcome of analytical modeling is behavioral models.

Cross References

► Behavioral Model

Anion

Definition

Negatively charged ion that moves towards the anode in electrophoresis.

Cross References

► Electrophoresis

Anion Exchange Membrane

Definition

An ion exchange membrane that interacts with anions and typically consist of amine functionalities ($-NH_3^+$, $-NRH_2^+$, etc). These functionalities allow anions to pass through the membrane and prevents cations from passing through the membrane. The ability of the membrane to bind ions is greatly dependant on the pH of the solution and the ions of intrest.

Cross References

► Ion Exchange Membranes

Anisotropic Etching

DUSTIN HOUSE, DONGQING LI
Department of Mechanical Engineering,
Vanderbilt University, Nashville, TN, USA
dustin.l.house@vanderbilt.edu

Synonyms

Silicon etching; Etching single crystalline materials; Potassium hydroxide (KOH) etching; Deep reactive-ion etching (DRIE); Bosch process; Physical-chemical etching

Definition

Anisotropic etching is a subtractive microfabrication technique that aims to preferentially remove a material in specific directions to obtain intricate and often flat shapes. Wet techniques exploit the crystalline properties of a structure to etch in directions governed by crystallographic orientation. Dry techniques utilize an inhibitor to protect the sidewalls of a cavity during ion bombardment to obtain high aspect ratios.

Overview

In contrast to isotropic etching, anisotropic etching is a fabrication technique that removes material in specific directions allowing for the production of geometric characteristics such as sharp corners, flat surfaces, and deep cavities. Relative to microfabrication, selectivity can be defined as the ratio of the etch rate of the target material to the etch rate of other materials. The definition can also be applied more specifically to single crystalline materials such as silicon where it would be considered the ratio of the etch rate in the target direction to the etch rate in other directions.

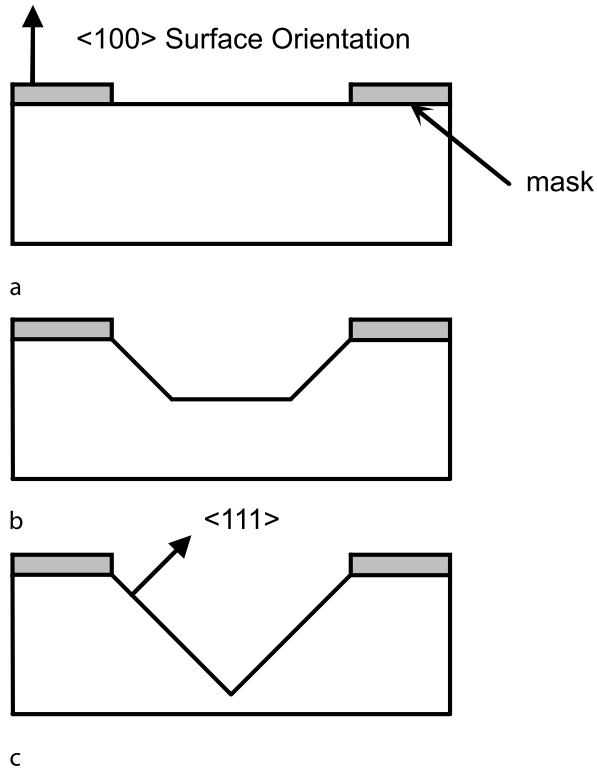

Anisotropic Etching, Figure 1 Example of a masked silicon wafer with a ⟨100⟩ surface orientation (**a**) before, (**b**) during, (**c**) and after exposure to a potassium hydroxide etch

Different etchants used in anisotropic wet etching have specific etch rates for each crystallographic plane in the material being removed. It is the difference in etch rates between planes that produce shapes within the material being etched that appear to follow the planes within the crystalline structure as seen in Fig. 1. For more information on the crystalline structure of silicon and how miller indices are used in designating crystal planes, see The MEMS Handbook [1]. It is commonly accepted that the ⟨111⟩ plane etches the slowest regardless of the etchant used. However, the crystal plane that etches the fastest depends on the etchant composition [2]. Ammonium hydroxide etchants (NH_4OH and TMAH) are frequently used to etch silicon due to their compatibility with certain metals involved in on-chip circuitry, whereas alkali hydroxide etchants (NaOH, CsOH) are used for their faster etch rates [3]. A commonly used alkali hydroxide etchant for silicon is potassium hydroxide (KOH) which provides a high level of selectivity between the ⟨100⟩ and ⟨111⟩ planes. Materials that are highly resistant to these etchants, such as silicon nitride and silicon dioxide are often utilized as etch stops in more complex designs. Detailed specifications for each etchant including etch rates in specific crystal planes, and recommended temperatures, concentrations and etch stops is available in the literature such as those of Nguyen and Wereley [2].

Careful design and alignment of the mask must be ensured when involving directional dependence in the etching process. Because the planes will continue indefinitely until they reach a surface or another plane, undercutting of the masking material is possible. A shape that does not align with the correct planes can produce an opening that circumscribes the original shape if etched long enough as seen in Fig. 2. The angle produced between the slow-etch plane and the surface after etching is clearly dependent on surface orientation and the crystalline structure of the material. Such angles are found in the literature and are utilized in design to achieve accurate depths and specific slopes (including vertical). Equipment used in wet etching can be easily obtained in most laboratories. The material being etched is suspended within a beaker containing the etchant while a magnetic stirrer ensures continuous transport of reactants to and products from the surface of the material. A simple temperature-controlled hot-

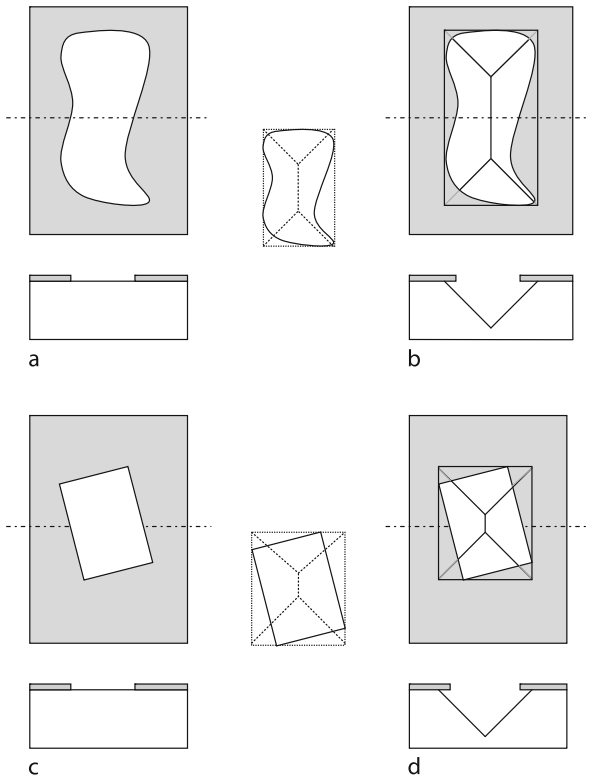

Anisotropic Etching, Figure 2 Examples of undercutting that is possible for (**a**,**b**) odd shaped masks and (**c**,**d**) misaligned masks relative to crystal planes

plate regulates the optimum temperature.

Anisotropic dry etching is a method for creating high aspect ratio trenches with nearly vertical walls. The two common techniques utilize a protective coating along the vertical walls of an etched trench such that the bottom of the trench etches at a faster rate allowing for large aspect ratios. Each is independent of crystal orientation. The first method forces the reactant gases to condense on the sidewalls of the trench by lowering the temperature of the materials with liquid nitrogen. Ions are then accelerated toward the trench by means of an electric field. This physical shower of ions results in an etching effect. After ion bombardment removes the bottom layer, it can be etched further while the sidewalls are protected by the cryogenically frozen inhibitor. Another novel approach, commonly referred to as the Bosch process (named after its inventor, Robert Bosch) alternates additive and subtractive microfabrication techniques. During the additive stage, chemical vapor deposition is used to coat the sidewalls of the trench with a polymeric passivation layer. Similarly to the previous method, ion bombardment is then used to sputter off the trench bottom, exposing the substrate to the chemical etchant [4]. Several companies specialize in the production of microfabrication equipment for various reactive ion etching processes. These processes, commonly referred to as deep reactive ion etching (DRIE) are capable of producing channels with a depth on the order of 500 μm and aspect ratios on the order of 30 : 1 [5].

Cross References

- ► Bulk Micromachining
- ► Dry Chemical Etch
- ► Fabrication of 3D Microfluidics Structures
- ► Isotropic Etching
- ► Microfabrication Techniques
- ► Plasma Etching
- ► Reactive Ion Etching (RIE)
- ► Silicon Micromachining
- ► Sputter Etching
- ► Wet Chemical Etch

References

1. Gad-el-Hak M (2002) The MEMS Handbook. CRC Press, Florida
2. Nguyen N, Wereley S (2002) Fundamentals and Applications of Microfluidics. Artech House, Inc., Massachusetts
3. Lobontiu N, Ephrahim G (2005) Mechanics of Microelectromechanical Sytems. Springer Science + Business Media, Inc., Massachusetts
4. Franssila S (2004) Introduction to Microfabrication. Wiley, West Sussex
5. Tabeling P (2006) Introduction to Microfluidics. Oxford University Press, Oxford

Anisotropic Silicon Etching

- ► Silicon Micromachining

Anisotropic Silicon Micromachining

- ► Bulk Micromachining

Anisotropy

Definition

The directional dependency of a measurable property of a material.

Cross References

- ► Sputtering for Film Deposition

ANN

► Artificial Neural Networks

Anode

Definition

Positively charged electrode.

Cross References

► Electrophoresis

Anodic Bonding

ZHENG CUI
Rutherford Appleton Laboratory, Oxford, UK
z.cui@rl.ac.uk

Synonyms

Field assisted bonding; Electrostatic bonding

Definition

Anodic bonding is a technique to produce hermetic seals between metals and glass insulators. Anodic bonding is mostly used for hermetic sealing of silicon and glass. Different from other sealing techniques, anodic bonding involves heating and applying an electrical field to a bonding pair.

Overview

The anodic bonding technique was first reported in 1969, with the name of field assisted glass–metal sealing [1]. It has since been developed into a widely used hermetic sealing technique for a variety of MEMS devices and microfluidic devices. The equipment for anodic bonding can be simply a hot plate on which the bonding parts are heated to the sealing temperature between 300 and 600 °C and a DC power supply to apply a high voltage from 200 V up to 2000 V to the bonding parts. The bonding process takes only a few minutes. Figure 1 shows schematically the setup for anodic bonding, where the conductive part, in this case a silicon wafer, is connected positively to the applied voltage. The essential conditions for anodic bonding are:

1. The bonding surfaces should be flat and well polished to less than 5 nm in surface roughness. When the bonding pair is put together, the two parts are in intimate contact at the polished surfaces.
2. The materials of the bonding pair must have well matched thermal expansion coefficients.
3. Anodic bonding only occurs between conductive materials and glass materials.

The mechanism of anodic bonding is believed to be both physical and chemical. The physical mechanism is electrostatic force. At the typical bonding temperature, most glass materials contain mobile positive ions compensated by almost immobile negative ions. Upon applying high voltage, these positive ions migrate to the negative electrode connected to the glass and become largely neutralized, leaving a depletion layer with negative space charge at the contact interface. Figure 2 shows the typical electrical current profile during anodic bonding [2]. The initial rise of current represents the migration and neutralization positive ions at the electrode. Then the current drops and a depletion layer is built up at the interface. The contact interface, although well polished at both sides, initially has only a few points of physical contact. Therefore, there is a high electrostatic field generated from the negative charge layer at the gaps. The high electrostatic attractive force then pulls the surfaces into direct contact, which explains why the bonding always starts at the point contact of electrode and spreads radially. The radial spreading of the bonding front makes it impossible for air to become trapped between the bonding surfaces. The electrostatic force depends on a number of factors, such as the total applied voltage, the width of the gap, the concentration and distribution of ions in the glass, whether under the high field the negative ions will drift out of the glass or the positive ions will drift into the glass and possible formation of surface charge on the glass (the effect of such charge would partially shield the charge in the glass, thus reducing the field in the gap).

The chemistry of anodic bonding is an oxidation process at the interface. Due to the high electrostatic field, oxygen anions leave the glass and create Si–O–Si bonds, i.e., a thin layer of SiO_2 is formed. This gives the strong bond between silicon and glass, and the bonding becomes irreversible. The formation of thin SiO_2 layer at the bonding interface has been verified by Rutherford backscattering spectroscopy. It has also been demonstrated that the rate of oxygen release is directly proportional to the average current passing through the bonding area. In areas where silicon and glass are in direct contact due to electrostatic attractive force, the oxygen anions will oxidize the silicon into SiO_2 and form the anodic bond. The oxygen is therefore totally consumed. However, in areas where silicon is

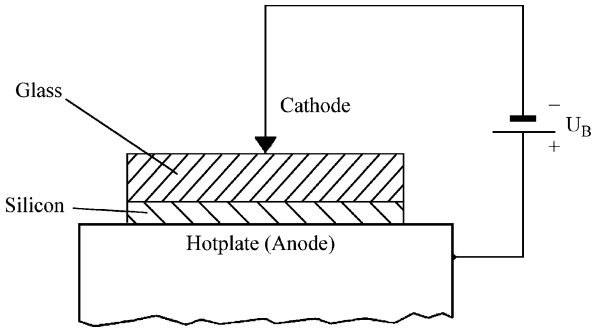

Anodic Bonding, Figure 1 Schematic setup for anodic bonding of silicon to glass

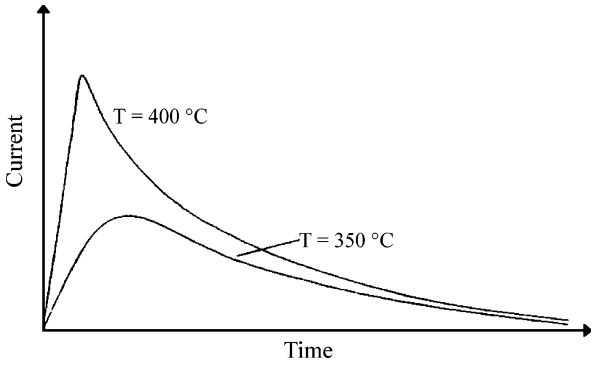

Anodic Bonding, Figure 2 Current profiles during anodic bonding at different temperatures

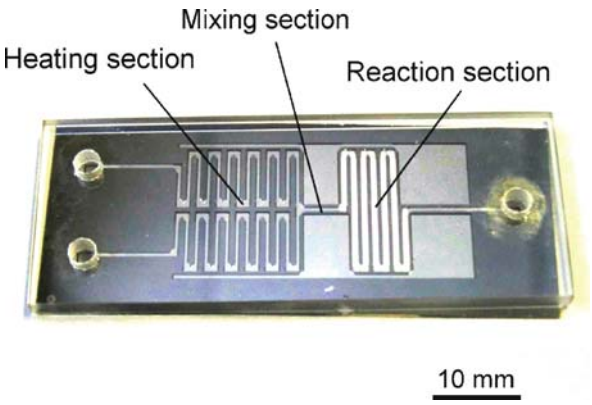

Anodic Bonding, Figure 3 Microreactor chip assembly by anodic bonding of silicon and glass

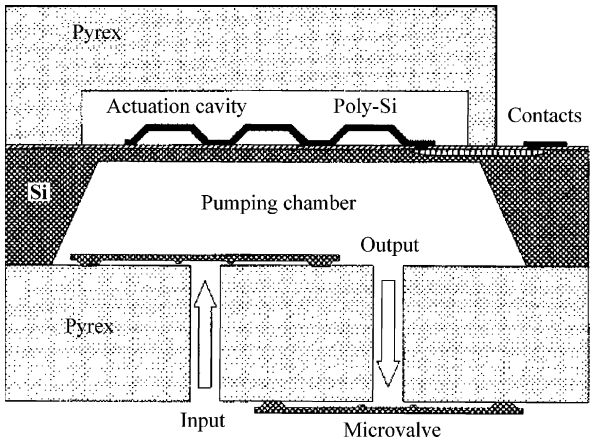

Anodic Bonding, Figure 4 Schematic cross-section of a micropump assembled by anodic bonding of glass–silicon–glass

not in direct contact with glass, for example in the case of an etched cavity into the glass or silicon, oxygen evolution into the cavity can occur. This may have detrimental effects in some device applications [3].

The bonding strength for silicon–glass anodic bonding is measured typically at 10 – 20 MPa. Some have reported between 30 MPa and 40 MPa at higher bonding voltage [2]. The pull test has demonstrated that bonding strength is higher than the fracture strength of the glass, i.e., the break in the pull test occurs only in the glass and not at the silicon–glass interface.

Anodic bonding of glass and silicon has found many applications in microsystems, MEMS and microfluidics, including the fabrication of pressure sensors, accelerometers, micropumps and other fluid handling devices. A typical microfluidic device is shown in Fig. 3, which is a microreactor chip to perform chemical synthetic reactions [4]. The microreactor was made by wet or dry etching of silicon to form microchannels and sealed by anodic bonding of a glass slide on top with inlet and outlet holes. Anodic bonding can provide an airtight seal to ensure proper function of fluidic flow in the microchannels. Silicon is a preferred material in microfluidic systems because micromachining of silicon is the most mature fabrication technique. Complex structures can be made in silicon by either wet chemical or reactive ion etching. Anodic bonding of silicon with glass can also help in the building of multistack microsystems to perform complicated functions. Figure 4 shows an example of a micropump made by silicon/glass micromachining and anodic bonding [5]. This is a glass–silicon–glass multistack system. The top Pyrex glass provides a hermetically sealed cavity so that the polysilicon heater can heat up the air in the cavity. Expansion of the hot air in the cavity will compress the silicon membrane to perform a pumping action in the pumping chamber. The bottom Pyrex glass seals the pump chamber as well as provides the input and output holes for fluid flow in and out of the pump chamber.

Anodic bonding is the primary method for packaging silicon microstructures, for example packaging of pressure sensors, accelerometers and solar cell panels, because of

its relatively low bonding temperature. With bonding temperature being below the glass transition point, the glass thermal expansion coefficient remains constant, which enables stress-free packaging of silicon microstructures (provided the glass has a good thermal expansion match with silicon over the process temperature range). In addition, with the low bonding temperature there is no measurable flow of glass, which ensures sealing around silicon microstructures without any loss of dimensional tolerances. Apart from low bonding temperature, there are other attractive features of anodic bonding:

- Since glass is an electrical insulator, parasitic capacitances are extremely small.
- The bonding process can be readily performed in vacuum, allowing hermetic sealing or zero pressure reference cavity to be formed (or sealing with special gas mixtures).
- The transparency of glass allows optical inspection or detection of fluidic flow/reaction in microfluidic devices. It also facilitates alignment of microstructures in glass with microstructures in silicon.

Although glass–silicon sealing or assembly is the most common form of anodic bonding, the technique can also be applied to the sealing of many metals with a variety of glasses. Successful seals have been made with borosilicate glass, soda lime glass, potash soda glass, aluminosilicate glass, fused silica and fiber optical glass [1]. Strong seals have also been made to some ceramic materials. For those metals and alloys whose thermal expansion coefficients are matched to the above glasses, successful anodic bonding have also been made, such as tantalum, titanium, Kovar, Niromet 44, and to semiconductors such as germanium and gallium arsenide, in addition to silicon [1].

Basic Methodology

Although the principle of anodic bonding is simple, successful bonding depends on appropriate selection of bonding materials, good preparation of bonding surfaces, optimization of bonding conditions and inspection of bonded samples. These are explained in the example of silicon–glass anodic bonding.

Material Selection

Silicon material is normally of standard wafer sizes and thicknesses. As the anode part of the bonding pair, the silicon should be low in resistivity. However, some applications require an insulating layer to prevent electrical leakage in silicon. In this case, a thin layer of silicon dioxide or silicon nitride should be deposited on the silicon surface. The insulating layer does not prevent anodic bonding of silicon with glass. However, a thicker insulating layer can increase the bonding time dramatically. For example, for a 0.5 μm thick oxide layer a bonding time of approximately five times longer is required [2]. For anodic bonding with glass, p-type silicon wafers (boron doped) are preferred, as a high electrostatic field is much easier to build up, particularly at low temperature, at the silicon side of a silicon–glass interface for p-type silicon than for n-type silicon (phosphor doped) [6]. However, for high-temperature anodic bonding (> 400 °C) the doping type of silicon is no longer a factor.

Borosilicate glasses such as Corning 7740 Pyrex glass, Schott Borofloat 33 glass and Hoya SD-2 glass are commonly used for anodic bonding with silicon. They are of almost the same coefficient of thermal expansion (CTE) as that of silicon. They also have the necessary electrical conductivity at the bonding temperature. However, some special applications require the glass to be high in resistivity (Corning 7070 glass) or high in spectral transmission (Pilkington CMZ glass). Glasses that have a CTE different from silicon or a low concentration of mobile positive ions are still able to be anodically bonded with silicon, but with special process conditions. For example, to bond Corning 7070 glass with silicon, much higher temperature and voltage are needed. To bond a Fisher glass slide whose CTE is very different from that of silicon, the bonding temperature has to be much lower (150 °C) and bonding time is much longer (60 min) [6].

Preparation of Bonding Surfaces

A well-polished surface is essential for a successful bonding. The average surface roughness (R_a) should be less than 5 nm. Commercial silicon wafers and glass substrates are normally polished to this standard. Although anodic bonding is fairly tolerant to particles and contaminations on the bonding surfaces, they still need to be cleaned prior to anodic bonding, unless the wafers are straight out of the box. A study has demonstrated that a $H_2SO_4 + H_2O_2$ acidic clean of bonding surface can significantly reduce the bonding time compared to a simple cleaning with acetone [6]. Thorough cleaning is even more important for structured wafers. Whether the bonding surfaces are hydrophobic or hydrophilic can also have an influence on bonding. At low temperature, a hydrophilic surface is easier to bond than a hydrophobic surface. However, such difference disappears at high bonding temperature [7].

Process Parameters

The basic process parameters for anodic bonding are temperature, voltage, clamping pressure, environment and bonding time.

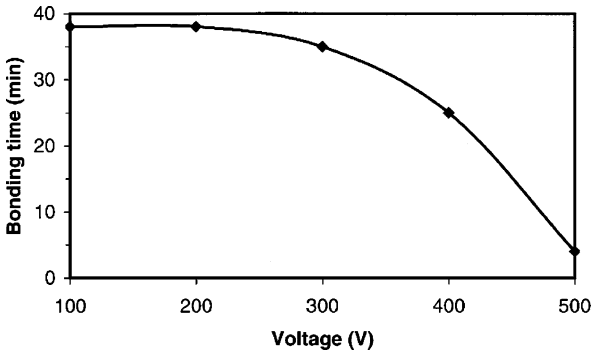

Anodic Bonding, Figure 5 Bonding time as a function of applied voltage for silicon–glass anodic bonding

- Bonding temperature is normally in the range 300 – 500 °C. Higher temperature promotes better mobility of positive ions in glass, resulting in a faster bonding process. However, the temperature must be below the softening point of glass (glass transition temperature).
- Typical bonding voltage is in the range of 200 to 2000 V. High voltage helps to drive the positive ions in glass towards the cathode, leaving a negatively charged region at the bonding interface. The electrostatic force at the interface pulls the silicon and glass in direct contact, resulting in oxygen ions in glass oxidizing the silicon to form strong chemical bonds. Figure 5 shows the bonding time as a function of bonding voltage for anodic bonding of Corning 7740 glass with silicon [6]. It is apparent that higher voltage results in a shorter bonding time. For glasses with low concentration of sodium ions (Na^+), both high temperature and high voltage are necessary for a successful bonding. Higher voltage is also needed for thicker glass. High voltage also helps to reduce the temperature necessary for a good bonding.
- Standard silicon wafers are not completely flat but with $\pm 20 - 40\,\mu m$ bowing and wrapping. In order to make sure the silicon wafer is in intimate contact with the glass, a pressurized clamping is necessary. The clamping pressure is normally below 50 N.
- Anodic bonding can be carried out either in vacuum, or in a gaseous or atmospheric environment. However, bonding in air is much faster than in vacuum or in an inert gas environment [7]. This may be due to the oxygen in air which helps the oxidation process during anodic bonding. However, many applications require anodic bonding to be carried out in vacuum.
- Bonding time is typically 1–5 min for Corning 7740 glass and silicon. For special glasses, the bonding time may be longer. As mentioned before, both bonding temperature and voltage can influence the bonding time. After bonding, there is a cooling time. The cooling can be a few minutes with the help of purging inert gas. However, the cooling should be slow for materials with large difference in CTE.

Inspection and Testing

The bonding process can be visually monitored through the glass. Initially there will be an interference fringe pattern when the silicon and glass are in contact because of the microscopic gaps between them. As the bonding progresses the interference pattern recedes gradually, until a uniform color is seen across the whole bonding surface. Any defects in the bonding will show as voids at the bonding interface. Better inspection of bonding quality can be achieved by scanning acoustic microscopy (SAM). SAM can detect any loose contact at the bonding interface independent of visual errors.

The bonding strength can be tested in different ways, such as pressure testing, pull testing, shear testing and bending testing [2]. The pull test has demonstrated bonding strength in the range 10 – 20 MPa, which is greater than the fracture strength of glass. The upper limit of bonding strength is difficult to estimate, as the break in the pull test always occurs in the glass, not at the silicon–glass interface. However, for imperfect bonding, the bonding strength is poor and the glass often breaks along the boundary of voids.

Although anodic bonding can be done simply with a hot plate and a DC power supply, reliable and reproducible anodic bonding can only be performed with purpose-built systems. There are commercially available wafer bonders. With commercial systems, the bonding process can be either manual or automatic. The bonding is performed in a chamber of either vacuum or filled with gases. One of the key issues in anodic bonding is the alignment when both the silicon and glass have some fabricated microstructures. The alignment process in a commercial wafer bonder can be carried out either off-line or in situ. The in situ alignment is advantageous because high-accuracy alignment ($\pm 5\,\mu m$) occurs only when the process temperature is reached, thus avoiding differential thermal expansion effects which can compromise alignment. It enables the user to make in situ adjustments and visual confirmation before finally committing to making the bond.

Key Research Findings

Anodic bonding is relatively simple in principle and has been well developed over the last few decades. Research in this area has been very much focused on solving practical and application-specific issues. One of the practi-

cal issues is dealing with anodic bonding of silicon–glass assemblies with shallow cavities. This is often encountered in microfluidic systems where microchannels are of high lateral-to-depth aspect ratio. Anodic bonding can cause the microchannels to collapse due to high electrostatic force at the bonding interface. Theoretical and experimental study indicated that the collapse can be avoided as long as the following condition is satisfied [8]:

$$\varepsilon_a V^2 a / E_{\text{eff}} d^3 < 1$$

where ε_a is the permittivity of air, V is the applied voltage for anodic bonding, E_{eff} is a material constant which characterizes the elastic stiffness of the materials, a is the half width of the channel and d is the channel depth. A similar problem happens when packaging pressure sensors, micropumps and accelerometers by anodic bonding. Most of these devices have micromachined silicon membranes, diaphragms or suspended beams. These micromechanical structures may stick to the glass when they are too flexible and too close to the bonding interface.

Although anodic bonding is a low-temperature process compared to fusion bonding which requires temperatures up to 1200 °C, the bonding process can still induce thermal residual stress in the silicon–glass assembly, causing bowing of the bonded wafer. The thermal expansion of Pyrex glass is not a constant but changes with temperature. The higher the bonding temperature the larger the mismatch between silicon and glass. For Corning 7740 Pyrex glass, the crossover point with silicon (where the thermal expansion of silicon is exactly the same as that of Corning 7740 glass) is around 300 °C. Experiments showed that bonding made at this temperature can be maintained flat within ± 5 μm [3]. The crossover point is also dependent on the thickness of glass. Experiments indicated that for 0.5 mm thick glass (Corning 7740) the crossover temperature is at ~ 315 °C, while it becomes ~ 260 °C for 1.5 mm thick glass [7].

It is known that glass cannot be anodically bonded to glass. However, research has found that this can be realized by depositing an intermediate layer. The intermediate layer can be polysilicon, amorphous silicon, silicon nitride or silicon carbide [9]. This has opened an easy route to construct glass-based microfluidic systems which are widely used for capillary electrophoresis. Other investigations into anodic bonding have been on oxygen release into sealed cavities during bonding or proper seals for thin metal films which act as lead through electrodes [3].

Future Directions for Research

Anodic bonding is a fairly mature technique. Many basic issues have been dealt with. Future researches will mostly focus on widening its applications, particularly in microelectronic and microsystem (MEMS) packaging. Packaging can significantly influence the performance of final devices and systems. Therefore, anodic bonding has to be integrated as part of the manufacturing process and its influence should be fully taken into account at the design and manufacturing stages.

Cross References

► Wafer Bonding

References

1. Wallis G, Pomerantz DI (1969) Field assisted glass–metal sealing. J Appl Phys 40(10):3946–3949
2. Obermeier E (1995) Anodic wafer bonding. Electrochem Soc Proc 95-7:212–220
3. Roger T, Kowal J (1995) Selection of glass, anodic bonding conditions and material compatibility for silicon–glass capacitive sensors. Sens Actuators A46–47:113–120
4. Cao E, Gavriilidis A, Cui Z (2002) Application of micro-engineered reactors in chemical engineering. MST News 3/02: 14–16
5. Acero MC, Plaza JA, Esteve J, Carmona M, Marco S, Samitier J (1997) Design of a modular micropump based on anodic bonding. J Micromech Microeng 7:179–182
6. Lee TMH, Lee DHY, Liaw CYN, Lao AIK, Hsing IM (2000) Detailed characterisation of anodic bonding process between glass and thin-film coated silicon substrates. Sens Actuators 86:103–107
7. Cozma A, Puers B (1995) Characterization of the electrostatic bonding of silicon and Pyrex glass. J Micromech Microeng 5:98–102
8. Shih WP, Hui CY, Tien NC (2004) Collapse of microchannels during anodic bonding: theory and experiments. J Appl Phys 95(5):2800–2808
9. Berthold A, Nicola L, Sarro PM, Vellekoop MJ (2000) Glass-to-glass anodic bonding with standard IC technology thin films as intermediate layers. Sens Actuators A82(1-3):224–228

Anthrax

Definition

Anthrax is an acute infectious disease caused by the spore-forming bacterium *Bacillus anthracis*. Anthrax most commonly occurs in wild and domestic lower vertebrates (cattle, sheep, goats, camels, antelopes, and other herbivores), but it can also occur in humans when they are exposed to infected animals or tissue from infected animals.

Antibody

Definition

Antibodies are immune system-related proteins called immunoglobulins. An important component of the immune system, antibodies are found in the blood of all vertebrates. The synthesis, or manufacture, of antibodies is initiated when a foreign substance, referred to as an antigen, enters the body. Lymphocyte cells respond to the foreign substance by making an antibody with a molecular arrangement that fits the shape of molecules on the surface of the substance so that the antibody combines with it. Common antigens are the protein components of bacteria and viruses.

Antigen

Definition

An antigen is any substance that causes the immune system to produce antibodies against it. An antigen may be a foreign substance from the environment such as chemicals, bacteria, viruses, or pollen. An antigen may also be formed within the body, as with bacterial toxins or tissue cells.

Aperiodic AC Field

► Unbalanced AC field

Aperiodic Electrophoresis

Synonyms

Nonlinear electrophoresis; Field-dependent electrophoretic mobility

Definition

Aperiodic electrophoresis refers to the use of an unbalanced AC field to separate charged polarizable particles due to the Stotz–Wien effect of field-dependent electrophoretic mobility.

Cross References

► Electrokinetic Motion of Polarizable Particles
► Electroosmotic Flow (DC)
► AC Electro-Osmotic Flow
► Electrophoresis
► Induced-Charge Electrophoresis
► Nonlinear Electrokinetic Phenomena
► Unbalanced AC field
► Stotz–Wien Effect

Apoptosis

► Microfluidics for Studies of Apoptosis

Apparent Slip

► Boundary Slip of Liquids

ARDE

► Aspect Ratio Dependent Etching

Arnoldi Algorithm

► Arnoldi-Based Model Order Reduction

Arnoldi-Based Macromodeling

► Arnoldi-Based Model Order Reduction

Arnoldi-Based Model Order Reduction

Synonyms

Arnoldi-based macromodeling; Arnoldi algorithm

Definition

Arnoldi-based algorithm is a classical Krylov-subspace-based Model Order Reduction technique. It reduces the dimension of the spatially semi-discretized form of the original governing PDEs using moment-matching of transfer functions.

Cross References

► Model Order Reduction (MOR)
► Macromodels
► Macromodel

Artificial Atom

► Quantum Dot

Artificial Muscle Materials

► Piezoelectric Materials for Microfluidics

Artificial Neural Networks

Synonyms

ANN

Definition

An artificial neural network is an information processing paradigm inspired by way the human nervous system processes information. It consists of an interconnected group of processing elements (neurons) which can exhibit a complex global behavior, determined by the network topology (the scheme used to connect elements together), and the algorithm (the rules) employed to specify the values of the weights connecting the nodes, the connections between the neurons. Based on *training rules* (whereby the weights of connections are adjusted on the basis of presented patterns), ANNs can be trained to generate an arbitrary number of outputs in response to an arbitrary number of inputs.

Cross References

► Model Order Reduction (MOR)
► Neural Network

Aspect Ratio Dependent Etching

Synonyms

ARDE

Definition

ARDE is the phenomenon of the etching rate related to the aspect ratio. The larger the aspect ratio, the lower the etching rate.

Cross References

► RIE Lag
► Anisotropic Etching
► Reactive Ion Etching (RIE)
► Plasma Etching

Assay

Synonyms

Test

Definition

A method for the determination of the level of a given analyte in a given sample or set of samples.

Cross References

► Lab-on-a-Chip Device for Chemical Analysis

Assembly of Nanoparticles Into Controlled Nanostructures

► Nano-Particle Controllable Assembly

Atomic Force Microscope (AFM)

Definition

Material characterization technique which uses a tip (typically silicon) on the end of a cantilever to determine the surface profile of a material. As the cantilever is moved across the surface, a laser is reflected off of the backside. As the cantilever is deflected, the change in laser beam position is detected by a photodetector. This information is then used to create a three-dimensional image of the surface, with atomic-scale resolution.

Cross References

► AFM
► Fabrication of Self-Assembled Catalytic Nanostructures

Atomistic Computer Simulation

► Molecular Dynamics Simulation Method

Atomistic Deposition

► Chemical Vapor Deposition for Film Deposition

Atwood Number

Definition

A dimensionless number that describes the density difference between two adjacent fluids with a common interface.

Cross References

► Piezoelectric Microdispenser